Schweizerische Eidgenossenschaft
Confédération suisse
Confederazione Svizzera
Confederaziun svizra

Federal Department of the Environment, Transport, Energy and Communications DETEC

Swiss Federal Office of Energy SFOE
Energy Research and Cleantech Division

Final report dated 31st March, 2021

Feasibility Study for Proposed CO_2 Circulation Test at the Aquistore Injection Site, Saskatchewan

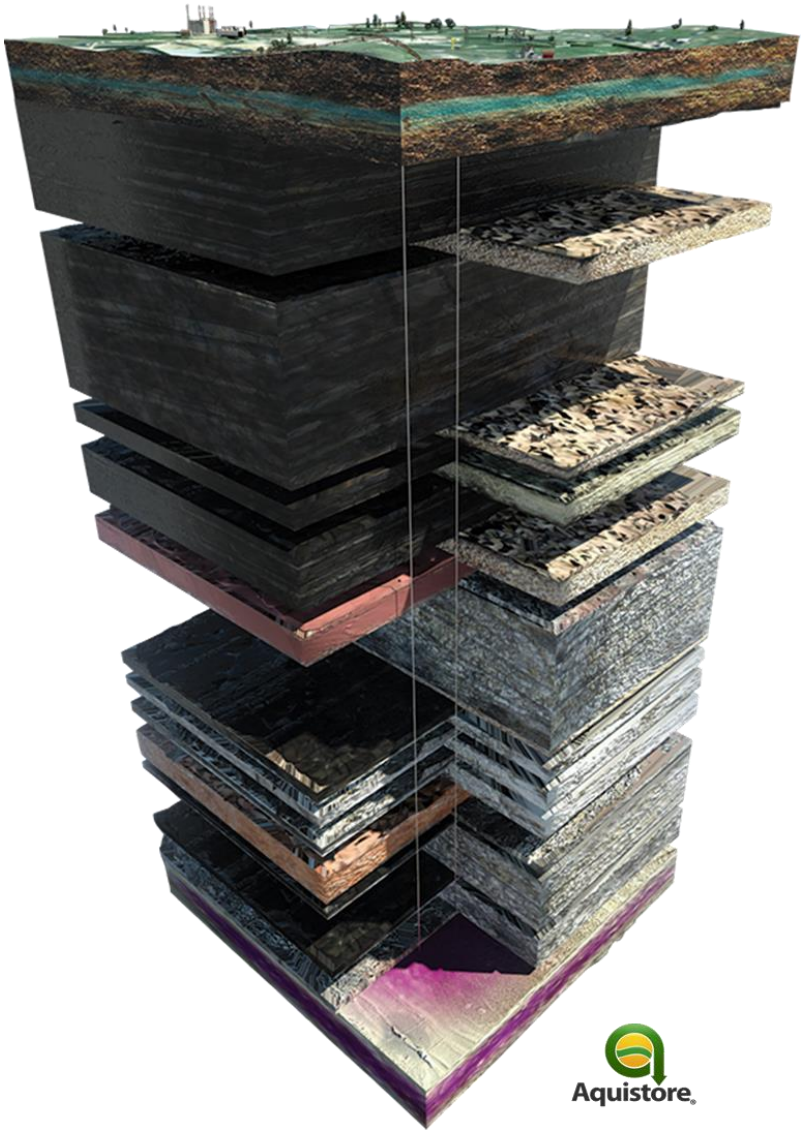

Source: aquistore.ca

Date: 31 March 2021

Location: Bern

Publisher:
Swiss Federal Office of Energy SFOE
Energy Research and Cleantech
CH-3003 Bern
www.bfe.admin.ch

Subsidy recipients:
Petroleum Technology Research Centre (PTRC)
220-6 Research Drive,
Regina, Saskatchewan, S4S 7J7
Canada

Authors:
Alireza Rangriz Shokri, PhD, University of Alberta, rangrizs@ualberta.ca
Rick Chalaturnyk, PhD, PEng, University of Alberta, rjchalaturnyk@ualberta.ca

SFOE project coordinators:
Gunter Siddiqi, gunter.siddiqi@bfe.admin.ch

SFOE contract number: SI/502043-01

Zusammenfassung

In Folge des Interesses für ein mögliches CO2 Plume Geothermal (CPG) Pilotprojekt am CO2-Speicherstandort Aquistore in Saskatchewan, Kanada wurde die University of Alberta beauftragt, die Machbarkeit eines CO2-Zirkulationstests als ersten Schritt zu einem CO2 Plume Geothermal (CPG) Feldexperiment zu untersuchen. Bei der von Schweizer Wissenschaftern entwickelten CPG Technologie, wird CO2 als Arbeitsmedium für ein geothermisches Energiesystemen eingesetzt, wobei das CO2 auch in tiefen, salinen Aquiferen gespeichert wird. CPG als mögliche Technologie zur Energiebereitstellung und als Ergänzung zur Kohlenstoffabscheidung und -speicherung (CCS) hat das Potenzial, die Kosten für CCS-Operationen zu senken und könnte in geothermisch günstigen Regionen sogar zusätzliche Umsätze generieren. Noch wichtiger ist, dass das gesamte CO2 während des Betriebs einer CPG Anlage in den jeweiligen unterirdischen Gesteinsformationen gespeichert wird.

Die vorliegende Machbarkeitsstudie befasst sich mit einigen Herausforderungen, wenn geologisch gespeichertes CO2 unter Verwendung eines Bohrloch-Doubletten-Systems an die Oberfläche zurückgeführt wird. Diese Studie unterstützt das Forschungsinstitut PTRC/SaskPower bei der Identifizierung der Vor- und Nachteile eines CO2-Zirkulationstests (ein Schlüsselelement von CPG), um die Möglichkeiten und Grenzen der CPG-Technologie aufzuzeigen und eine Bewertung der wichtigsten Lagerstättenvariablen liefern, die die Leistung eines CO2-Zirkulationstests am Aquistore-Injektionsstandort potenziell beeinflussen.

Für diese Machbarkeitsstudie wurde Literatur über geothermische Systeme und Thermosiphons konsultiert, um die Mindestanforderungen vor der Durchführung von CO2-Zirkulationstests zu bestimmen, wobei der Schwerpunkt auf den Lagerstättenbedingungen am Aquistore-Injektionsstandort lag. Ein Sektormodell wurde aus dem vollständig verfügbaren geologischen Modell des Aquistoreprojekts extrahiert und für weitere Simulationen des CO2-Zirkulationstests in ein sehr feines geozelluläres Modell erweitert.

Statische Unsicherheits-Workflows wurden entwickelt, um die wahrscheinlichsten Realisierungen der CO2-Fahnenausdehnung und -form mit Hilfe numerischer Simulationen und den neuesten verfügbaren seismischen Untersuchungen zu modellieren. Zahlreiche Realisierungen (Stratigraphie, stochastische petrophysikalische Eigenschaften, Berücksichtigung der Flexur geologischer Gesteinsschichten, und Ausdehnung der CO2-Fahne bestimmt mittels neuer seismischer Daten) durchgeführt, um sowohl die CO2-Fahne als auch die Injektionsgeschichte abzugleichen.

Die dynamische Unsicherheitsanalyse des CO2-Zirkulationstests trug dazu bei, einige der Herausforderungen zu identifizieren, nämlich in Bezug auf die Auswirkungen der Ausdehnung und Form der CO2-Fahne, der anfänglichen Wasser- und CO2-Sättigungen innerhalb der CO2-Fahne, der Heterogenität der petrophysikalischen Eigenschaften und der Betriebsvariablen sowie der Injektions- als auch der Produktionsbohrungen zu klären, neben anderen. Die Simulationen deuten darauf hin, dass die CO2-Zirkulation bei Aquistore machbar ist; sie führt nicht zu grossen Volumina an saliner Wasserproduktion aus dem Aquifer, erfordert aber vor der Durchführung des Pilotversuchs erhebliche Arbeit am Front-End-Engineering-Design.

In allen Realisierungen gab es einen anfänglichen Anstieg in der Produktion von salinem Wasser bevor sich eine kontinuierliche CO2-Produktion mit einem stabilen Wasser/Gas-Verhältnis einstellt; die anfängliche Produktion von salinem Wasser sollte nicht als Versagen des Tests angesehen werden. Stattdessen sollte eine geeignete Oberflächeneinrichtung entworfen werden, um diese anfängliche Produktion zu handhaben.

Eine Massenbilanz der CO2-Masseninjektion und -produktion während des CO2-Zirkulationstests zeigt, dass ein Teil des injizierten CO2 dauerhaft im Aquifer gespeichert wird. Diese CO2-Speicherung dient dem eigentlichen Ziel von Aquistore, nämlich der dauerhaften CO2-Speicherung. Allerdings sollte bei jedem CO2-Zirkulationstest dem Injektionskreislauf CO2 nachgefüllt werden.

Ebenso wichtig ist, dass die Betriebsbedingungen sowohl des Injektors als auch des Produzenten für einen erfolgreichen CO2-Zirkulationstest optimiert werden können; dazu gehören unter anderem die Stimulation des Bohrlochs, die Optimierung der Injektions-/Förderraten, die Druckbeschränkungen und das Design der Komplettierung sowohl des Injektors als auch des Produzenten.

Wir prognostizieren auch die potenziellen komplexen Strömungsregime und ihre Auswirkungen auf den Produzenten (Koproduktion von CO2 und salzhaltigem Wasser) mit Hilfe von vereinfachten vertikalen Zweiphasen-Strömungsmodellen und adressieren auch die Bildung von CO2-Clathraten während des CO2-Zirkulationsbetriebs, was zu einer Verstopfung der Steigrohre, reduzierten Durchflussraten oder Salzausfällungen führen könnte.

Zukünftige Arbeiten und Wissenslücken umfassen die Auswirkungen potenzieller thermisch induzierter Frakturation des Reservoirs und deren Ausbreitung (Kurzschluss der Bohrlöcher), die Geochemie von überkritischem CO2 (Sole/CO2/Gestein), mögliche langfristige Änderungen der Reservoirporosität und -permeabilität, das Wärmeentzugsverhalten während der CO2-Zirkulation, CO2-Verluste und den Bedarf an Make-up-Flüssigkeit.

Das in dieser Studie entwickelte Modell kann verwendet werden, um in zukünftigen Studien den Standort eines neuen Produzenten oder einer zusätzlichen Injektionsbohrung für die Entsorgung des ko-produzierten Formationswasser, die Schaffung zusätzlicher Porosität und das Reservoirdruckmanagement zu bestimmen.

Résumé

En réponse à l'intérêt manifesté pour le site de stockage Aquistore, pour un essai pilote, l'Université de l'Alberta a été chargée d'étudier la faisabilité d'un test de circulation de CO_2, représentant une première étape vers la réalisation d'une expérience in situ de CO_2 Plume Geothermal (CPG). La technologie CPG, développée par des scientifiques suisses, utilise le CO_2 comme fluide de travail dans des systèmes géothermiques , tout en permettant de le séquestrer dans les aquifères salins profonds. Le concept du CPG représente une technologie émergente dans le domaine de la production d'électricité et un complément au captage et au stockage du carbone (Carbon Capture and Sotrage, CCS). Il peut ainsi potentiellement réduire le coût des opérations de CCS, voire même permettre de générer un revenu dans les régions propices à la géothermie. Enfin, et surtout, tout le CO_2 sera in fine stocké dans les formations souterraines ciblées pendant le CPG.

Cette étude de faisabilité aborde certains des problèmes qui se posent lorsque le CO_2 séquestré géologiquement est remis en circulation vers la surface à l'aide d'un système de doublet de puits. Elle a pour but d'aider PTRC / SaskPower à identifier les risques liés à l'exécution d'un test de circulation du CO_2 (un élément clé du CPG), d'apporter des éléments à l'OFEN quant aux possibilités et aux limites de la technologie CPG, et de fournir une évaluation des caractéristiques principales du réservoir qui sont susceptibles d'affecter les performances d'un test de circulation de CO_2 sur le site d'injection d'Aquistore.

Pour réaliser cette étude de faisabilité, nous avons fait l'état de l'art des systèmes géothermiques stimulés ainsi que de la littérature relative aux thermosiphons en focalisant l'attention sur des conditions de réservoir telles qu'on les trouve dans le site d'injection d'Aquistore. Ceci a permis de déterminer les exigences minimales qu'il convient de respecter lorsqu'on souhaite effectuer des tests de circulation de CO_2. Un modèle de secteur de référence a été extrait du modèle géologique complet disponible pour Aquistore. Il a été reconstitué avec une maille géocellulaire très fine afin d'effectuer des simulations supplémentaires du test de circulation de CO_2.

Nous avons développé des processus (workflows) statiques de traitement des incertitudes et avons évalué l'étendue et la forme les plus probables du panache de CO_2, en nous aidant, d'une part, des

simulations numériques calibrées pour recréer les évènements du passé, et d'autre part, les dernières études sismiques disponibles. Plusieurs représentations du modèle ont été réalisées (modèles à plusieurs couches, propriétés pétrophysiques stochastiques, inclusion de la flexion, restriction du panache de CO_2 aux relevés sismiques), afin de corroborer les données historiques relatives au panache et à l'injection de CO_2.

L'analyse dynamique des incertitudes liées au test de circulation du CO_2 a permis de traiter certains des problèmes notamment liés à l'impact de l'étendue et de la forme du panache de CO_2, des saturations initiales en eau et en CO_2 dans le panache, de l'hétérogénéité des propriétés pétrophysiques, et des variables opérationnelles aussi bien du puit d'injection que du puits de production. Les simulations suggèrent que la circulation du CO_2 semble faisable à Aquistore ; cela n'entraîne pas la production d'énormes volumes de saumure de l'aquifère, mais nécessite en revanche un travail important sur la conception technique avant d'exécuter le test pilote.

Dans toutes les représentations du modèle, il y avait d'abord un pic initial de production de saumure avant la production continue de CO_2 avec un rapport eau / gaz stable ; cette production initiale de saumure ne doit pas être considérée comme un échec du test. Au contraire, une installation appropriée devrait être conçue en surface pour gérer cette production initiale de saumure.

Un bilan massique du CO_2 entre l'injection et la production lors du test de circulation indique qu'une partie du CO_2 injecté reste stockée de façon permanente dans l'aquifère salin. Cette perte de CO_2 sert l'objectif ultime d'Aquistore, à savoir le stockage permanent du CO_2. Cependant, un liquide de compensation doit être ajouté au CO_2 durant l'injection pour tout test de circulation de CO_2.

Il est tout aussi important d'optimiser les conditions opératoires des puits d'injection et de production pour réaliser un test de circulation du CO_2 qui soit réussi. Ces conditions incluent, entre autres, la stimulation de puits, les débits d'injection et production, les contraintes de pression et les caractéristiques de l'achèvement des puits d'injection et de production.

Nous avons également évalué les régimes d'écoulement potentiellement complexes et leurs impacts sur le puits de production (co-production de CO_2 et de saumure) à l'aide de modèles d'écoulement vertical bi-phasiques simplifés. Cela nous a permis d'étudier la formation de l'hydrate de CO_2 pendant la circulation du CO_2. Ce clathrate pourrait entraîner des obstructions dans les conduites/tuyaux, une réduction des débits, ou encore la précipitation de sels.

Les futurs travaux et les lacunes qu'il convient encore de combler porteraient sur l'impact de potentielles fractures induites thermiquement ainsi que leur propagation (court-circuitage des puits), la géochimie du CO_2 supercritique (saumure / CO_2 / roche), les potentielles altérations à long terme de la porosité et de la perméabilité du réservoir, la dynamique d'extraction de la chaleur pendant la circulation du CO_2, les pertes de CO_2 et le recours à un liquide de compensation.

Le modèle développé dans cette étude peut être utilisé dans de futures études pour définir l'emplacement d'un nouveau puits de production ou d'un puits supplémentaire pour l'élimination de la saumure, les mécanismes de compensation des fluides et la gestion de la pression du réservoir.

Summary

Responding to an interest shown in the Aquistore storage site for a pilot test, the University of Alberta was tasked to study the feasibility of a CO_2 circulation test as a first step towards a CO_2 Plume Geothermal (CPG) field experiment. The CPG uses CO_2 as the working fluid in geothermal power systems while sequestering CO_2 in deep saline aquifers. The concept of CPG, as an emerging power generation technology and an add-on to carbon capture and storage (CCS), has the potential to reduce the cost of CCS operations, and might even generate revenue in geothermally favorable regions. More importantly, all the CO_2 will eventually be stored during CPG into the targeted subsurface formations.

This feasibility study addresses some of the issues when geologically sequestered CO_2 is recirculated to the surface using a well doublet system. This study aims to assist PTRC/SaskPower in identifying the upside/downside risks of running a CO_2 circulation test (a key element of CPG), to assist the SFOE with the possibilities and limitations of the CPG technology, and to provide an assessment of key reservoir variables that potentially affect the performance of a CO_2 circulation test at the Aquistore injection site.

For this feasibility study, we reviewed enhanced geothermal systems and thermosiphon literature to determine minimum requirements prior to conducting CO_2 circulation tests, with a focus on reservoir conditions at the Aquistore injection site. A base sector model was extracted from the available full geological model of Aquistore, and it was re-built into a very fine-scale geocellular model for further simulations of the CO_2 circulation test.

We developed static uncertainty workflows and appraised the most probable realizations of CO_2 plume extent and shape from the history-matched numerical simulations and the latest available seismic surveys. Many realizations (layer cake model, stochastic petrophysical properties, inclusion of flexure, and constraining the CO_2 plume to the seismic surveys) were conducted to match both CO_2 plume and injection history.

The dynamic uncertainty analysis of the CO_2 circulation test helped to address some of the issues related to the impacts of the extent and shape of CO_2 plume, initial water and CO_2 saturations within the CO_2 plume, heterogeneity in petrophysical properties, and operational variables of both injection and production wells, among others. Simulations suggest that CO_2 circulation seems feasible at Aquistore; it does not result in huge volumes of brine production from the aquifer, but it needs significant work on front end engineering design prior to executing the pilot test.

In all realizations, there was an initial brine kick prior to continuous CO_2 production with a stable water/gas ratio; the initial brine production should not be thought of as a failure of the test. Instead, proper surface facility should be designed to handle this initial brine production.

A mass balance of CO_2 mass injection and production during the CO_2 circulation test indicates that a portion of injected CO_2 will permanently be stored in the saline aquifer. This CO_2 loss serves the ultimate goal of Aquistore, i.e. permanent CO_2 storage. However, CO_2 make-up fluid should be added to the injection cycle during any CO_2 circulation test.

Equally important, the operating conditions of both the injector and the producer can be optimized for a successful CO_2 circulation test; these include, but are not limited to, well stimulation, injection/production rates, pressure constraints, and completion designs at both injector and producer, among others.

We also estimated the potential complex flow regimes and their impacts on the producer (co-production of CO_2 and brine) using simplified two-phase vertical flow models, and commented on the formation of CO_2 clathrate during CO_2 circulation operation that could result in tubing/pipes blockage, reduced flow rates, or salt precipitation.

Future work and knowledge gaps include the impact of potential thermally induced fractures and their propagation (short circuiting the wells), geochemistry of supercritical CO_2 (brine/CO_2/rock), possible long-term changes in reservoir porosity and permeability, heat extraction behavior during CO_2 circulation, CO_2 loss, and the need for make-up fluid.

The developed model in this study can be used to determine the location of a new producer or an additional brine well for brine disposal, voidage replacement, and reservoir pressure management in future studies.

Main findings

- Instead of treating CO_2 as a waste product to be disposed of, emerging technologies such as CO_2 Plume Geothermal (CPG) offer the possibility to utilize the disposed CO_2 as a geothermal (i.e. subsurface) working fluid to produce sustainable geothermal energy.

- The Aquistore CCS site, the largest experimental laboratory in the world for the measurement and monitoring of industrial-scale levels of injected CO_2, provides a unique opportunity towards CPG commercialization and to improve its technology readiness level through a pilot field experiment; Aquistore satisfies the minimum requirements of a CPG system and the CO_2 circulation test.

- Simulations suggest that CO_2 circulation, a key element of a CPG system, seems feasible at Aquistore; it does not result in huge volumes of brine production from the aquifer, but it needs significant work on Front End Engineering Design prior to executing the pilot test.

- During the CO_2 circulation test, a portion of injected CO_2 will permanently be stored in the saline aquifer. This CO_2 loss serves the ultimate goal of Aquistore, i.e. permanent CO_2 storage. It is belived that at the end of its life cycle, CPG permanently sequesters 100% of the injected CO_2 in the geological reservoir.

Contents

Abbreviations

List of used abbreviations (if applicable)

CCS Carbon Capture and Storage

CCUS Carbon Capture Utilization and Storage

CH_4 methane

CMG Computer Modelling Group Ltd.

CO_2 Carbon Dioxide

CPG CO_2 Plume Geothermal

DEEP Deep Earth Energy Production (a Saskatchewan privately held corporation to develop geothermal resources for power generation)

DTS Distributed Temperature Sensing

EGS Engineered/Enhanced Geothermal System

EOR Enhanced Oil Recovery

FRS Fluid Recovery System

GEM Generalized Equation of state Modeling software

HDR Hot Dry Rock

InSAR Interferometric Synthetic Aperture Radar

MD Measured Depth

mD millidarcy (permeability unit)

NAD83 North American Datum of 1983

NNW North-Northwest

PERF Perforated Interval

PND Porosity Neutron Density log

ppm parts per million

PR EOS Peng-Robinson Equation of State

PTRC Petroleum Technology Research Centre

RG^2 Reservoir Geomechanics Research Group

RMS Root Mean Square

S Wellbore skin factor

SECARB South Eastern Regional Partnership for Carbon Sequestration

SFOE Swiss Federal Office of Energy

SSE South-Southeast

TDS Total Dissolved Solids

TRL Technology Readiness Level

1 Project Introduction and Objectives

1.1 Background information and current situation

1.1.1 Review of Relevant Experience with Enhanced Geothermal Systems

Exploitation of geothermal energy, often considered a clean renewable source used for electricity generation, involves the circulation of water into deep (>2.5 km) hot (>250 ºC) subsurface formations, known as Hot Dry Rock (HDR) (Coats 1977; Brown 2000). Because most geothermal resources do not offer adequate permeability for efficient fluid circulation, geothermal systems are engineered through hydraulic fracturing and stimulation to create permeable pathways for geothermal fluid from the injectors to the producers, referred to as the Engineered/Enhanced Geothermal Systems (EGS). Water, a common geothermal fluid, is often used to mine the heat from deep subsurface formations due to its many distinct properties, including for instance its phase behaviour and high heat capacity. In addition, water has long been taken for granted for use in many industries, but today (relatively fresh) water is a valuable commodity in many countries and its loss in conventional EGS could have significant environmental and economic consequences (Preuss 2006). Given the high pressure, high temperature conditions in EGS reservoirs, water could also act as a solvent for rock minerals with unfavourable impacts on heat extraction and fluid circulation (e.g. dissolution, precipitation, permeability reduction, Xu and Pruess 2004). To answer the need of geologic storage of CO_2, to advance the conventional EGS reservoirs, and as an alternative to some unfavourable drawbacks for the use of water (e.g. water loss, reactive fluid/rock transport, precipitation), CO_2 has been proposed as a transmission fluid in HDR systems for reservoir creation and heat extraction (Brown 2000).

Following up with the idea of CO_2 as a geothermal working fluid, many researchers have explored the topic of mass and heat transport in CO_2-based EGS reservoirs (e.g. Brown 2000; Fouillac et al. 2004; Pruess 2006, 2008; Pruess and Azaroual, 2006; Atrens et al. 2009; Nielsen et al. 2013; Zhang et al. 2016; Sepulveda et al. 2018). Since typical EGS reservoirs operate at high temperature and high pressure conditions, CO_2 is expected to be at a supercritical state. Based on these studies, some features of using supercritical CO_2 in a closed loop, as compared to water, are summarized as follows:

- Supercritical CO_2 has gas-like viscosity, which allows the larger flow rates at lower pressure gradient.
- Supercritical CO_2, with liquid-like density, offers a larger ratio of density to viscosity (i.e. favorable mobility).
- Supercritical CO_2 has lower mass heat capacity, an unfavorable condition, but is compensated for by lower CO_2 viscosity and greater flow capacity.
- When using supercritical CO_2, less geochemical interactions with solids and fewer scaling problems (e.g. silica dissolution, precipitation) are expected compared to water (Xu et al. 2005; Ueda et al. 2005; Preuss 2008).
- Supercritical CO_2 has larger expansivity/compressibility than water. This results in a larger density difference, hence, stronger buoyancy forces between injector and producer, reducing the power consumption for fluid circulation. In theory, the fluid circulation might even continue without external pumping (i.e. thermosiphon effect).
- Supercritical CO_2 can be efficient in energy extraction from shallower subsurface formations with lower temperature/pressures, as compared to deep hot dry rock in conventional EGS. This potentially extends the application of geothermal energy to many other formations that were previously assumed unfit for conventional EGS.

- With respect to Aquistore (CO_2 storage in saline formations), the inevitable fluid loss during any EGS operation could be a benefit as CO_2 loss/trapping within the subsurface formations serves the ultimate goal of the geologic storage of CO_2.

- The combination of power generated and CO_2 stored could provide economic benefits to compensate for pumping CO_2 into the formation, in addition to generating revenue (e.g. tax credits for CO_2 storage).

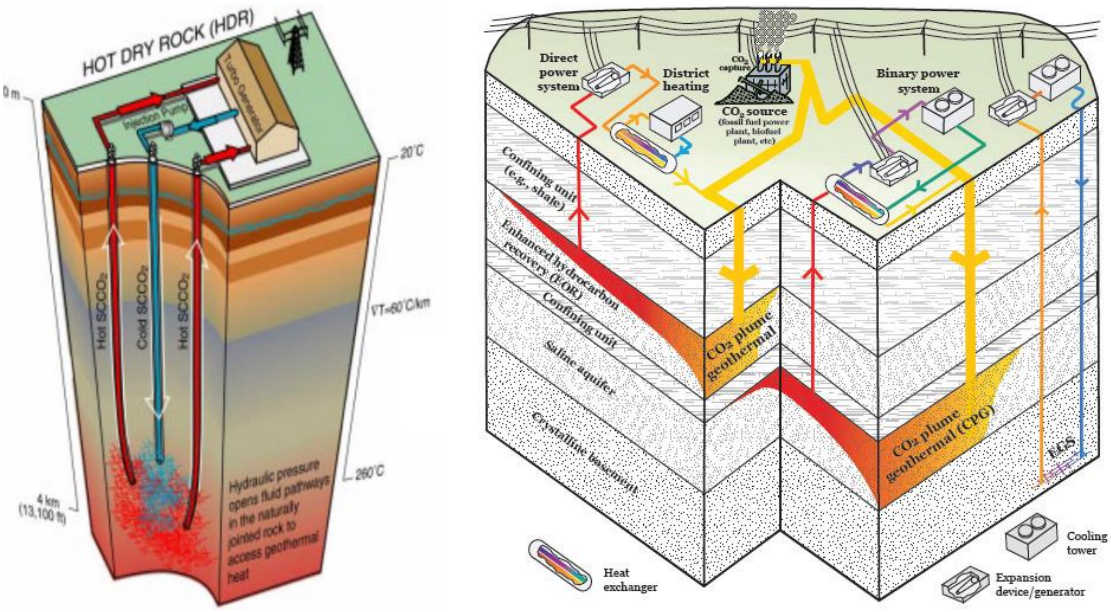

(a) (b)

Figure 1: Schematic of (a) CO_2 geothermal from hot dry rock system (after Brown 2000), and (b) CO_2 plume geothermal system (after Randolph et al. 2013)

Since most underground formations are initially filled with water or hydrocarbons, a very crucial step to deploy a CO_2-based EGS reservoir is to remove the water/hydrocarbons and replace them with CO_2 (e.g. **Figure 1**). To produce a fairly dry CO_2 reservoir, continuous CO_2 circulation is needed to remove or displace the water/hydrocarbons from the injector and producer. Several researchers have addressed this question and characteristics of such successful and practical CO_2-based EGS reservoirs (Brown 2000; Pruess 2006, 2008; Atrens et al. 2009; Randolph and Saar 2011; Adams et al. 2014, 2015; Garapati et al. 2015; Hau et al. 2021). Of interest to this work, CO_2 Plume Geothermal offers synergetic utilization of the subsurface formation for both geologic CO_2 storage and geothermal power generation. A CPG system involves the CO_2 injection into the subsurface formation as in any typical geologic CO_2 storage project (both in saline aquifers and enhanced oil/gas recovery of hydrocarbon resources). The CO_2 displaces the brine and contribute to the formation of a CO_2 plume. Once the plume has sufficient saturation and thickness, the CO_2 can be circulated between injector(s) and producer(s) within the plume. During CO_2 circulation, the injected CO_2 is heated as it moves in the subsurface formations. The extracted heat is then delivered by CO_2 to the surface and used to generate electric power or provide direct heat utilization (Randolph and Saar 2011a,b; Adams et al. 2014, 2015; Garapati et al. 2015).

Since its inception, the applications, benefits and challenges of CPG have been discussed in the literature (e.g. Randolph and Saar 2011a, 2011b; Randolph et al. 2012; Adams et al. 2014, 2015; Garapati et al. 2015; Fleming et al. 2018, 2020; Levy et al. 2018; Ezekiel et al. 2020, Hau et al. 2021). This includes a great body of work focused on developing reservoir models, power cycle models, and cost models. A CPG system is believed to have the most benefits of a conventional geothermal system, but it can potentially generate 2-5 times more electricity than water-based geothermal. In CPG, there are few-to-no issues with hydrofracking, induced seismicity, and fresh water consumption (e.g. Adams et al. 2015, Saar 2019). A CPG facility is claimed to provide cost-competitive electricity from sufficiently

deep (>2 km), hot (> 100 °C) and transmissible (> 5000 mD-m) reservoirs (Saar 2019; Adams et al. 2015). Available literature suggests that CPG seems a viable geothermal energy solution for both power generation and geologic CO_2 storage in deep and shallow suitable reservoirs, with significantly higher heat mining rates than both CO_2-based EGS and traditional water-based EGS reservoirs.

To date, no field trial has been conducted to measure the efficacy of a CPG system. A closely relevant pilot test on the potential of thermosiphon during CO_2 circulation between two wells was reported in the literature. The pilot test, known as the Cranfield CO_2 Thermosiphon Test, was conducted at the Cranfield site in a saline aquifer (Hovorka et al. 2013; Delshad et al. 2013). The field experiment was operated by the South Eastern Regional Partnership for Carbon Sequestration (SECARB). The well site consisted of one injector and two collinear observation wells about 70 m and 100 m away from injector. The saline formation was 3.2 km deep, with 32.5 MPa pressure and 129 °C temperature. The 23 m thick perforated interval was described as highly heterogeneous with permeabilities in the range of 100-300 mD. The initial modeling work predicted a sustaining thermosiphon could be established without any external pump. The water production was predicted to be insignificant. The Cranfield pilot test, however, showed that the thermosiphon decays faster than expected until it is no longer self-sustaining; it also indicated significant water production from the producer. Although the Cranfield test did not establish and sustain a thermosiphon in its partially saturated formation, it provided invaluable lessons learned in the design of subsequent pilot tests for CO_2 circulation. Some of the observations and lessons learned from the Cranfield pilot test include (Pan et al. 2015; Freifeld et al. 2016; Pan et al. 2018):

- the importance of understanding water mobility and irreducible water at in-situ conditions;
- challenges with reservoir heterogeneity and its impact on multi-phase flow performance (e.g. high-permeability sands might be CO_2-saturated while low-permeability shales might remain water-saturated, different relative permeability and capillary pressure);
- issues with characterization of possible fast pathways (e.g. sand/shale sequences, induced fractures) between injection and production wells, and short-circuiting the flow/heat fronts within the reservoir;
- challenges with complex outflow performance in the production well, and potential need for workover (e.g. changes in multi-phase flow regimes, liquid loading, salt precipitation, CO_2 clathrate formation).

Of relevance to this report and significance to the application of the CPG system, Hau (2020) and Hau et al. (2021) looked into the multi-phase flow behaviour and fractional flow of CO_2/brine within a well doublet at the Aquistore site. Given lack of field data, Hau et al. noted that a field experiment is essential to improve the technology readiness level (TRL) of CPG systems. Rather than demonstrating that geothermal energy could be utilised to generate power, Saar (2019) and Hau et al. (2021) emphasized the fact that such field tests should primarily show that a stable CO_2 circulation (not brine) between the injector and producer within the CO_2 plume could be achieved and maintained; what we collectively refer to as a CO_2 circulation test. Hau et al. (2021) used a simplified numerical model for the 2nd perforated interval of the Aquistore injection and observation wells and concluded that CO_2 gas predominantly enters the producer (observation well) with 85-90% CO_2 saturation independent of assumed absolute and relative permeabilities. This report builds on the previous work and addresses some of the issues with a CO_2 circulation test at Aquistore, such as the use of a history-matched model, uncertainties associated with reservoir characterisation, formation heterogeneity, design of injection/production well completions, and operational parameters, among others.

1.2 Purpose of the project

As the most comprehensive full-scale geological field laboratory in the world, Aquistore continues to show that geological storage of CO_2 in deep saline aquifers can be a safe, practical way to meet the

commitments of climate change and net-zero carbon emission policies. Treating CO_2 as a valuable commodity rather than waste to dispose of, emerging technologies such as CO_2 Plume Geothermal (CPG) offer new possibilities to utilize CO_2 as a geothermal working fluid in order to generate geothermal power, while permanently sequestering CO_2 in underground formations. As a step towards its commercialization and to improve the technology readiness level of CO_2 Plume Geothermal, a pilot field experiment is required (Hau et al. 2021). Such field tests should primarily show that a stable CO_2 circulation (not brine) between the injector and producer within the CO_2 plume could be achieved and maintained, rather than demonstrating that geothermal energy could be utilised to generate power (Saar 2019; Hau et al. 2021); what we collectively refer to as a CO_2 circulation test.

1.3 Objectives

Prior to performing any field experiment, The Petroleum Technology Research Centre (PTRC) and the Swiss Federal Office of Energy (SFOE) tasked the Reservoir Geomechanics Research Group (RG^2) of the University of Alberta with a “Feasibility Study for a Proposed CO_2 Circulation Test at the Aquistore Injection Site, Saskatchewan”. The simulation work was aimed to address the following objectives:

- providing primary outcomes to assist PTRC/SaskPower in identifying the upside/downside risks of running a CO_2 circulation test at Aquistore,
- helping the SFOE to demonstrate the possibilities and limitations of the CPG technology, using the pilot test site of Aquistore, and
- providing an assessment of key reservoir variables that potentially affect the performance of a CO_2 circulation test at Aquistore injection site.

CPG seems an attractive solution to carbon capture utilization and storage (CCUS) technologies, because of both power generation and geologic CO_2 storage. We believe the preliminary findings of this report answer some key questions related to CPG development and operation, and ultimately its pilot test at a geologic CO_2 storage site such as Aquistore.

2 Description of facility

2.1 Overview of Aquistore CO_2 Storage Site and Injection History

Aquistore is the geological storage component of the Boundary Dam Integrated Carbon Capture and Storage (CCS) demonstration project, owned by SaskPower and operated by Petroleum Technology Research Centre in Saskatchewan, Canada (**Figure 2**). The required CO_2 is captured from the flue gas of a coal-fired power generation station. If CO_2 is not required for Enhanced Oil Recovery (EOR) projects, it is transported through an underground pipeline to the Aquistore injection well (~3.4 km deep). A cumulative injected mass of over 350 ktonnes of CO_2 had been achieved by February 2021 with varying injection rates of up to ~600 tonnes/day of CO_2. To maximize injectivity, the injection targeted four perforated zones between 5.5 and 27.5 metres thick (totaling 88 metres) of the best reservoir layers, over a total interval of 200 m, targeting the Deadwood Formation, and the Black Island sandstone member of the Winnipeg Formation. The primary seal of the storage geological complex is the shaly Icebox member of the Winnipeg Formation (~30 m thickness) with the Prairie Evaporite acting as an additional safety barrier to CO_2 upward flow (Movahedzadeh et al. 2021; Rangriz-Shokri et al. 2021; Rostron et al. 2014; White et al. 2016).

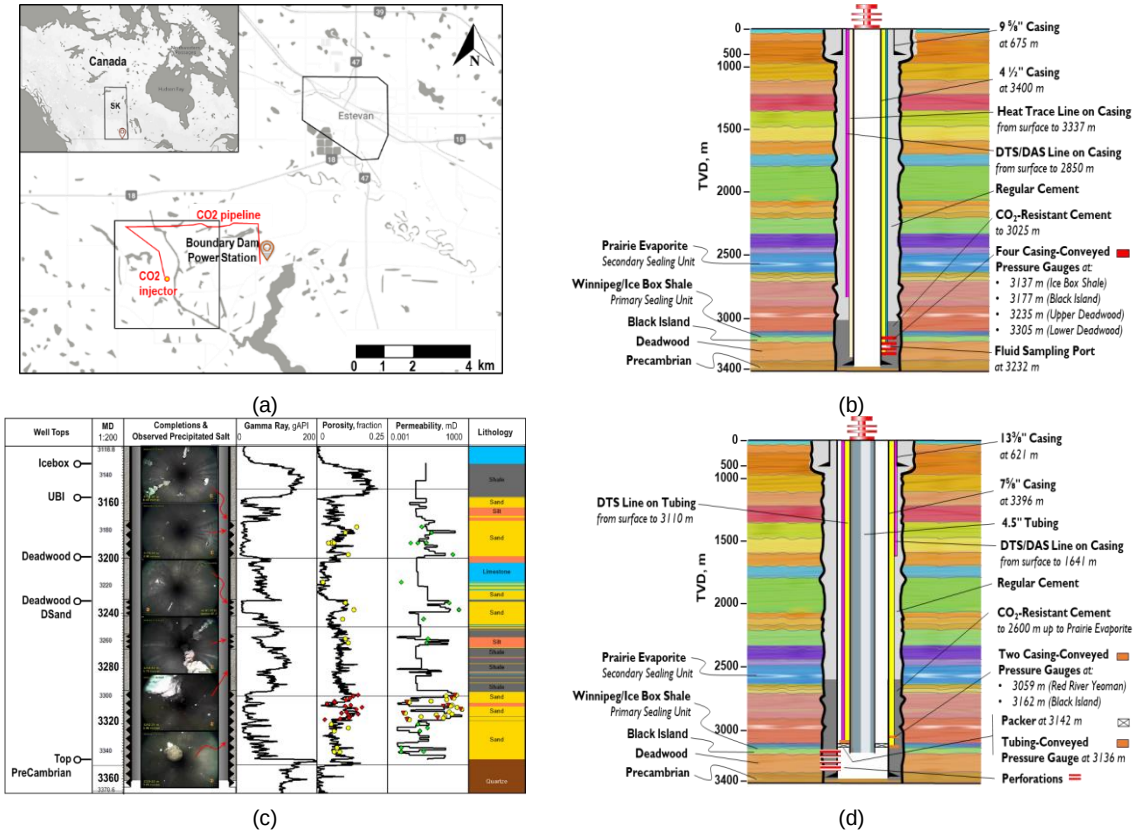

Figure 2: (a) Map of the Aquistore storage site with the locations of the Boundary Dam Power Station, CO_2 pipeline and CO_2 injection well, schematic of (b) the observation and (d) the injection wells, and some of the monitoring components installed at the Aquistore injection site, (c) an overview of the aquifer petrophysical properties from well logs (solid) and cores (points), four perforation zones, and the regions associated with salt scale in the injection well. Images in the tubing indicate salt precipitation observed from different depths during 2017 downhole inspection with the red arrows pointing to their approximate locations (from Rangriz-Shokri et al. 2021).

Estimated porosity values of 0.022-0.159 and permeability values of 0.002-312 mD are based on calibrated well logs and core data of sidewall and whole core samples from the injection well. The average initial temperature and pressure of the target aquifers are estimated to be ~115 °C and ~34.2 MPa, respectively, with brine salinity ranging from 271000-336000 ppm (Talman et al. 2020). The Aquistore storage capacity was estimated between 8 to 27 millions tonnes of CO_2 (Peck et al. 2014). Given that Aquistore is injecting CO_2 into deep (3.2 km > 2 km) hot (120 °C > 100 °C) and relatively transmissible formation (9000 mD-m > 5000 mD-m), it satisfies the minimum requirements of a CPG system and the CO_2 circulation test (Saar 2019; Adams et al. 2015).

The CO_2 injection operation started with a single injector on April 16th 2015. An observation well, 151 m away from the injector, was drilled to monitor CO_2 operation, such as formation pressure and CO_2 plume arrival. The observation well was cased with no access to the aquifer formations, except for the FRS (fluid recovery system) through a port that could take fluid formation samples on the outside of the casing (Zambrano et al. 2015; Rostron et al. 2014). Both injection and observation wells are highly instrumented and deploy multiple monitoring technologies, including permanently installed tubing- and casing-conveyed pressure and temperature gauges, Distributed Temperature Sensing (DTS) systems at multiple discrete locations, spaced approximately every 100 m, along the length of both wells, and wellhead gauges. The site is equipped with many surface monitoring systems, including 6 broadband seismometers, 630 permanently mounted geophones, tiltmeters, InSAR (Interferometric Synthetic Aperture Radar) reflectors, and numerous water/soil gas sampling stations to satisfy the monitoring, measurement, and verification program (Movahedzadeh et al. 2021).

Due to maintenance of capture plant and regional demand of CO_2 for EOR applications, the CO_2 injection at Aquistore has been intermittent, i.e. repeatedly stopped and started at varying injection rates and durations (Lee et al. 2018). Continuous monitoring of this intermittent injection operation at 1-minute frequency from multiple sensors has resulted in huge data in the form of numerous large spreadsheets; this makes it cumbersome to access, navigate, view, and analyze the full or a portion of the data set. We improved our previously developed Matlab® codes to extract and process the injection data at Aquistore, between April 2015 to April 2020, and to export data on a 24-hour resolution at both the injection and observation wells for numerical simulation and history matching purposes (**Figure 3-a**). Different modules of code were aimed to pre-process reported files, perform data quality checks, get daily-averaged values of the reported data, and to plot and export the required data in popular formats as direct input into CMG/ECLIPSE simulators for matching the injection history (Rangriz-Shokri et al. 2019, 2021).

2.2 Relevant Field Data Observations and Implications from Aquistore

Figure 3-(b) shows the history of volumetric injection rate, bottomhole pressure, and bottomhole temperature of the Aquistore injection well on a daily basis. Also shown is the heat map of DTS data along the length of the injector tubing, exhibiting multiple episodes of transient heat periods (blue shading for lower temperatures and red shading for higher temperatures). This section provides major observations from 5 years of injection operation relevant to the proposed CO_2 circulation study.

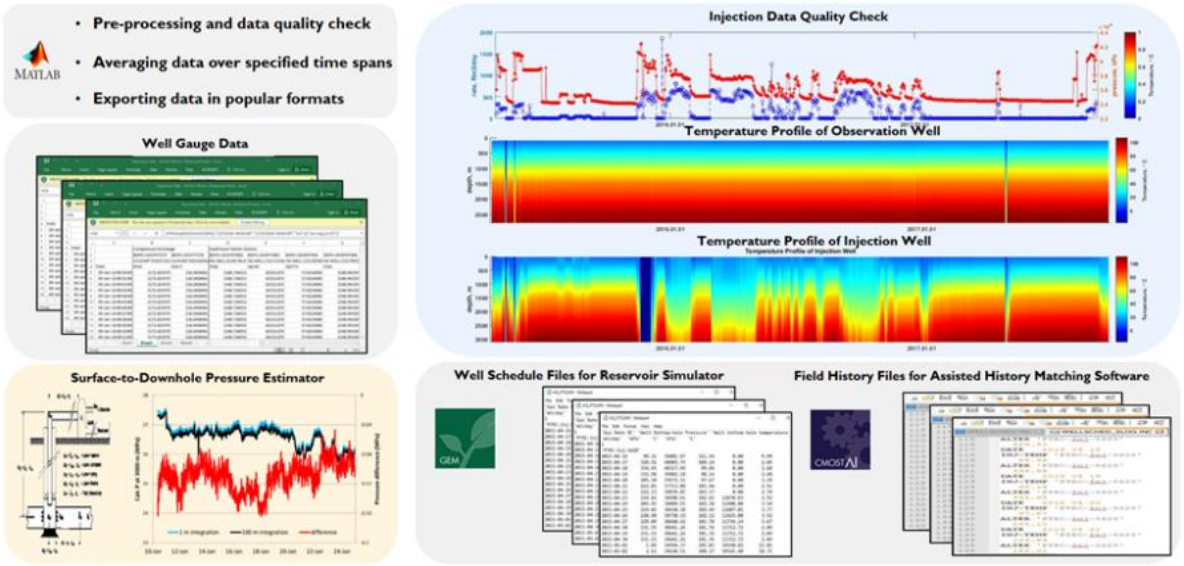

(a)

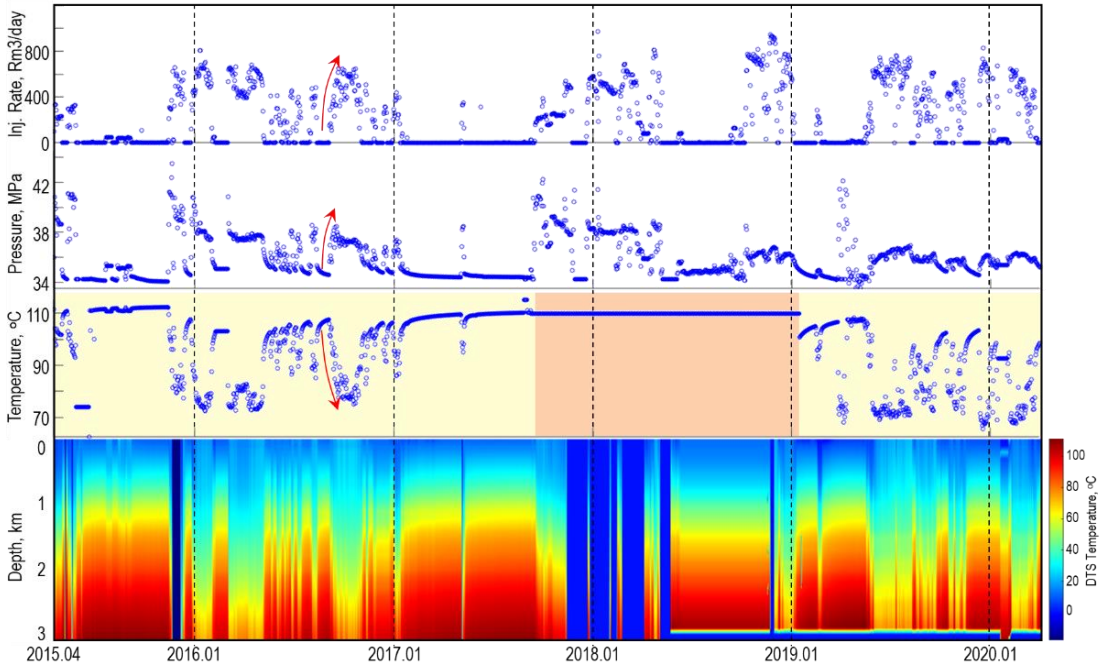

(b)

Figure 3: (a) Developed Matlab tool for field data pre-processing and quality check (from Rangriz-Shokri et al. 2019) (b) 5 years of the Aquistore injection history including volumetric injection rate, bottomhole pressure, bottomhole temperature, and DTS heat map, averaged at 24-hour interval. Note the episodic transient heat and flow periods. The orange box in temperature sub-plot indicates the main interval where downhole temperature gauge has apparently failed (Rangriz-Shokri et al. 2021).

2.2.1 Cooling Sequences of Storage Formation

Aquistore injects CO_2 at a lower temperature than that of the formation, referred to as cold CO_2 injection. That is why the bottomhole temperature decreases in response to CO_2 injection, and temperature reduction is amplified by higher injection rates and longer injection periods (cooling cycle). The bottomhole temperature rises towards the initial formation temperature (warming cycle) when the well is shut in. Inspection of the 5-year CO_2 injection history suggests that the bottomhole temperature never reaches the initial value even after several extended periods of shut-in. This means CO_2 injection appears to have caused long-lasting cooling of subsurface formation, at least around the injection well. Because of the intermittent nature of CO_2 injection, our analysis suggests that variability in bottomhole temperature at Aquistore is more rate-dependent than a result of seasonal variations of surface temperature. We observe that every increment of 100 tonnes/day in injection rate temporarily reduces the bottomhole temperature by 5.9 °C (**Figure 4**).

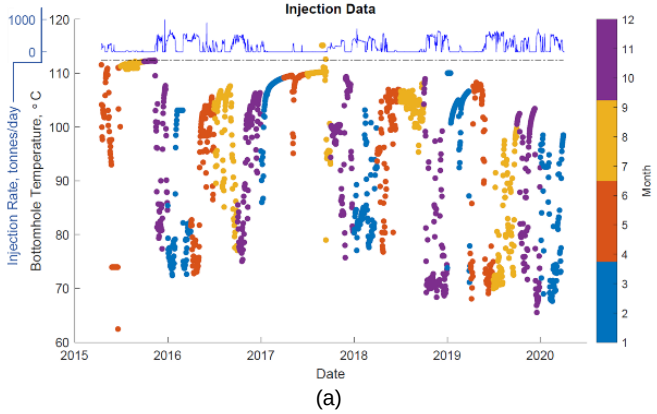

(a)

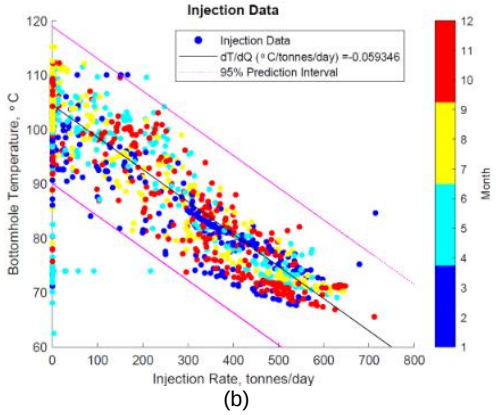

(b)

Figure 4: (a) Variation of bottomhole temperature due to intermittent cold CO_2 injection; higher injection rate and duration reduce the bottomhole temperature. Note the bottomhole temperature never rises back to the initial reservoir temperature of ~112 °C, denoted by dashed line in black, an evidence of reservoir cooling down. Also shown is the little to no impact of seasonal variation on CO_2 injectivity. (b) bottomhole temperature response to cold CO_2 injection rate, color-coded by season (Rangriz-Shokri et al. 2021)

2.2.2 Pressure Increase of Storage Formation

Bottomhole pressure is measured at the depth of 3136 m down the injection well by means of a tubing-conveyed gauge. When late pressure falloffs are compared with initial bottomhole pressure (34.2 MPa shown with a black dashed line) in **Figure 5**, the bottomhole pressure appears to never reach its initial value and a time-dependence in the average reservoir pressure is manifested. Of interest is the magnitude of pressure increase before and after mid 2018 – because of a workover operation. The Aquistore injection history indicates that the increase in average reservoir pressure is insignificant and it does not negatively affect storage capacity and subsurface containment. The decrease in magnitude of pressure drop after the workover is of interest and might be caused due to a combination of the creation of localized fractures and/or mobilization of precipitated salts, among other factors; this needs to be further investigated.

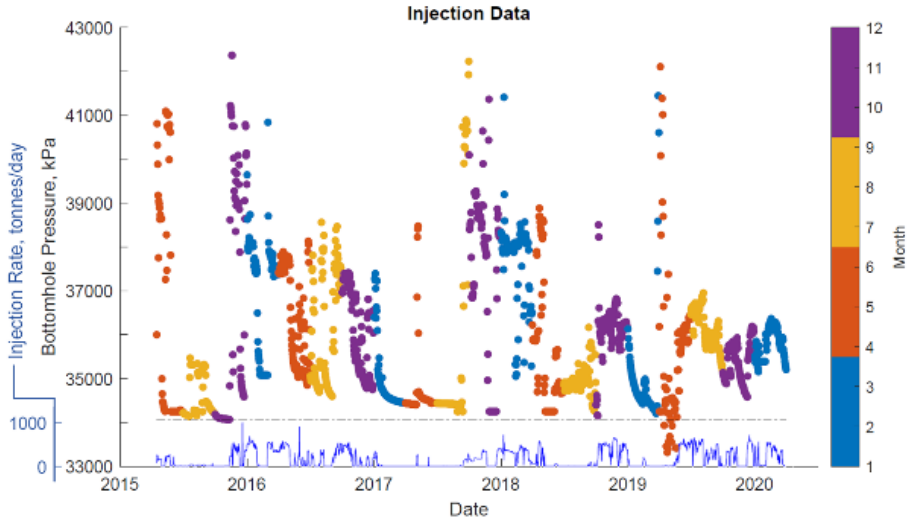

Figure 5: Variation of bottomhole pressure due to intermittent cold CO_2 injection; higher bottomhole pressures are attributed to larger injection rate and duration. Note the bottomhole pressure never returns to the initial reservoir pressure of 34.2 MPa, denoted by dashed line in black, an evidence of reservoir pressurization. Also shown is the little to no impact of seasonal variation on CO_2 injectivity (Rangriz-Shokri et al. 2021).

2.2.3 Wellbore Thermal Profiling of CO_2 Injection from DTS Data

Figure 6 provides the variability of 24-hourly averaged temperature data, over 5-year operation, from DTS lines along the length of the tubing of the injection well, and the casing of the observation well. Because the DTS lines do not cover the targeted CO_2 storage interval, it is not possible to profile the injection flowrate in the perforated zones. The thermal profile of the injection well is primarily controlled by the temperature of the injected CO_2 stream and average wellbore temperature, the magnitude of rate and duration of CO_2 injection, thermal properties of the injected CO_2, phase behaviour, and the heat transfer between wellbore and surrounding formation rock/fluids (Ramey 1962; Willhite 1967).

The Aquistore data suggest that establishing a constant injection temperature at the injector perforations could take a sufficiently large amount of time due to the intermittent nature of CO_2 injection. The DTS data of the observation well shows no substantial variability at deeper formations and follows closely the local geothermal gradient. This suggests that heat loss associated with CO_2 injection is limited to a localized medium immediate to the injector due, for instance, to the low thermal conductivity of formation

rock/fluids, the extent of the surrounding formation between the two wells, among other things (Rangriz Shokri et al. 2019, 2021).

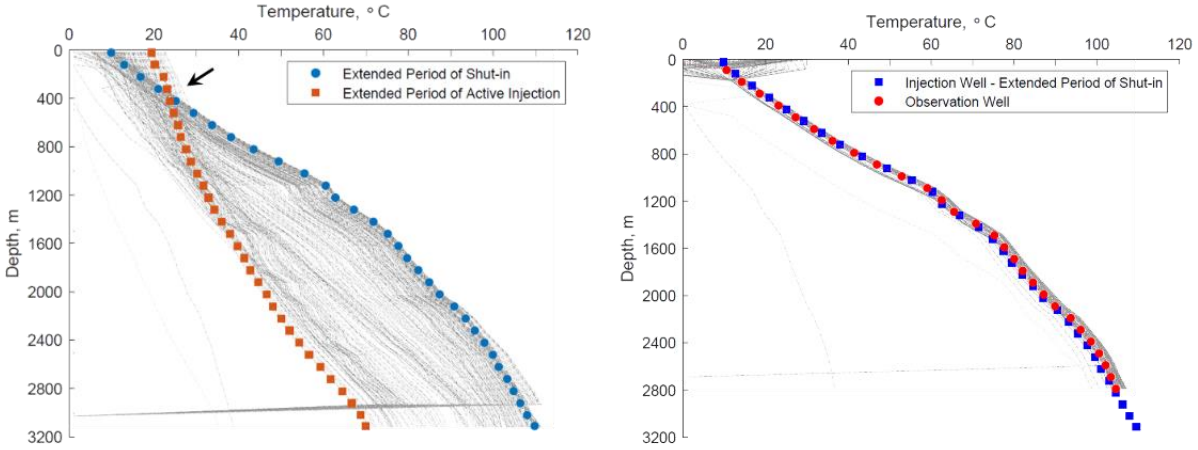

(a) (b)

Figure 6: Variability of 24-hourly averaged temperature data from DTS along the length of (a) injection and (b) observation wells during 5 years of CO_2 injection (Rangriz-Shokri et al. 2021).

2.2.4 Non-isothermal Evolution of CO_2 Injectivity

Figure 7 is the plot of the temporal evolution of injectivity behaviour indicators, as well as the number of days in each month when CO_2 injection operation was considered active. Despite its variability, injectivity appears to increase with time. Eliminating the continuous time scale, there seems to be a correlation between the injectivity behaviour indicator and the number of days with relatively consistent average CO_2 injection rates; in general, injectivity improves as injection continues.

Mixed behaviour of injectivity gain and loss could be perceived in warm and cold seasons. It appears that injectivity data could be grouped into three clusters with distinct injectivity statuses: inferior (~0.01 tonnes/day/kPa), moderate (~0.1 tonnes/day/kPa), and exceptional (~1.0 tonnes/day/kPa) levels. These descriptors are at a scale unique to the Aquistore site; the magnitude of injectivity in other storage sites might differ significantly as they depend on site-specific details such as formation petrophysical properties and injector operating conditions. Overall, CO_2 injectivity has a strong inverse correlation with bottomhole injection temperature.

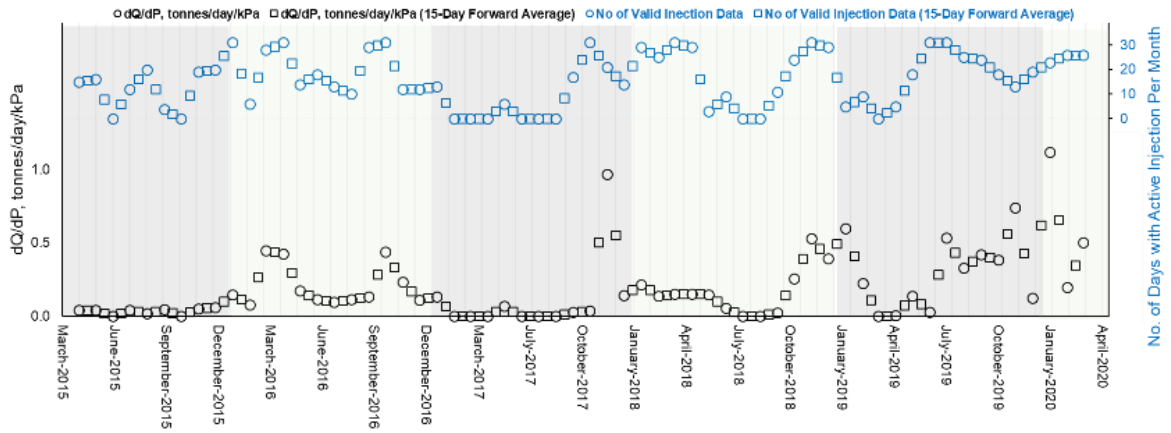

(a)

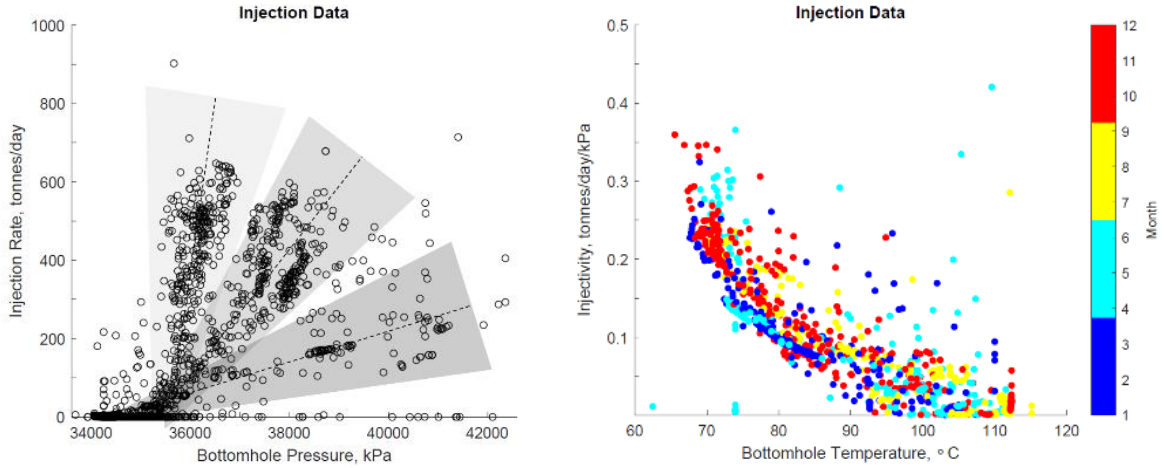

(b) (c)

Figure 7: (a) Illustration of the temporal evolution of monthly-averaged injectivity behavior indicator (black) along with number of days (blue) of active injection per month, (b) identifying three clusters with distinct injectivity status, of inferior (~0.01 tonnes/day/kPa), moderate (~0.1 tonnes/day/kPa), and exceptional (~1.0 tonnes/day/kPa) levels at a scale unique to the Aquistore site, and (c) recognizing an inverse relation between injectivity performance and bottomhole temperature labelled by season (Rangriz-Shokri et al. 2021).

2.2.5 Salt Precipitation within the Injection Well

The formation brine of Aquistore is a very saline (TDS 330 g/L) Na^+, Ca^{2+}, Cl^- rich brine with chloride as the dominate anion, >99.8 mole% of anions in solution, with water at, or near, saturation with halite and anhydrite at reservoir conditions (Talman et al. 2020). **Figure 8** provides an overview of well salt precipitation, where the second perforated zone (PERF 2) exhibits the lowest amount of precipitation. This perforation zone is associated with relatively homogeneous, high permeability, strata in the aquifer.

Significant scale development is associated with the lowest injectivity and the third perforation zone (PERF 3). This observation suggests that brine back-flow into the wellbore is related to permeability variations in the near-wellbore region, arising from complex interactions between mechanical responses, capillary forces, and chemical potential gradients. Pressure driven flow back into the well, during low injection-rate episodes, can provide a source of brine into the wellbore (Talman et al. 2020). Salt precipitation has the potential to negatively affect CO_2 injectivity.

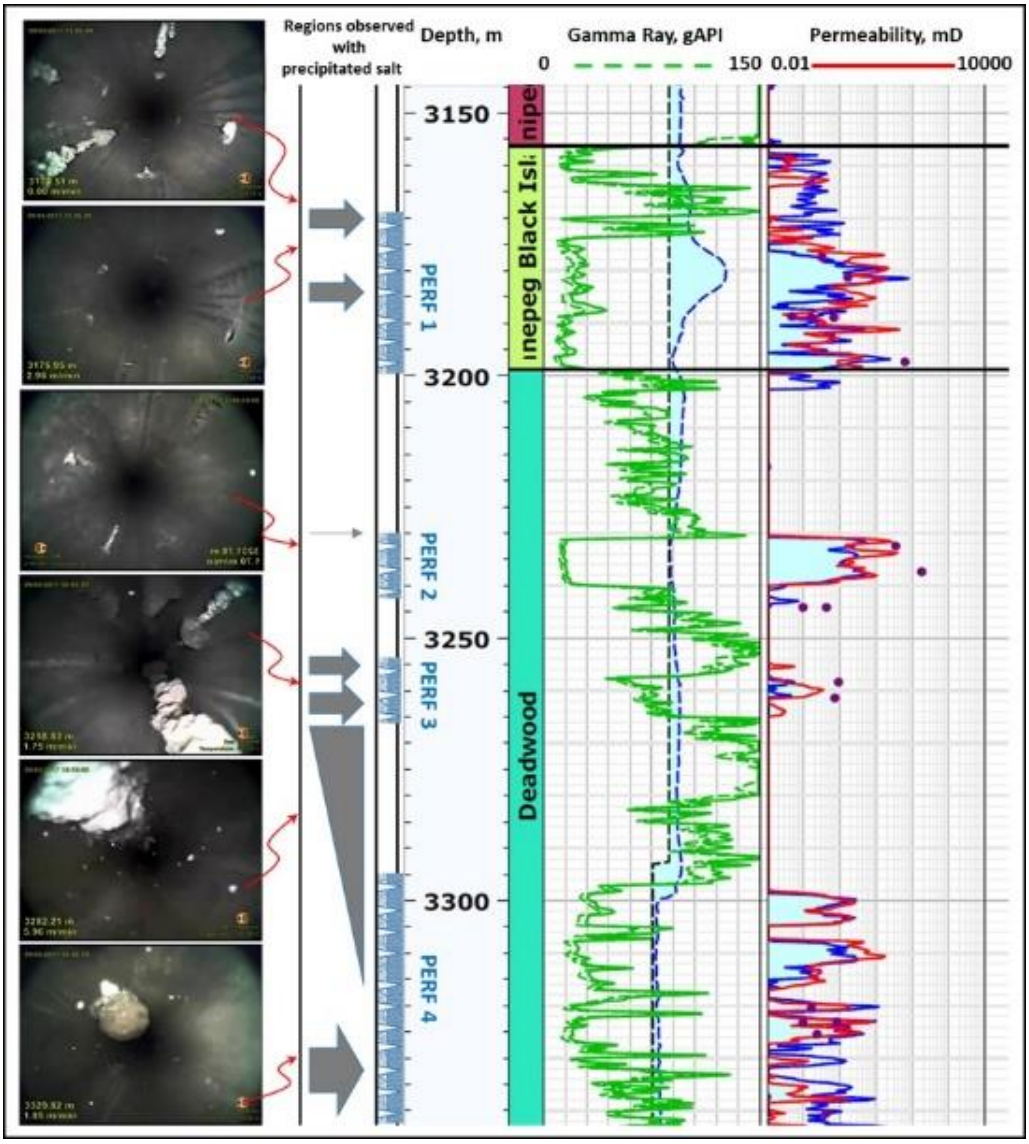

Figure 8: An overview of the aquifer physical properties and regions associated with salt scale. Images from different depths are shown at the left with the red arrows indicating their locations. The grey shapes indicate general locations where there is salt buildup. An indication of the location volume of the deposits is given by the grey zones (Talman et al. 2020).

3 Procedures and methodology

In this work, we initially appraised the most probable realizations of CO_2 plume extent from history matched numerical simulation and four seismic monitor surveys at the Aquistore. We then extracted and re-built a high-resolution sector model from the developed full geological model to represent the geology near the existing injection and observation wells. Given the extensive field evidences of CO_2 breakthrough at observation well, we employed non-isothermal simulation tools to perform uncertainty assessment of a pilot CO_2 circulation test between injector and producer (i.e. observation well), followed by assessment of flow regimes during CO_2/brine co-production at the producer.

3.1 Extract and Build a Base Sector Model

3.1.1 Full Field Static Geological Model

The initial full geological model was constructed by Schlumberger for a feasibility study in 2012 and then improved by EERC (Peck et al. 2014). Building on these available models, we revisited the geological model and constructed our own version of the full geological model in Petrel. We incorporated the available geological and geophysical data; they include well data (paths, logs, cores), and the interpreted seismic horizons in depth domain (Geological Survey Canada, White 2018). We adopted metric units and the coordinate reference system of NAD83 Zone 13N. Depth, from gamma ray well logs, selected as the reference to position the interpreted seismic horizons alongside the associated well tops of injection and observation wells and to correct seismic depth mismatch. The full geological model was constructed from the Winnipeg Icebox to the Precambrian erosional surface, on a 5km x 5km region associated with the Aquistore seismic monitoring activities (**Figure 9**).

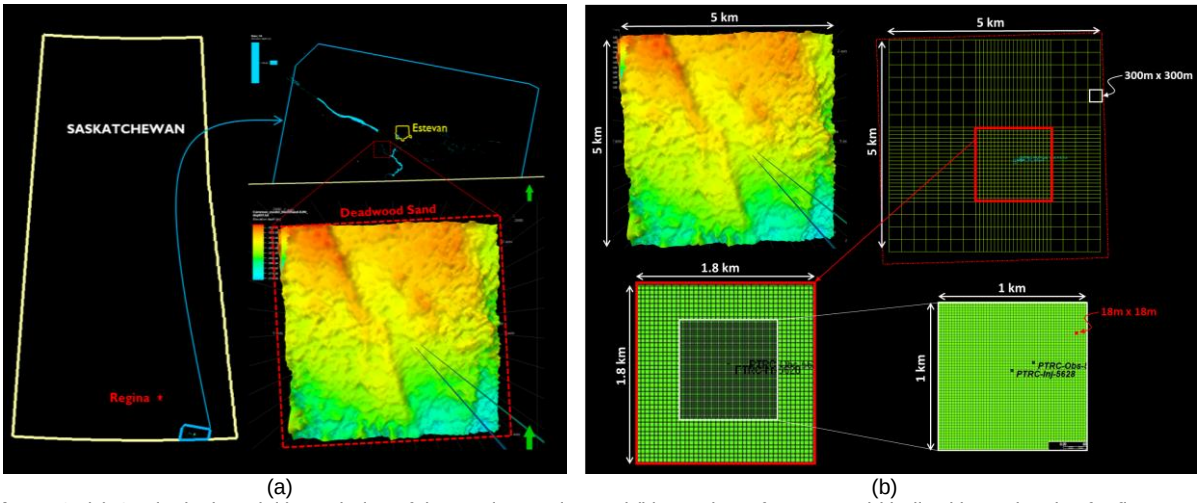

(a) (b)

Figure 9: (a) Geological model boundaries of the Aquistore site, and (b) top view of a tartan grid built with two levels of refinement around the injection and observation wells (Rangriz Shokri et al. 2019)

We used log data (e.g. shale volume index, lithology, and porosity logs) and the knowledge of southern Saskatchewan geology to divide the storage formations into several subdivisions. Each geological subdivision was assigned different numbers of layers. Layering was aimed to honor the vertical heterogeneity (sand vs. shale zones) and to more accurately distribute petrophysical properties (Peck et al. 2014a; Rangriz Shokri 2019). **Table 1** summarizes the zones and distribution of vertical layering in the static model.

Table 1: Distribution of vertical layers, perforated intervals, and rock types in different geological zones

Geological Zone Division	Number of layers	Perforation Status	Relative Permeability Set Number
Icebox	2	None	3
Upper Black Island Sand	4	None	3
Upper Black Island Shale	2	None	3
Lower Black Island Sand	14	Perforated	2
Upper Deadwood – Non Reservoir	6	None	3
Deadwood D Sand	6	Perforated	1
Deadwood D Shale	3	None	3
Deadwood C Sand	5	Perforated	1
Deadwood C Shale	3	None	3
Deadwood B Sand	3	None	3
Deadwood B Shale	2	None	3
Deadwood A Sand	24	Perforated	1 and 3 – as explained in the text.

We performed a quality check on the structural surfaces, interpreted seismic horizons, and well tops, and then, generated a tartan grid for reservoir simulation (5km x 5km) with one level of refinement in a region of 2km x 2km in x-y directions around the injection well. This step was intended to re-build the

model to suit the CO_2 circulation feasibility study. The dimensions of the local refined area were estimated based on sensitivity analysis of the possible extent of CO_2 plume from previous knowledge of history-matched simulations and time-lapse seismic surveys (Rangriz Shokri 2019; White et al. 2021). Grid cell sizes were 32m x 32m near the wells and 250m x 250m close to the model boundary. As detailed in next section, we later refined the 32m x 32m grids a second time into 4m x 4m grids in Petrel. This was done to have a high-resolution sector model as the input to CMG-GEM simulator. This model helps to better compute mass and heat transport in the CO_2 plume region during the CO_2 circulation test.

Analysis of well logs from both injection and observation wells (151 m apart) indicated similar rock types and shale/sand sequences (**Figure 10**). We estimated the petrophysical properties from well logs, calibrated with core data for the injection well. Density, porosity, gas and liquid permeabilities of 20 core plugs were previously measured in the laboratory on the full diameter cores. Routine core analyses of 22 side wall core samples were also available. A depth correction was made to match logs and core data. Porosities ranged from 0.022 to 0.159, and permeabilities ranged from 0.002 to 312 mD, for the whole intervals (Figure 8) with an assumed vertical to horizontal permeability ratio (k_v/k_h) of 0.1. The permeability log was from calibrated porosity-permeability correlations from EERC (Peck et al. 2014; Rostron et al. 2014; White et al. 2016); the correlations were based on permeability data from the Deadwood cores measured at the North Dakota Geological Survey core library facility.

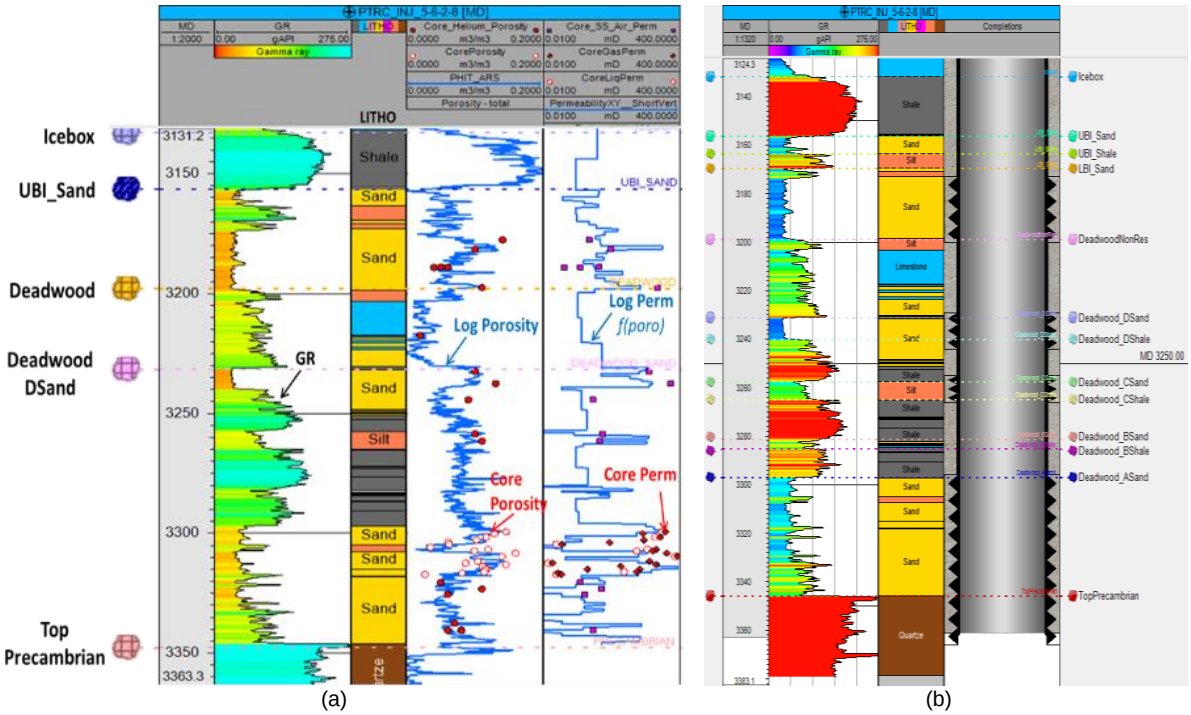

Figure 10: (a) Computed petrophysical data from well logs and core measurements of the injection well and (b) four different intervals perforated in the injection well (Rangriz Shokri et al. 2019)

Since the model was constrained by only two line sources (i.e. the injection and observation wells), the porosity and permeability data were initially distributed within a layer cake model. In the layer cake model, we directly assigned each property throughout the whole individual horizontal layer from these two wells. The layer cake assumption is useful for simplified modeling where heterogeneity in only vertical direction for petrophysical properties is of significance. Other realizations of petrophysical property distributions are addressed in section 4, using vertical variograms from well logs, synthetic horizontal variograms from seismic data, and random distribution generated by the Gaussian simulations.

3.1.2 Presence of a Flexure in Precambrian Basement

Prior to drilling the injection well and during the site screening/characterization phase, an initial pseudo 3D geophysical model (8km x 6km) was generated over the Aquistore injection site. The pseudo 3D model was constructed based on six available legacy industry 2D seismic lines in the region (**Figure 11-a**). This initially helped with characterization of the underlying Precambrian basement, but it showed no clear evidence of vertical faults, fractures, or any missing reservoir horizons over the injection site (Rostron et al. 2014).

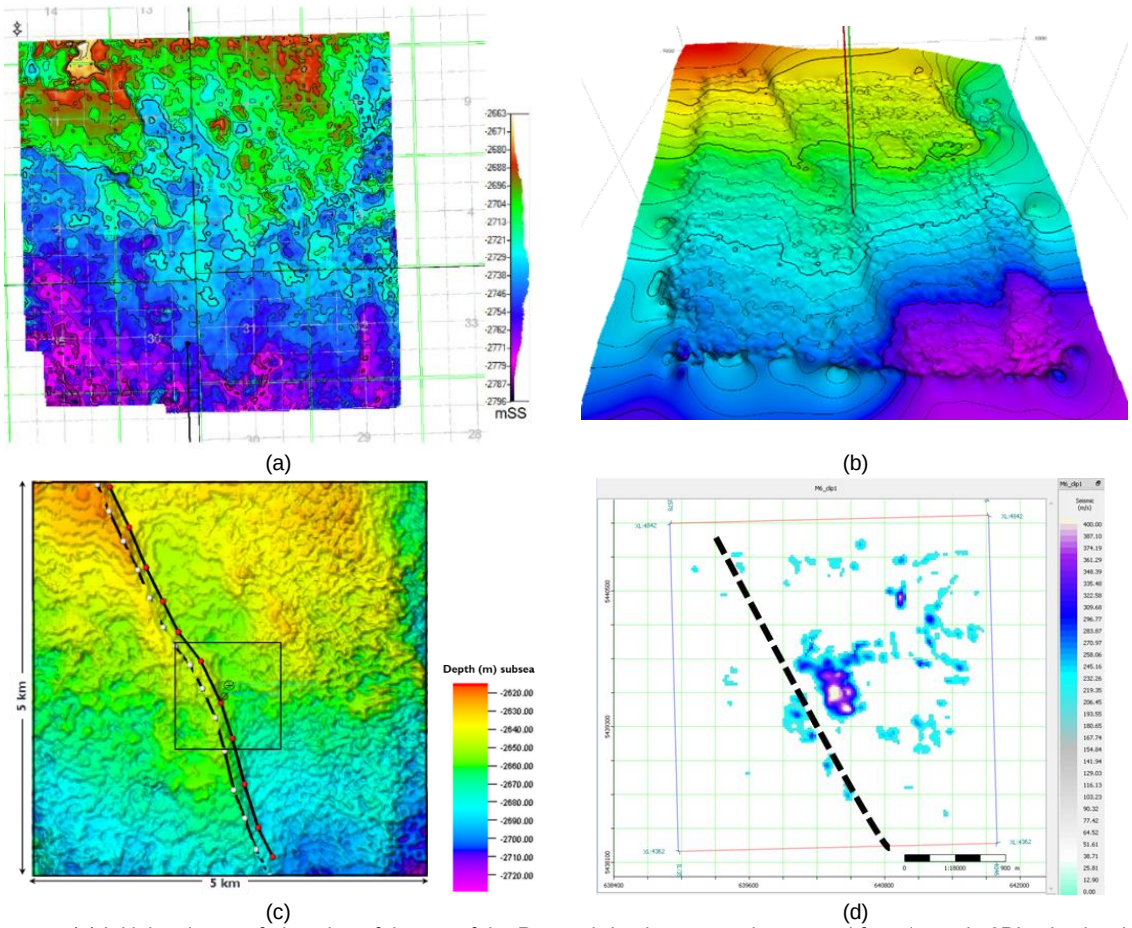

Figure 11: (a) Initial estimate of elevation of the top of the Precambrian basement, interpreted from 'pseudo 3D' seismic, shows no flexure (Rostron 2014), (b) detection of flexure in subsequent high quality seismic surveys, (c) uncertainty associated with locating the flexure in interpreted depth horizon, and (d) CO_2 plume outline from 4D seismic monitor surveys; the flexure seems to control the migration of CO_2 plume.

After acquisition of a detailed 3D seismic volume, and its interpretation in connection with other geological/geophysical logs from the Aquistore injection well, a local sub-vertical Precambrian basement fault-like structure (referred to as flexure) was noticed (**Figure 11-b**). The NNW-SSE flexure (fault-like structure) is ~1km away from the injection well and is oriented at an azimuth of 75°–85° relative to the regional maximum horizontal stress. Because of its location and orientation, the flexure seems less susceptible to reactivation during CO_2 injection (Rostron et al. 2014). No clear evidence is available to support if the strata in the overlying flexure are faulted; the nearest known significant fault zone was determined to be located ~200 km away (White et al. 2016).

The 4D seismic surveys over the Aquistore injection site suggest that the CO_2 plume propagates in a certain direction; its propagation has been evidently controlled by the presence of the flexure structure (**Figure 11-d**). The interpreted CO_2 plume is asymmetric in shape and it appears to be propagating mainly northward from the injection well. Basic analysis indicates that this might be the result of a combination of factors, including the regional dip (SSE direction), the predominant oriented flexure

structure (NNW-SSE) and/or porosity/permeability distribution/anisotropy in the Deadwood formation (White et al. 2018, 2019, 2021).

3.1.3 Resampling AVO Inversion Volumes and Constraining Petrophysical Data to Acoustic Impedance

Schlumberger delivered the 3D AVO inversion volumes in time domain to PTRC for subsequent lithology prediction and porosity estimation for the Aquistore reservoir interval (Schlumberger 2018). Because of a significant acquisition footprint in the data, White (2018) applied azimuthal (kx-ky) filtering directly to the AVO inversion 3D volumes as well as the original lithology and porosity sub-volumes; the filtering process largely suppressed the acquisition footprint (White 2018; Marfurt et al. 1998). We received the AVO inversion volumes and subsequent lithology products in NAD83 UTM coordinates, where the volumes were converted to depth using the Strata model constructed by Dr. Don White of Geological Survey of Canada. The model was constructed using the injection well log data and the seismic horizons (White 2018). The seismic inversion volume in depth domain (mainly acoustic impedance) was imported to the Petrel model of the Aquistore site; it was depth corrected, and resampled to the existing tartan grid for the CO_2 circulation test (**Figure 12**)

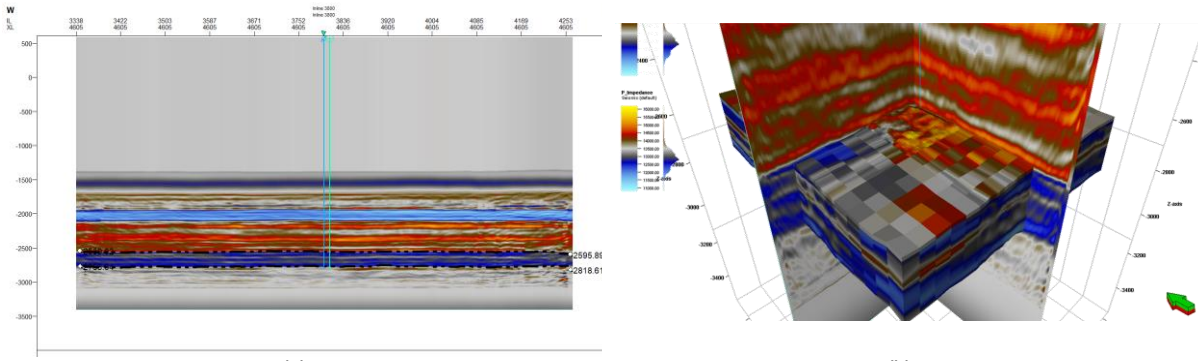

(a) (b)

Figure 12: (a) P-wave acoustic impedance from seismic inversion volume in depth domain, (b) importing the acoustic impedance, applying depth correction, and resampling it to the existing tartan grid to suit CO_2 circulation study.

To have a reliable estimation of spatial distribution of porosity, and to improve our earlier layer cake model, we took advantage of seismic inversion data, mainly the acoustic impedance. We assumed there is a negative correlation between porosity and acoustic impedance that can be defined through a single transform function (Batzle and Wang 1992). The porosity was populated using the Gaussian random function simulation, a stochastic method, so that many realizations could be produced if needed. During the Gaussian simulations, we honored well data, input distribution, and variograms from injection and observation well logs. We incorporated the knowledge of P-wave acoustic impedance volume, as a secondary variable, through collocated co-kriging with an initial correlation coefficient of -0.8 in the petrophysical modeling process. This initial value was estimated based on porosity and acoustic impedance data of the injection well. The correlation coefficient was later treated as a variable in the uncertainty workflow of section 4 to generate multiple-realizations of porosity-permeability volumes. **Figure 13** shows the acoustic impedance, and the stochastic distribution of porosity with and without constraining the porosity distribution to the P-wave acoustic impedance volume.

Given limited data from cores and well logs, cross plots of porosity vs. permeability for available facies were generated (Peck et al. 2014a; Rangriz Shokri 2019). We used the porosity-permeability cross plots per facies as secondary variables to populate the permeability in the model; the process honors well data (**Figure 13-e**). As a result, permeability distribution is a function of both the permeability of wells, their correlation with porosity at the wells, and the acoustic impedance volume; the latter is because the porosity has been already constrained to the acoustic impedance in a previous modeling step. **Figure 13** also illustrates the permeability distributions along with the assumed porosity distributions.

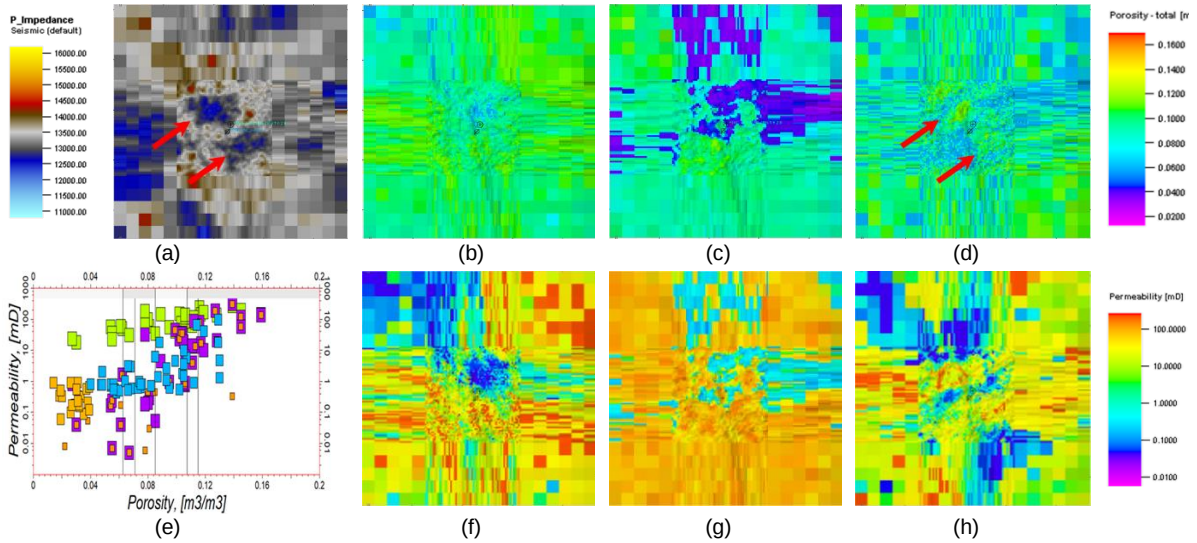

Figure 13: Top view of 5 km x 5 km of the Deadwood D formation (a) P-wave acoustic impedance, (b) stochastic distribution of porosity and its relevant (f) permeability, (c) distribution of porosity from EERC's model and its relevant (g) permeability, (d) distribution of porosity constrained to acoustic impedance and its relevant (h) permeability, and (e) cross-plot of porosity-permeability for different rock type/facies from core data and well logs of Aquistore injection well.

3.1.4 Reservoir Dynamic Simulation Model for History Matching Process

We used the CMG Compositional Simulator (CMG-GEM) to build a non-isothermal flow model and to match the CO_2 injection history of the Aquistore injection well in the targeted saline formations, and its breakthrough at the observation well. We selected the Peng-Robinson equation of state with two-component fluid system of brine and CO_2; but trace amounts of a third component (methane 0.00001 mole fraction) were added for numerical stability reason. The CO_2 was allowed to dissolve in brine. The solubility of CO_2 in brine was estimated by Harvey's correlation in pure water and corrected for salinity effect (Harvey 1996). The correlations to calculate brine density (Rowe and Chow 1970) and viscosity (Kestin et al. 1981) were also implemented in CMG-GEM simulator. The aquifer was initially assumed to only contain brine (Sw=1) with salinity ranging between 271000-336000 ppm (Peck et al. 2014b). The pore pressure gradient was reported as 10.4-10.63 kPa/m, increasing from north to south, with a value of 10.7 kPa/m interpreted from well tests conducted in the Deadwood Formation (White et al. 2016). The model was initialized with 34129.05 kPa and 112.8 °C at a reference depth of 3173 m. The outer boundary of the full geological model was connected to an analytic infinite acting aquifer from all sides. The simulation runs were non-isothermal (Rangriz Shokri et al. 2019).

We used three sets of drainage relative permeabilities for different rock types (**Figure 14**), available from multiple sources including Kruz et al. (2014), Schlumberger (2013), and Bennion and Bachu (2006a,b). Relative permeability data from Schlumberger was sourced from unsteady-state CO_2 gas/CO_2 equilibrium brine relative permeability tests performed on a composite core stack composed of three core plugs (Schlumberger 2013). Relative permeability data of Bennion and Bachu (2006a,b) were derived from three basal Cambrian sandstone formations in the Wabamun Lake area southwest of Edmonton, Alberta (Peck et al. 2014a). We assigned heterogeneity to relative permeabilities of high quality sand zones and poor shale sequences with zero capillary pressures (Jiang et al. 2016); the effect of capillary pressures and entry pressures were ignored. A summary of the allocation of rock types to different zones is provided in **Table 1**.

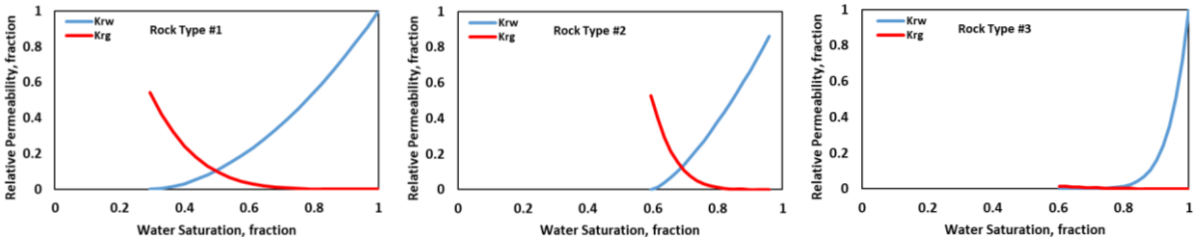

(a) (b) (c)

Figure 14: Three sets of relative permeability used in the flow simulation (Peck et al. 2014a) from Bachu and Adams 2003, and Bachu et al. 2011 for (a) basal Cambrian sandstone, (b) Wabamun carbonate, and (c) shale.

We modeled CO_2 injection into four different perforated intervals of the injection well (**Figure 10**). These include:

- Perforation 1 in Lower Black Island;
- Perforation 2 in Deadwood D Sand, and approximately 1 meter of overlying Upper Deadwood Silts and 2 meters of underlying Deadwood D Shale;
- Perforation 3 in the Deadwood C Sand which to some extent penetrated the overlying Deadwood D Shale;
- Perforation 4 in entire Deadwood A Sand, and extended about 15 meters into the Precambrian formation.

A spinner survey of the injection well indicated that more than half of Perforation 4 at the bottom and the entire of Perforation 3 might not contribute to CO_2 injection (assumed plugged/non-effective). 45-50% of injection occurred at the upper section of Perforation 4, while Perforation 2 and 1 took in approximately 40-45% and 10% of injection, respectively (Schlumberger 2015) (**Figure 16**). Reports are available on brine injection tests that were conducted to obtain bulk well injectivity estimates. The tests were conducted subsequent to completion of the injection well and prior to initial CO_2 injection. For the plugged perforations, Jiang et al. (2016) suggested that this previous water injection during well testing might have caused clay content swelling in the formation, substantially reducing the permeability near the wellbore. Other opinions were made on the possibility of spinner malfunction because the precipitated salts might have fallen into the spinner, resulting in the spinner not operating properly. A summary of parameters used in constructing the geological model and setting up the flow simulation, is included in **Table 2**.

Table 2: Summary of flow simulation parameters

Parameters	Values
Initial reservoir pressure, kPa	34129.05 at 3173 m MD
Pressure gradient, kPa/m	10.7
Initial reservoir temperature, ˚C	112.8 at 3173 m MD
Initial water saturation, fraction	1
Brine salinity, ppm	300000
Porosity, fraction	0.002-0.105
Permeability, mD	0-312
Permeability anisotropy (k_v/k_h)	0.1
Reservoir boundary	Analytic infinite acting aquifer
Equation of State	Peng-Robinson
Default run type	Non-isothermal

3.1.5 Appraise the Most Probable Realizations of CO_2 Plume Extent and Shape

We used the non-isothermal option of CMG-GEM simulator to match the daily averaged values of injection rate, pressure, and temperature from the Aquistore injection well. Skin factor was selected as the key history matching parameter, with the assumption that the skin factor is not a constant number.

A change in the well skin factor might indicate changes in phase behaviour, flow regime, fluid/rock interactions, thermal fractures, plugging of perforations, and/or salt precipitation, among others. To honor the spinner log, negative values of skin were required to match the injection history, mostly in periods where high injection rate and high injection pressure resulted in significant temperature drops in the near wellbore region. These periods could provide favorable conditions for localized thermal fracturing due to stress alteration, augmented by cooling effects (around 50˚C change in temperature and 10 MPa change in pressure); this might result in near wellbore permeability enhancement (Rangriz Shokri et al. 2019; Jiang et al. 2016).

Figure 15 shows the results of history matching of the CO_2 injection; observed field data are shown by circles and simulated data by solid lines. There are multiple transient heat/flow periods – non-isothermal cycles – where an increase of injection pressure results in an increase in the injection rate. Because the temperature of injected CO_2 stream is lower than that of the target formations, more volumes of injected CO_2 cause the downhole temperature to drop. When CO_2 injection rate occurs at lower values or comes to a stop, injection pressure drops to values close to initial reservoir pressure, and temperature rises back to values close to initial reservoir temperature. In a previous study, we suggested that non-isothermal effects are significant, especially in the periods where injection rates are significantly high, and they should be considered for more accurate modeling of cold CO_2 injection at Aquistore (Rangriz-Shokri et al. 2019).

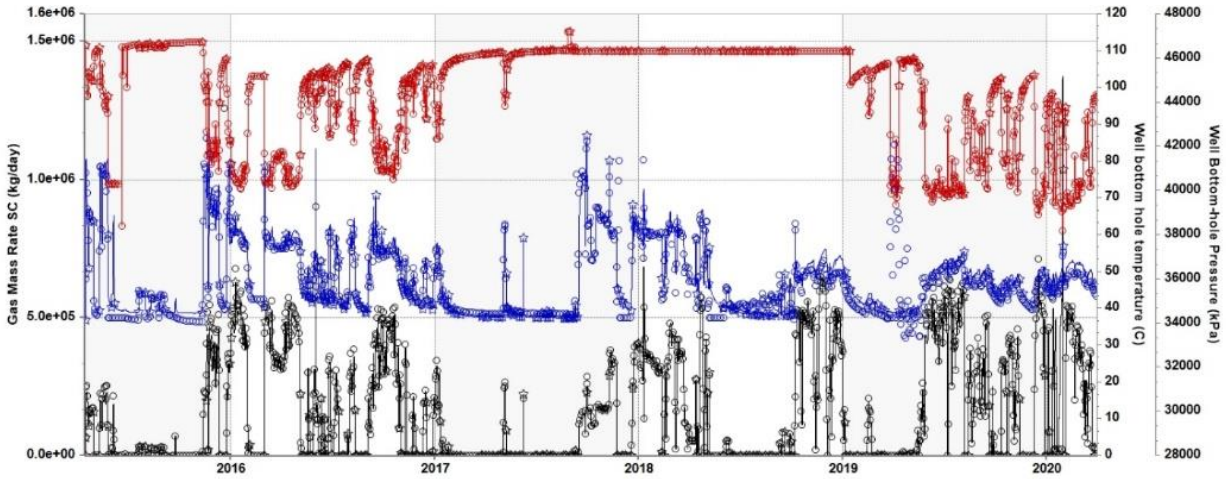

Figure 15: Matching the injection history in non-isothermal simulations; simulated data (solid lines) vs. observed data (circles); red temperature, blue pressure, black mass rate.

Figure 16-(a) shows a comparison of the spinner survey of the injection well conducted by Schlumberger in 2015 and an equivalent simulated spinner log during the history matching process. The spinner log demonstrates how injected CO_2 was allocated in different perforations. If the knowledge of the spinner survey is trusted, some perforations should be assumed plugged/non-effective. Honoring the spinner survey in the history matching process, the shape and extent of the CO_2 plume differs from the case where all four perforations are assumed open to receive CO_2.

Further calibration includes the knowledge of CO_2 breakthrough at the observation well (151 meters away from the injector). The CO_2 breakthrough was determined through an inspection of numerous pulsed neutron logs. The pulsed neutron logs were aimed at monitoring near fluid saturation changes at the observation well and their results (Reservoir Saturation Tool from Schlumberger) are illustrated in **Figure 16-(b)** (Swager 2017). Interpretations suggest a major change in CO_2 concentration occurred between December 2015 and March 2016 (Kennedy 2017). Close inspection of the interpreted data indicates on February 2016, a significant change of CO_2 saturation was noticed in the observation well, at depths close to Perforation 2 of the injection well. When the spinner survey was included in the history matching process, the first CO_2 arrival appears to occur at the depth of Perforation 2.

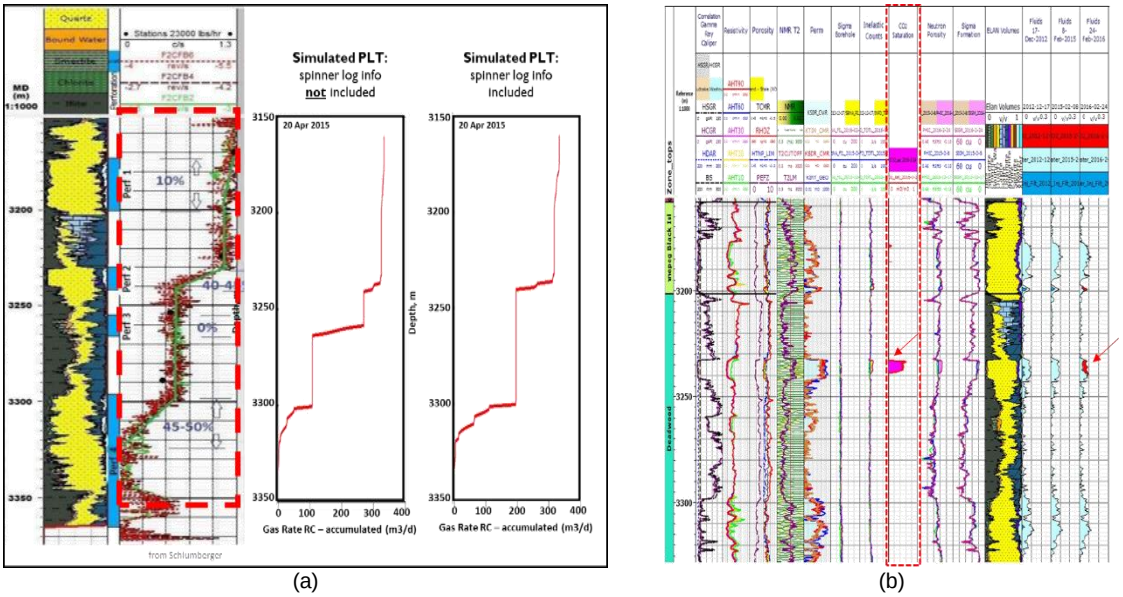

(a) (b)

Figure 16: (a) comparison of field measured spinner survey with simulated spinner logs when perforation 3 is assumed open, and/or plugged (Schlumberger 2015), (b) arrival of CO_2 in the observation well from Reservoir Saturation Tool (RST) by Schlumberger.

In the history-matching period, we assumed an infinite acting regional aquifer as the default boundary condition; however, the leaking capability of the regional aquifer is unknown. Leaking is a terminology used by the CMG simulator. The leakage of an aquifer, in this context, means the ability of water to leak back into the aquifer when under the influence of a higher reservoir pressure. Although the degree of the aquifer's leaking property was not fully investigated, the simulation results confirmed that for an identical amount of cumulative volumes of injected CO_2, the average pressure in the target formations would significantly increase for a non-leaking confined aquifer. Since we do not experience such high average reservoir pressures, the assumption is that the capacity of the regional aquifer is significantly larger than the amount of CO_2 injected. This is of significance for future brine injection/disposal wells to control the CO_2 plume. A significant increase in average reservoir pressure could adversely affect the onset of hydromechanical failure in the target zones, constrain the storage capacity, and jeopardize the containment of the storage complex within the saline formation.

4D seismic monitoring is one of the key components of the measurement, monitoring, and verification program at the Aquistore site (Movahedzadeh et al. 2021). 4D seismic surveys have been acquired at Aquistore since 2012 with a baseline survey prior to CO_2 injection. Additional subsequent monitoring surveys were conducted during 2012 to 2020 for 0, 36, 102, 141, and 272 ktonnes of injected CO_2 (White et al. 2021). This was possible through a permanent array of buried geophones for surface recording, a permanent fiber-optic cable for DAS-based VSP recording, and dynamite shots for surface and VSP shooting. **Figure 17** shows the depth slices through the main amplitude anomaly in the upper Deadwood Formation. The footprint of the CO_2 plume is asymmetric, extending mainly northward from the injector. The Deadwood CO_2 plume amplitude grows with more CO_2 injection (102, 141, and 272 ktonnes). Minimum CO_2 thickness/saturation estimates for the main CO_2 plume zone in Perforation 2 are 4-10 m and 50%-100%. The CO_2 plume appears to be developing in a northward direction, likely as a result of a combination of factors, including the SSE regional dip, the NNW-SSE oriented flexure structure, and its impact on porosity/permeability fabric in the targeted formations (Roach and White 2018; White et al. 2021).

Figures 17-(e) through **-(h)** show seismic amplitude difference maps in the upper Deadwood zone for the different monitor surveys relative to the baseline survey. These 2D difference maps, overlaid on top of acoustic impedance, represent a proxy for the lateral extent of the CO_2 plume at the 2nd perforation. The main CO_2 plume is assumed to be in the high-permeability zone. White (2018) and White et al. (2021) noted the variability in the noise levels among different surveys. In particular, the noise level of

the monitor survey at 141 ktonnes was determined to be significant. White et al. (2021) indicated that the central anomaly is robust whereas the amplitude differences at distance from the wells are most likely noise and thus should be ignored for modelling purposes.

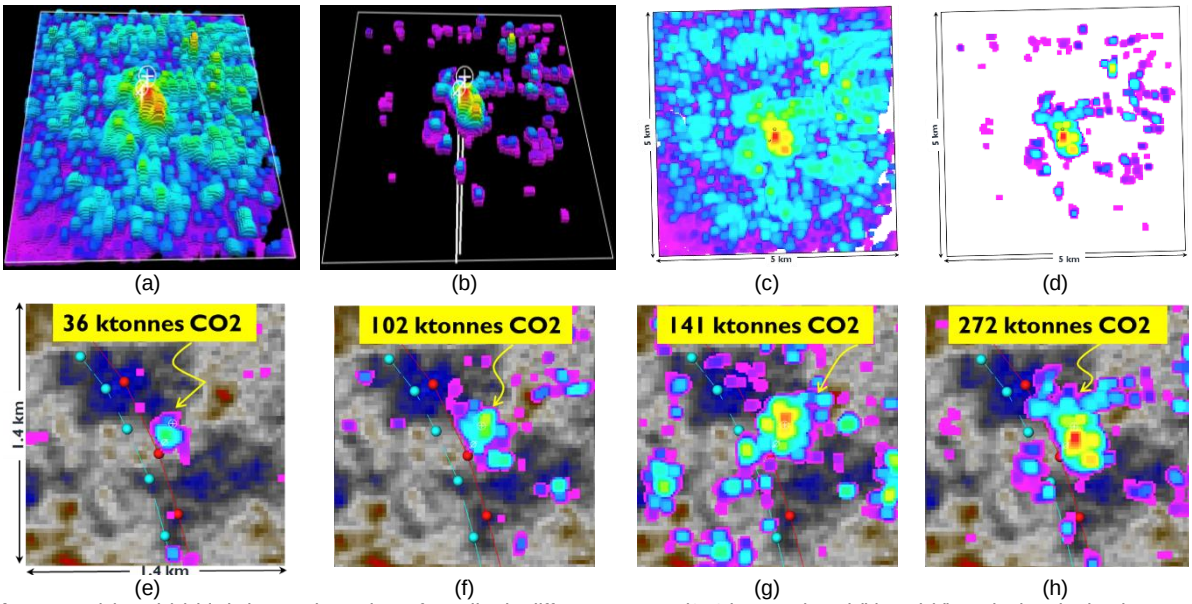

Figure 17: (a) and (c) bird view and top view of amplitude difference maps (272 ktonnes) and (b) and (d) exclusion the background noise with an arbitrary threshold to define the outline of CO_2 plume. The main plume outline seismic amplitude difference maps in the upper Deadwood zone for the different monitor surveys (e) 36 ktonnes, (f) 102 ktonnes, (e) 141 ktonnes, and (e) 272 ktonnes, relative to the baseline survey.

To exclude most of the background noise, an arbitrary threshold was applied to the amplitude difference maps. This allowed the definition of the main plume outline (**Figure 17-b** and **-d**). The outline of the amplitude anomalies is a proxy of a region where CO_2 saturation and thickness are sufficiently significant to be detected through seismic monitoring. Based on previous modelling experience, the minimum CO_2 saturations must be 10% with a note that seismic monitoring becomes less sensitive to saturation differences as the saturations increase (White et al. 2021). With more CO_2 being injected into Aquistore, the areas of increased amplitude likely correspond to an increase in CO_2 thickness and/or CO_2 saturation.

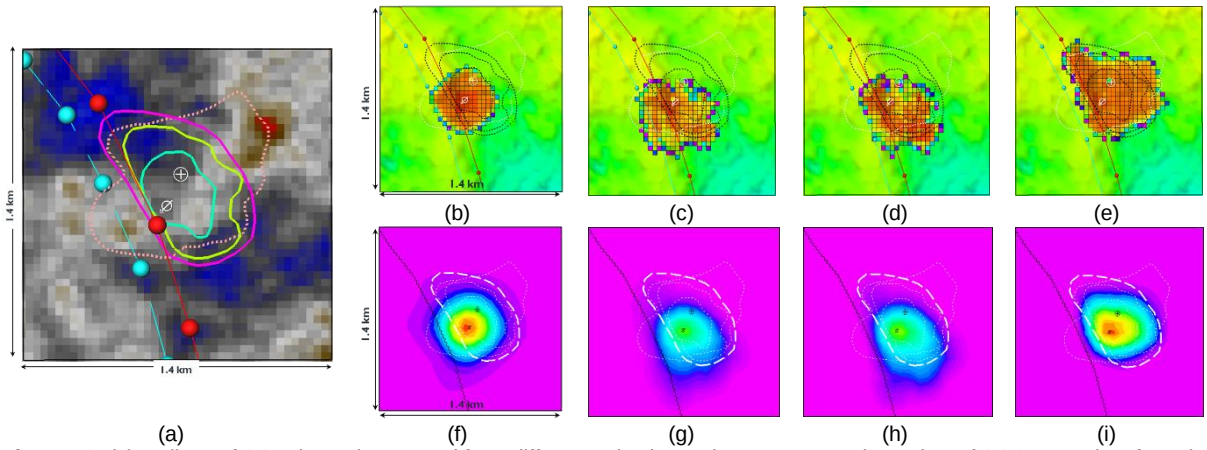

Figure 18: (a) outlines of CO_2 plume, interpreted from different seismic monitor surveys, and top-view of CO2 saturation, from the flow simulator, in the top layer of the Deadwood D formation, with respect to the outlines of CO_2 plume with the assumptions of (b) layer cake, (c) stochastic properties, (d) stochastic properties with flexure, (e) petrophysical properties constrained to acoustic impedance and honoring the presence of flexure, and (f) through (i) their equivalent saturation-thickness average maps for all layers.

Figures 18-(b) through -**(e)** show different realizations of simulated CO_2 saturation, from the flow simulator in the top layer of the Deadwood D formation, with respect to the outlines of CO_2 plume, interpreted from different seismic monitor surveys. **Figures 18-(f)** through **-(i)** show corresponding saturation-thickness average maps for all layers. The inclusion of heterogeneity, constraining the porosity and permeability to acoustic impedance, and the flexure as a permeability baffle, helped to match the outline of CO_2 plume from the flow simulator with the interpreted CO_2 plume from seismic monitor surveys.

Figure 19 shows the in-line slices from the surface 3D time-lapse RMS amplitude anomalies that pass through the CO_2 injection well. There are distinct time-lapse RMS anomalies within the reservoir intervals that were interpreted as zones of CO_2 saturation (White et al. 2019). The primary and secondary RMS amplitude anomalies are within the upper Deadwood and the lower Deadwood zones, respectively. The amplitude anomalies are beyond the background noise, and their strengths appear to grow in lateral extent with more quantities of CO_2 injected in each monitoring survey. The survey results agreed well with the PND log-based estimates of CO_2 saturation at the observation well within the Deadwood formation (White et al. 2019).

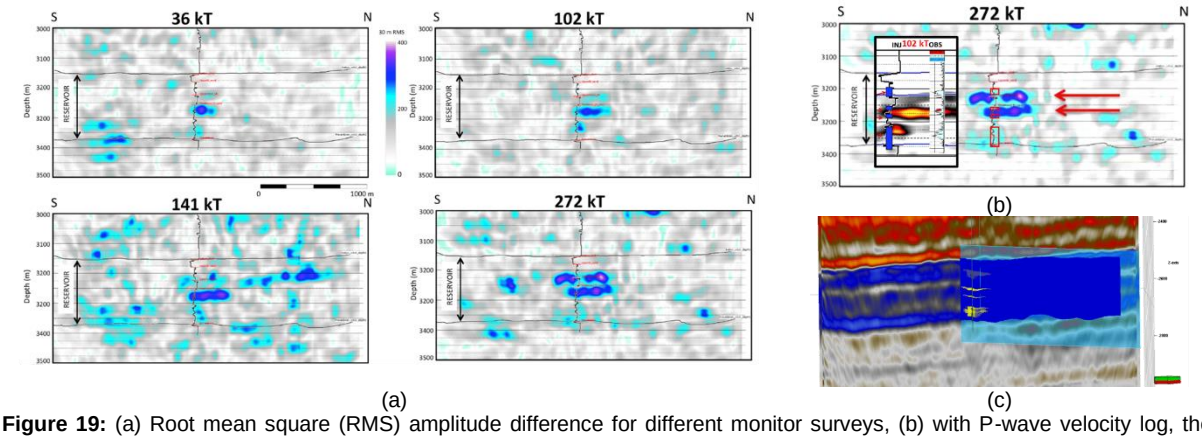

Figure 19: (a) Root mean square (RMS) amplitude difference for different monitor surveys, (b) with P-wave velocity log, the perforated zone locations for the injection well and interpreted pulse neutron log from the observation well superimposed (modified from White et al. 2018, 2019)

Figure 20 illustrates the downhole injection pressure from simulated data against the observed field data on a daily averaged basis for different realizations, namely with the layer cake assumption, with inclusion of stochastic petrophysical properties with and without the flexure (fault-like structure), and with stochastic petrophysical properties constrained to the acoustic impedance volume from seismic surveys. **Figure 20-(e)** shows the cumulative injected mass of CO_2 for all the realizations; all of them overlay the observed field data. The quality of the history match of the injection history are high for all realizations, but each realization results in different estimates of shape and extent of the CO_2 plume. This highlights the significance of including the knowledge of interpreted CO_2 plume outlines from seismic data to better constrain the simulated flow outcomes.

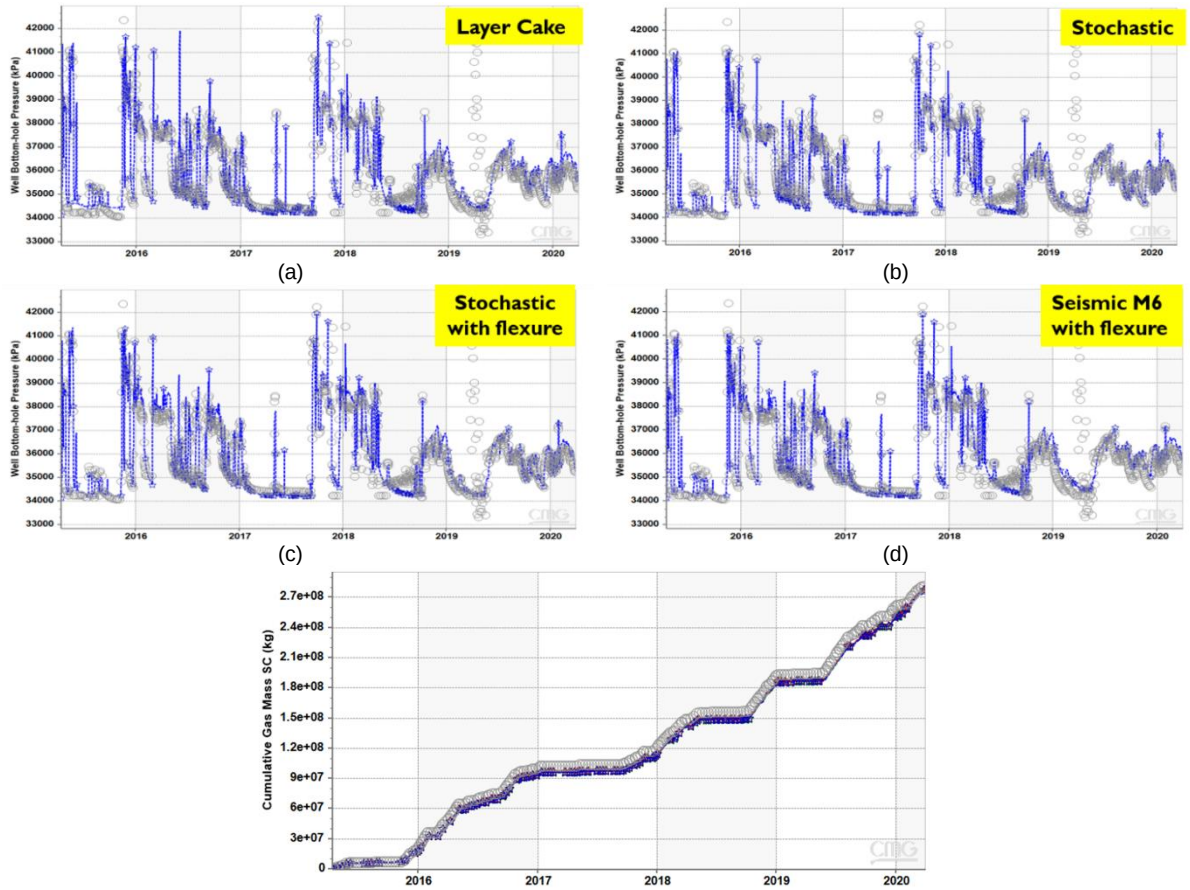

Figure 20: Downhole injection pressure from simulated data against the observed field data on a daily averaged basis for the realizations (a) with the layer cake assumption, (b) with inclusion of stochastic petrophysical properties, without and (c) with the flexure (fault-like structure), and (d) with stochastic petrophysical properties constrained to the acoustic impedance volume from seismic survey. (e) cumulative injected mass of CO_2 for all the realizations that all overlay the observed field data.

3.2 Build High-Resolution Sector Model to Initialize Flow Simulations

3.2.1 Generate and Rank Multiple Realizations of Static Geological Model

One of the advantages of the full geological modelling process is the possibility to assess uncertainties associated with seismic, geology, and flow data from the Aquistore injection site, and to visualize the spatial localization of uncertainty with respect to the developed CO_2 plume. We used stochastic modeling tools of Petrel (**Figure 21**) to obtain a set of realizations that takes into account the uncertainty of facies distribution (facies analysis and facies attribute probability), porosity distribution (data analysis, variograms, correlations to acoustic impedance), permeability distribution (cross plots with porosity constrained with seismic data, collocated co-kriging per facies), relative permeability (per facies), and location of the flexure (permeability baffle).

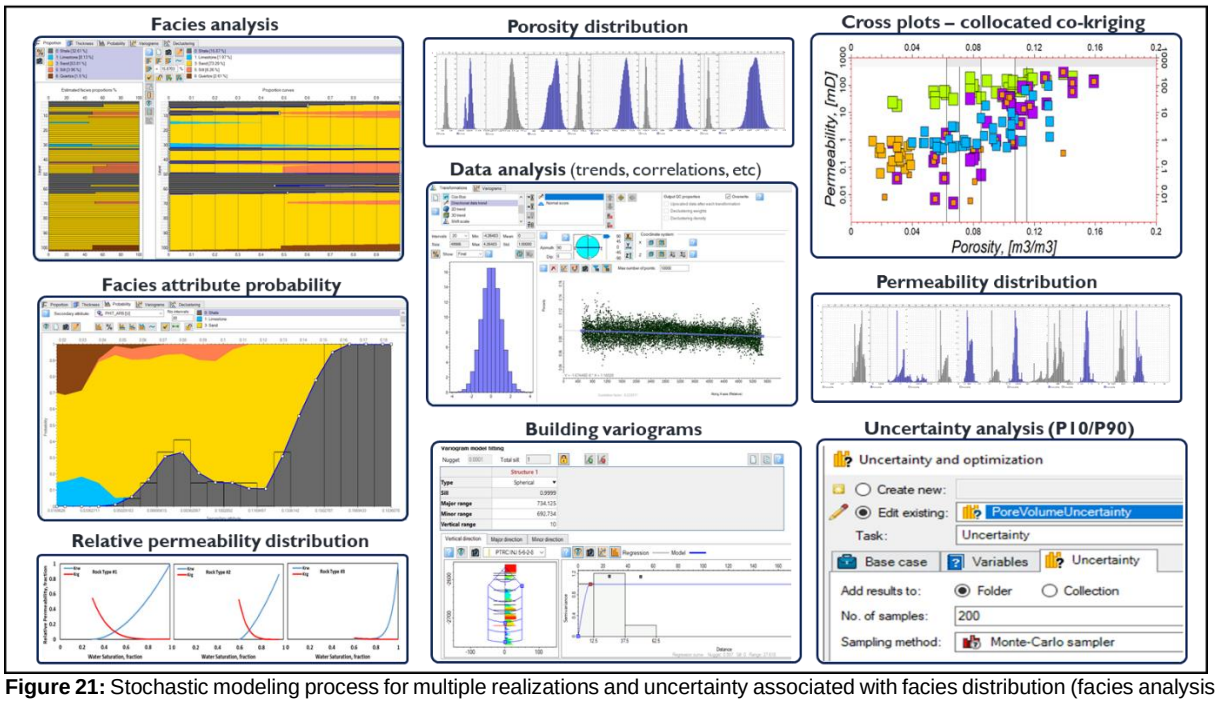

Figure 21: Stochastic modeling process for multiple realizations and uncertainty associated with facies distribution (facies analysis and facies attribute probability), porosity distribution (data analysis, variograms, correlations to acoustic impedance), permeability distribution (cross plots, collocated co-kriging per facies), relative permeability (per facies), and location of the flexure (permeability baffle)

The main uncertainty workflow, as shown in **Figure 22**, was based on pore volume calculation in sand bodies of the Aquistore injection site. We used Monte-Carlo sampler with Latin-hypercube sampling technique to generate 200 realizations and incorporate the uncertainties associated with vertical and horizontal heterogeneities from well logs, core data, and seismic surveys. The porosity and permeability distributions were generated at each realization using the Gaussian random function simulation method, constrained to acoustic impedance as a secondary variable (collocated co-kriging technique) with variograms (nugget, sill, range, anisotropy range, orientation) and collocated co-kriging coefficient as uncertain variables. We assigned relative permeabilities/thermal properties to appropriate facies/geological layers based on available laboratory studies from Aquistore.

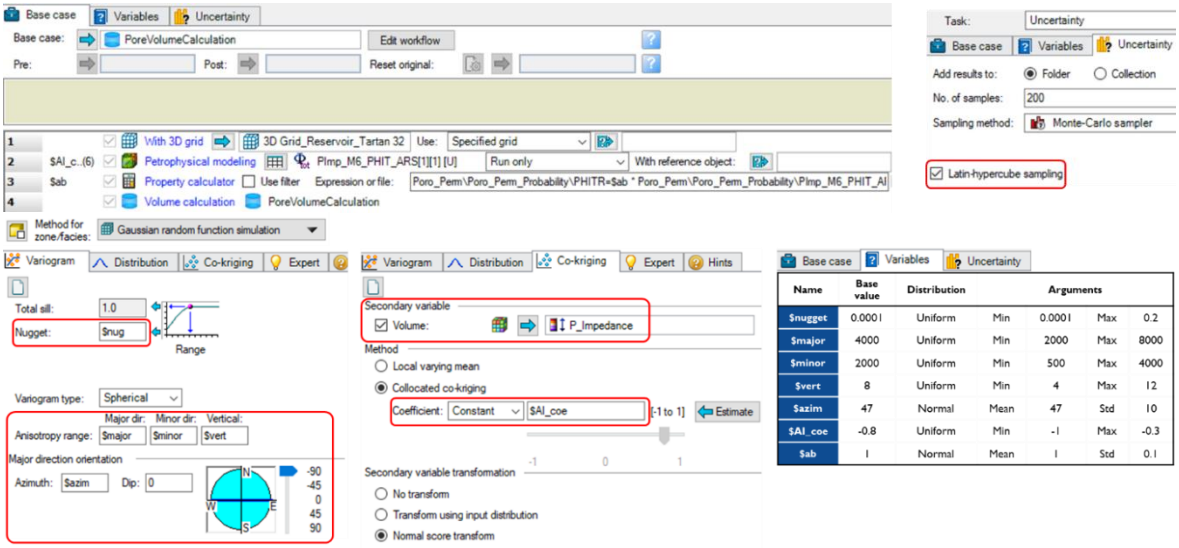

Figure 22: The uncertainty workflow to rank pore volume calculation in sand bodies of the Aquistore injection site.

Figure 23-(a) is a statistical comparison of the result of upscaling the well logs, and populating the porosity to the full geological model for one realization. An inspection of the porosity distribution and cumulative density functions indicates that the petrophysical modeling process could honor the spatial statistics of the measured well logs in the upscaled and populated properties in the model. The general assumption is that after upscaling, the log scale variations can be ignored and the emphasis in simulation would be on the match of the histogram of the upscaled cells with the full geological model. Once upscaled, it is no longer necessary to match the variability of raw logs because the variability and scale of well logs differ from the full geological model. In this way, the appropriate variability of the cell block scale is captured in the upscaled cells distribution.

We used the variability of cell block scale (upscaled from well logs) to model the full reservoir. **Figure 23-(a)** shows that the overall character of the distribution was preserved, as there is a good visual match of the vertical variability of the raw log and upscaled cells; the cumulative density functions overlay each other. **Figure 23-(b)** compares the spatial statistics of porosity distributed in many realizations (e.g. **Figure 23-(c)**). This indicates that while the spatial distributions of porosity in various realizations are different, they all honor original well log data and are statistically equivalent. This step is beneficial as we rely on limited hard data from only two wells (injection and observation wells) in the whole model of the Aquistore site.

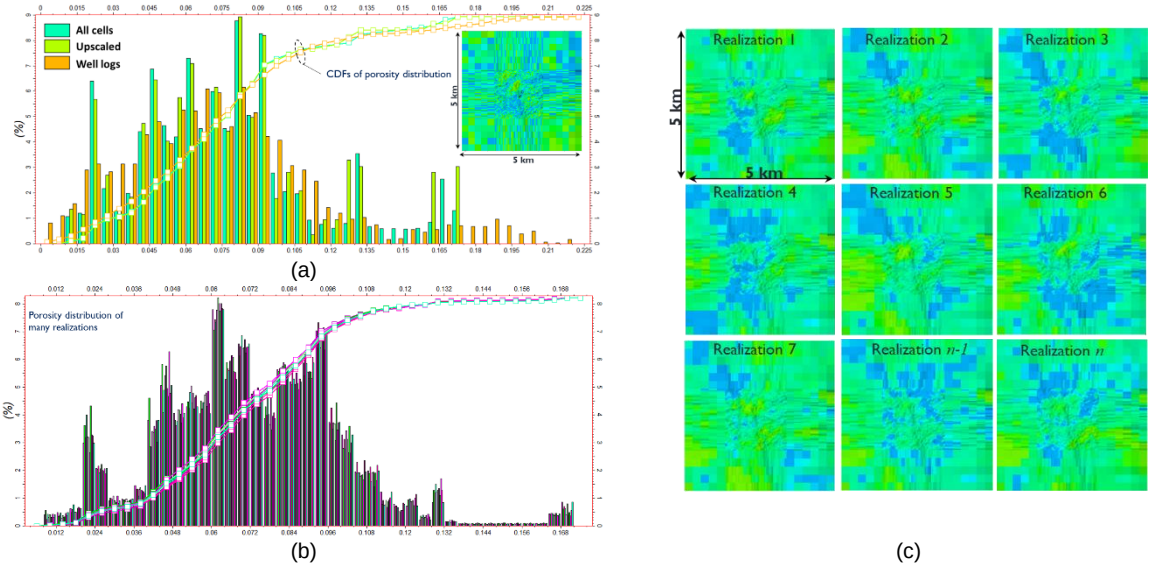

Figure 23: (a) Statistical comparison of well logs, upscaled, and all populated porosity to the full geological model for one realization, and (b) porosity distributed in many realizations as in (c).

We generated multiple realizations using the Monte-Carlo simulation and computed a final pore volume of sand bodies, as shown in **Figure 24**. With the use of the Monte-Carlo method, the possible random values of each parameter were modelled. Only sand bodies (as opposed to shales) are assumed to contribute to the capacity of CO_2 storage complex. We ranked the generated realizations of sector model with respect to the "static base" model and exported some of the realizations (e.g. P10, P50, P90) for further flow simulations. Based on the selected rank (e.g. P50), we can obtain the relevant parameters assigned in that realization and use its porosity/permeability distribution as the required input for the base case dynamic simulation in section 5. Here, different possible ranges of variation for each parameter are specified as well as the type of statistical distribution and values of its parameters.

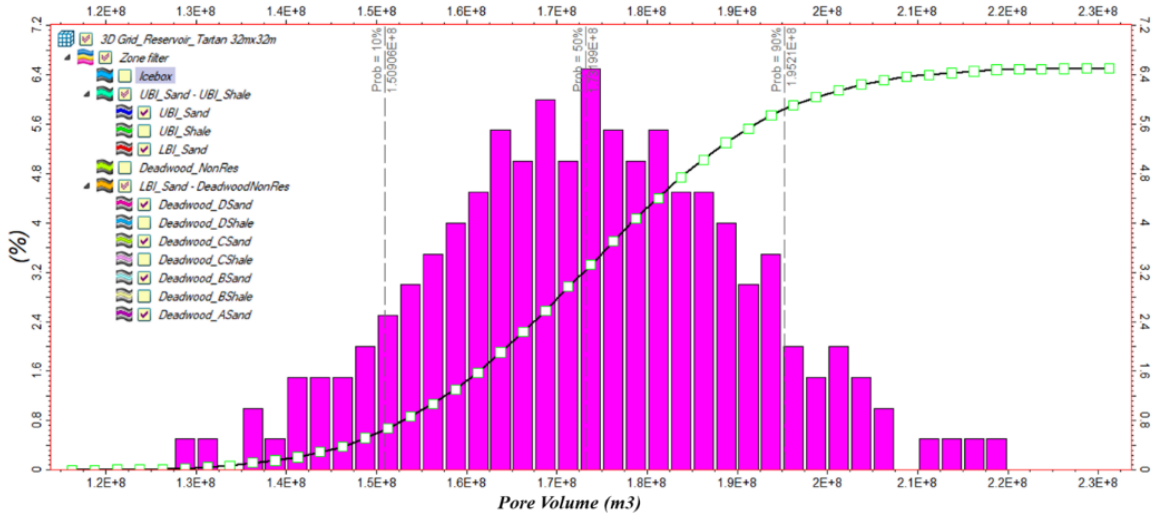

Figure 24: Generating multiple realizations using the Monte-Carlo simulation and ranking the computed pore volume of sand bodies

3.2.2 Impose the Initial and Boundary Conditions for the Sector Model

Based on the appraisal of most probable realizations of CO_2 plume extent and shape, we extracted a sector from the full geological model, and re-built it into a very fine scale geo-cellular model between the injection and observation wells (area of interest) with grid size of 4m x 4m; this step was meant to represent the near-wellbore geology and the developed CO_2 plume. We performed quality check and statistical comparisons of the generated high-resolution geological sector model with original petrophysical properties in the base model in terms of mean, standard deviations, histograms, and distribution (section 4.1).

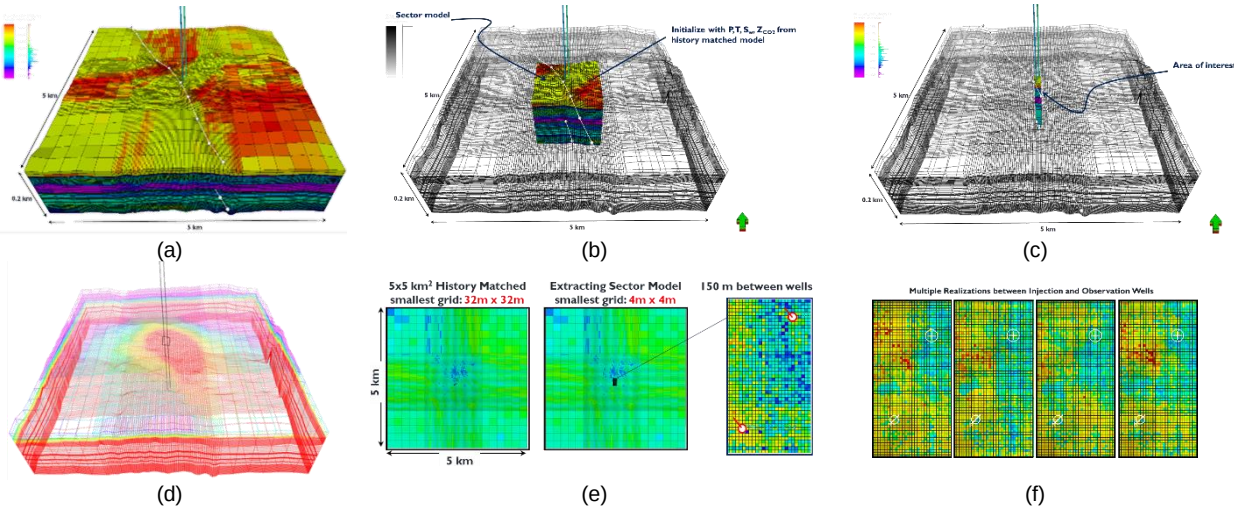

Figure 25: (a) full geological model, (b) taking initial and boundary conditions of history matched model for the sector model and (c) area of interest, (d) pore pressure over the full geological model, (e) top view of the refined cells in the area of interest between wells and (f) multiple realizations of porosity distribution for the high-resolution refined model.

The high-resolution model was first initialized based on pressure, temperature, water saturation, and global mole fractions of the last time step of the history matched model, i.e. April 1st, 2020 (**Figure 25**). During the dynamic base-case simulation, we noticed that imposing boundary conditions of no-flow or analytic aquifer at the exterior boundary of the sector model resulted in numerical instability and longer run time. We experienced similar problems when using the (last time step of history matched) properties of the exterior boundary of the area of interest to initialize the base case simulation study. This was

caused because the area of interest was affected by a developing CO_2 plume and, therefore, it seemed necessary to include those dynamic boundary conditions. After several modeling attempts, we concluded that the refined model should be used within the full coarse-grid geological model so that the properties at the boundary of the area of interest were directly taken from the last time step of the history-matched model as a whole. In other words, we had the refined model integrated into the full geological model with different cell sizes/resolutions. This respects the presence of a regional aquifer and its influence on the CO_2 plume; it significantly improved the run time and reduced the errors (e.g. material balance) in the dynamic simulations of the base case study.

Figure 25 indicates how we included the heterogeneity of the high-resolution sector model into the full geological model, while honoring the simulated history matched results to initialize the base case study.

4 Results and discussion

4.1 Base-Case Dynamic Simulation of the CO_2 Circulation Test

To suit the CO_2 circulation study, we modified the non-isothermal CMG-GEM simulation file for the area of interest. The high resolution flow model was initialized based on the history matched full-geological model from April 2015 to April 2020. To do so, we exported the last time step of the history matched CMG-GEM file – including water saturation, pressure, temperature, and global mole fractions of CO_2 and CH_4 (methane) – to the full geological model in Petrel using rescue format. The parameters from the full geological model were then assigned to the refined high-resolution model within Petrel, and then exported as Eclipse simulation keyword properties to a text editor. The Eclipse keywords were changed to the required keywords in CMG-GEM formats. The new CMG-GEM file was then updated to suit the CO_2 circulation study. The petrophysical properties of the base case were constrained to seismic data, as explained earlier.

One of the main assumptions in the base case feasibility study of CO_2 circulation is that the observation well (151 m away from the injection well) would act as a production well. Other assumptions in the base case simulation are summarized in **Table 3** for the injection and observation (i.e. producer) wells. Throughout the text, we interchangeably use both terms: observation well and producer.

Table 3: Assumptions in the base case simulation of CO_2 circulation test

Injection well	Observation well (i.e. producer)
Max downhole injection pressure 42.5 MPa (95% fracturing pressure)	Min downhole production pressure 33 MPa Max CO_2 production rate 300 rm3/day* (consistent with 0.11 m ID tubing)
CO_2 injection rate 600 rm3/day* (5-yrs avg. max injection rate)	Production through 2nd perforated interval only (highest permeability)
Downhole injection temperature 70 ^oC (5-yrs avg. temperature of active injection)	No fracturing/no salt precipitation around production well
Injection through all 4 perforated intervals	
Injectivity is governed by: - formation properties (porosity, permeability, facies) - formation thickness - fluid distribution (saturation, relative permeability)	
Injection period of 9 months continuous CO_2 circulation	

* rm3/d: volume (m3) is reported at reservoir conditions.

Figure 26-(a) shows the gas saturation in a block reservoir near production well in Deadwood D – 2nd perforation. Basic simulations on different realizations of the CO_2 plume suggests that the layer cake assumption leads to an overestimation of gas saturation around the observation well. Initial gas saturation from other realizations are reasonably comparable. Gas saturation increases in all cases after a few days. The increase in gas saturation due to CO_2 circulation is highest for the realization that was calibrated to the seismic data and assumed the presence of a flexure. From this exercise, one may conclude that heterogeneity, anisotropy, and inclusion of fracture could negatively affect the performance of CO_2 circulation.

Figure 26-(b) shows the gas/water ratio at the production well. It seems that the layer cake assumption leads to better gas-to-water ratio at the production well. Gas-to-water ratio decreases and then increases with more CO_2 injection. The ratios at standard conditions are significantly larger due to CO_2 compressibility and water incompressibility. Moreover, fluid injection in the base case study was through 4 perforated intervals at the injector, while fluid production was only allowed from the 2nd perforated interval of the producer (**Table 3**). These observations suggest that we need to examine and optimize the injection/production well constraints to manage the CO_2/brine production.

Figure 26-(c) is the CO_2 mass rate at injection and production wells. Note that the amount of injected CO_2 is almost identical in all realizations so that the production rate of brine and CO_2 could be compared in each simulation. In all cases, the mass of injected CO_2 is higher than the mass of produced CO_2 which means a portion of CO_2 is permanently trapped in the formations. In addition, there is a need for make up fluid (i.e. additional captured CO_2) in each cycle to maintain the same level of injection. Mass of produced CO_2 shows an increasing trend for the realizations of stochastic properties constrained to seismic data, with the assumption of the flexure. These basic observations convey the message that CO_2 circulation tests could be executed while permanently storing CO_2 underground. Because of the presence of 4 perforated intervals with inter-bedded shale layers, the perforation/completion design of the production well again is a subject for optimization (e.g. voidage replacement, gravity override/water coning/buoyancy effects).

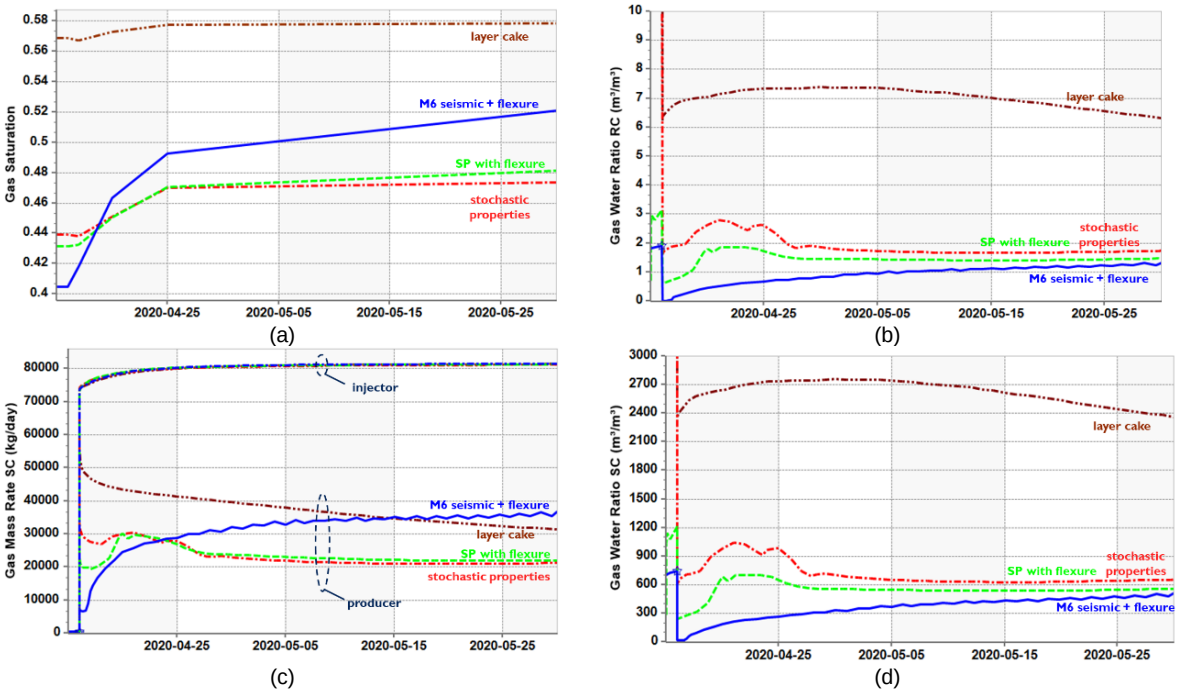

Figure 26: (a) gas saturation in a block reservoir near production well – Deadwood D, (b) gas/water ratio at production well at reservoir and (d) surface conditions, and (c) CO_2 mass rate at injection & production wells.

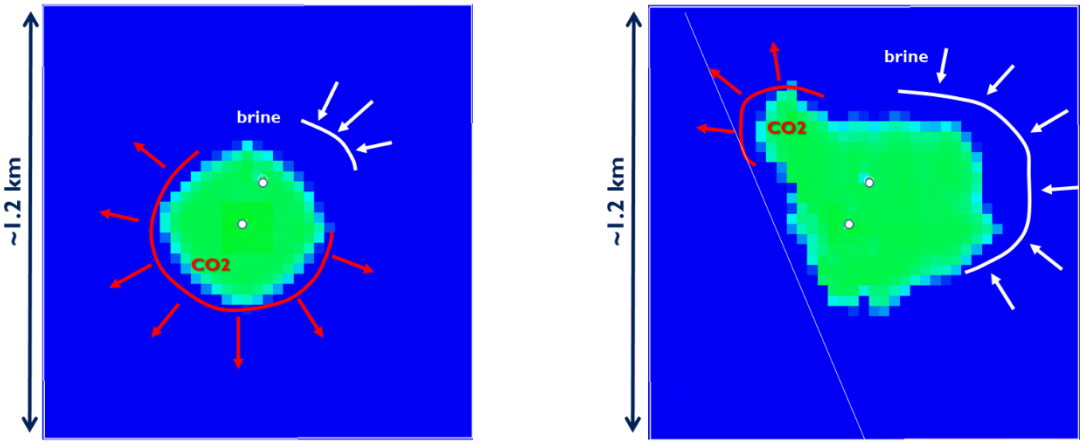

(a) (b)

Figure 27: Top view of water saturation in the Deadwood D formation with (a) layer cake assumption, and (b) calibrated flow simulation to M6 monitor seismic survey with inclusion of flexure.

Figure 27 provides the top view of water saturation near the injection and production wells during the course of CO_2 circulation. Early simulation results with the base assumptions suggest there is a possibility of brine entering the CO_2 plume zone and the observation well from an encroaching aquifer. Note how the inclusion of heterogeneity and flexure in the Deadwood Formation changes the way CO_2 and brine move within the reservoir during CO_2 circulation tests in **Figure 27-(b)**. This highlights the significance of examining and optimization of injection/production well constraints to determine the possible existence of any working conditions for both wells (e.g. rates and pressures) to minimize brine entering the CO_2 plume/rich zones.

4.2 Dynamic Uncertainty Analysis of the CO_2 Circulation Test

The dynamic uncertainty of CO_2 injection arises from the degree of confidence in determining the extent and shape of the CO_2 plume, the distribution of brine and CO_2 saturations within the plume, difficulty in determining the heterogeneity and anisotropy of the petrophysical properties and geological structures (e.g. shale baffles, flexure), and dynamic alterations in reservoir behaviour (e.g. reduced permeability and enhanced imbibition zone due, for instance, to salt precipitation or increase in permeability/injectivity due to localized thermal fracturing). Other sources of uncertainty are the presence and quality of the regional aquifer, its ability in mobilizing the brine into the CO_2-rich zones and/or the low pressure sinks (e.g. production well), and (previously experienced) brine back-flow into the wellbore during shut-in periods in intermittent injection (Talman et al. 2020). To assess the impacts of such uncertain variables on the performance of the CO_2 circulation test, we used the base case simulation of the area of interest; this was extracted from the history-matched model. As a result, initial and boundary conditions for the sector model were adopted from a unique parent history-matched model and were identical in all uncertain case studies. The latter step was aimed to show that the incremental changes in key performance metrics of CO_2 circulation tests (e.g. cumulative production, water-to-brine ratio, among others) were truly associated with the limits of selected uncertain variables, rather than initial/boundary conditions of the base model.

In the base model, we assumed that CO_2 injection occurs through the 4 perforated intervals at a rate of 600 rm3/d and maximum BHP of 42.5 MPa (95% of fracking pressure). The producer was allowed to operate through only the 2nd perforated interval (i.e. highest permeability zone) at a minimum BHP of 33 MPa with a 300 rm3/d constraint on production rate.

Table 4 lists the uncertain variables, their base values, and variability limits. Operating parameters that could control the CO_2 circulation performance include the injection and production rates/pressures, the design of the wells, especially with respect to the completion/perforations. This is because currently there are four perforated intervals in the injection well and it is essential to manage the multi-horizon

CO_2/brine flow displacement within the CO_2 plume. Through proper completion/perforation design, one might manage the common issues in immiscible/miscible floods such as gravity override due to buoyancy effects, water coning, and changes in flow regimes, among others. One of the reasons to examine the injection/production well constraints was to estimate the possible existence of any working conditions of the injection/production wells (e.g. rates and pressures) to manage brine entering the CO_2-rich zones within the plume and near the production well. These values should be optimized in a comprehensive FEED study prior to conducting any pilot test at the Aquistore site. This is once more important because it can control the co-production of CO_2 and brine volumes at the production well (downhole and surface) so that proper surface facility equipment could be designed in order to handle/manage any initial brine kick during the CO_2 circulation test.

Table 4: uncertain variables, their base values, and variability limits for CO_2 circulation study

Uncertain variables	Base values	Variability limits
Injection rate at the injector	600 rm3/d	100 to 900 rm3/d*
Downhole pressure at the producer	33 MPa	23 to 39 MPa
Production rate at the producer	300 rm3/d	100 to 900 rm3/d*
Completion configurations at the injector	all 4 perforated intervals	all 4 perforated vs. 2nd interval only
Completion configuration at the producer	2nd perforated interval	all 4 perforated intervals individual interval only (1st/2nd/3rd/4th only) only one layer of 2nd interval (1st to 6th layer)
Fracturing/slat precipitation at the producer (S)	0 (=intact formation)	-2 (=fractured); 0 (=intact); +2 (=slight salt); +10 (=moderate salt)
Inclusion of localized perm. heterogeneity	Realization 0	8 stochastic realization
Adoption of post-workover injectivity gain	1x (=intact formation)	10-100x enhanced permeability zone

* rm3/d: volume (m3) is reported at reservoir conditions

In the uncertainty analysis, we did not look into optimizing the location of the production well; we simply assumed the existing observation well could act as a producer. Locating the production well within the CO_2 plume is of interest. The developed model can be used to determine the location of a new producer or an additional brine well for brine disposal or to manage reservoir pressure in future studies.

To compare the operability and efficiency of the CO_2 circulation test, we looked at different performance indicators including:

- rates (CO_2 mass injection, CO_2 mass production, brine production);
- cumulatives (injected CO_2 mass, produced CO_2 mass, produced brine, permanently stored CO_2);
- pressures (injection pressure, production pressure, well-double pressure drop within CO_2 plume); and
- others (gas-to-water ratio, dry-out time, brine inflow from regional aquifer).

The dry-out time was the time that CO_2 circulation between the injector and producer will reach close to steady-state operation (Hau et al. 2021). Note that the CO_2 circulation was assumed to operate at pressure ranges below fracturing pressure, at/below CO_2 plume pressure, and above/at/below pressure of the regional aquifer. For brevity, we only included the figures for the impact of injection rate. Figures for other uncertain variables are included as an appendix. It is worth mentioning that CMG-GEM simulator requires volumetric input of the CO_2 injection rate; but we converted the output and reported the CO_2 rates on a mass basis in order to compare the results.

Figure 28-(a) shows that higher CO_2 injection rate takes a slightly larger time to stabilize at the injection well. The simulation results during 9 months of CO_2 circulation test suggest that the saline formation has the capacity to accept continuous high rates of CO_2 injection. The production rate at the producer seems

to be responding to a variable CO_2 injection rate (**Figure 28-b**). Higher CO_2 injection rates results in higher CO_2 production rates, and larger time for the production rate to stabilize at the producer. If one defines the ratio of CO_2 production mass rate to CO_2 injection mass rate, as a performance indicator, this mass rate ratio decreases from 49% to 24% when increasing the injection rate from 100 to 900 rm3/d. This indicates more CO_2 is lost or permanently trapped at higher injection rate during the CO_2 circulation test. Of interest, the brine production rate also slightly increases with higher injection rate (**Figure 28-c**).

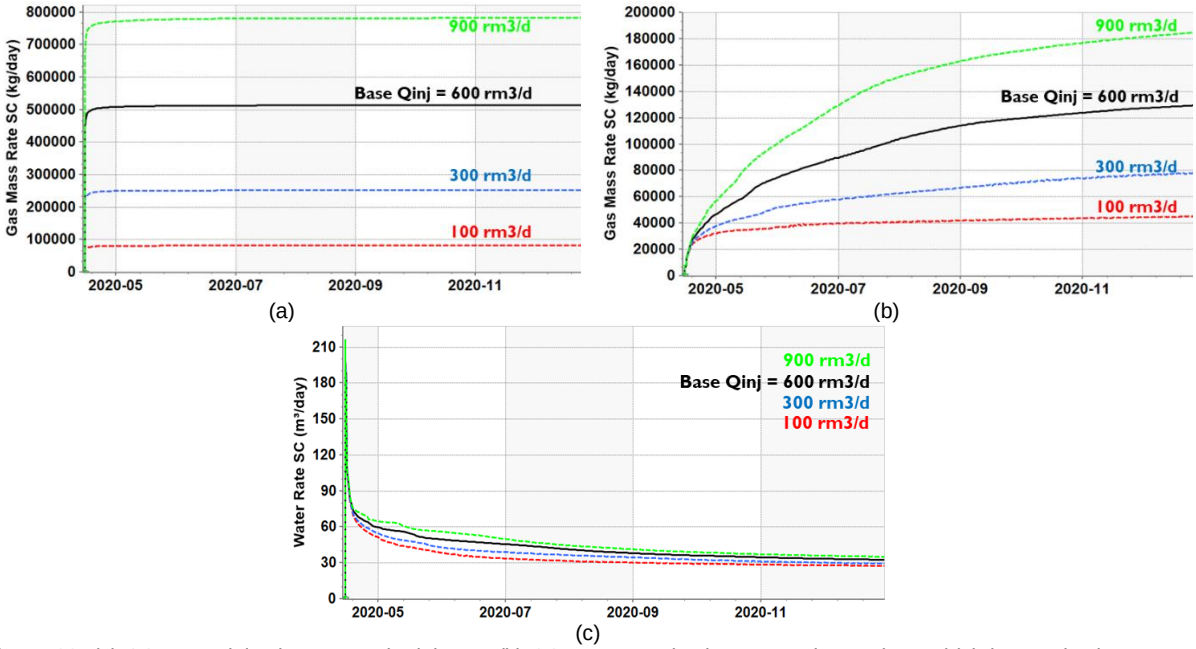

Figure 28: (a) CO_2 mass injection rate at the injector, (b) CO_2 mass production rate at the producer, (c) brine production rate at the producer; note that the operator should be prepared to manage initial brine production and continue with the CO_2 circulation test.

All of the simulations suggest that CO_2 circulation might initially result in production of a large volume of brine at the producer, and a proper surface facility should be available to mange the initial kick from brine production and continue the test. The brine production will abruptly decrease beyond this point. Note that this initial brine production is expected from the simulation work, and it should not result in shutting the production well early during the proposed pilot test (i.e. immature pilot test); the CO_2 circulation test should not be interpreted as unsuccessful because of an early brine kick.

The set of plots in **Figure 29** are performance indicators based on the cumulative mass, rather than rates. The slope of the lines shown in **Figure 29-(a)** are almost constant and indicate the saline aquifer has sufficient capacity and injectivity to accept the increase in CO_2 injection without any significant disruption. Higher injection rate resulted in an increase of cumulative mass of produced CO_2 from the production well (**Figure 29-b**). Defining the ratio of cumulative injected to produced CO_2 on a mass basis, the cumulative mass ratio decreases from 50% to 18% due to an increase in injection rate from 100 to 900 rm3/d. This suggests a larger amount of CO_2 is being lost/trapped within the saline formation at higher injection rates, which might be due to multi-horizon CO_2 injection/production. Bear in mind that CO_2 is injected through four perforated intervals at the injector, but it is only produced from the second perforated interval at the producer.

We can determine the trapped/stored CO_2 as the difference between the cumulative mass of injected and produced CO_2 during the circulation test, as depicted in **Figure 29-(d)**. Defining the mass ratio of stored CO_2 to cumulative injected CO_2, another performance indicator, the increase in injection rate from 100 to 900 rm3/d results in an increase of the stored mass ratio from 50% to 82%. It is also important to know the fate of CO_2 lost during the CO_2 circulation test, and whether it remains safely contained in

the formation or not (e.g. dissolution in the aqueous phase, formation of solid carbonates). The higher CO_2 injection rate also increases the cumulative brine production from the saline formation (**Figure 29-c**).

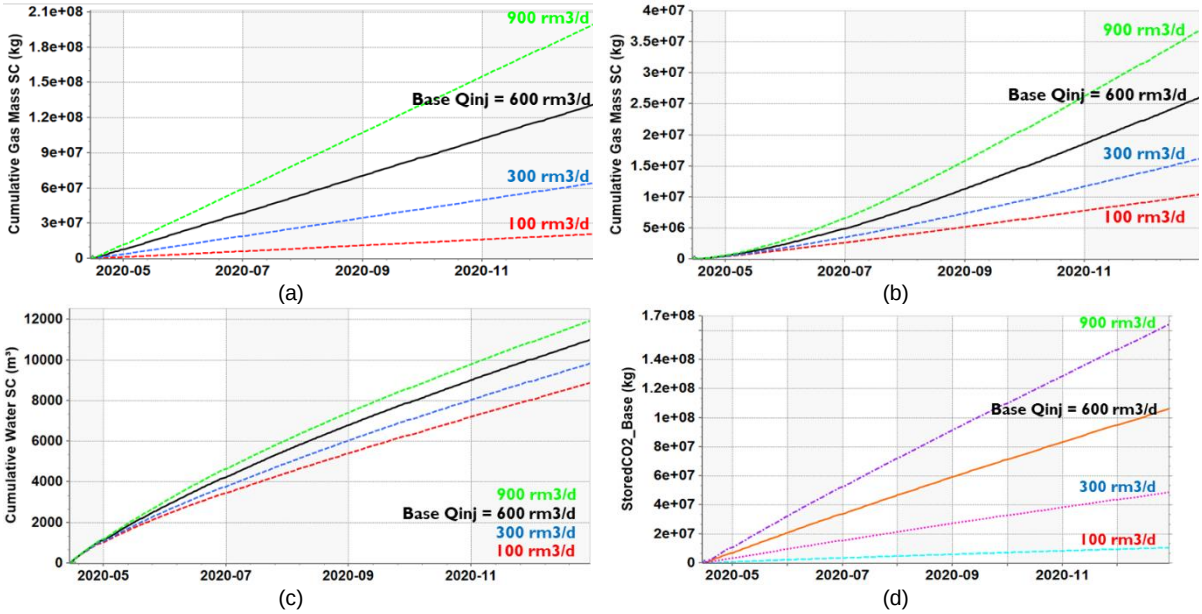

Figure 29: (a) cumulative injected CO_2, (b) cumulative produced CO2, (c) cumulative produced brine, (d) cumulative stored CO_2 in the saline formation (CO_2 loss during CO_2 circulation test).

Other metrics include the gas-to-water ratio of the production well at reservoir conditions as depicted in **Figure 30-(a)**. Because simulated results indicate an initial brine kick in the production well, the gas-to-water ratio decreases immediately to values close to zero. Shortly after the initial brine production, the gas-to-water ratio increases during the CO_2 circulation test. Higher injection rate results in higher gas-to-water ratio, which is of significance to avoid liquid loading in the production well. By liquid loading, we mean the accumulation of liquid brine in the production well due to insufficient CO_2 rate and low gas-to-water ratio.

Figure 30-(b) illustrates the pressure related results. It is evident that injecting CO_2 at higher rates requires higher injection pressure. For the base case, we have a maximum bottomhole pressure constraint of 42.5 MPa (95% of fracking pressure) at the injector, and a minimum bottomhole pressure of 33 MPa at the producer. It appears the injection pressure reaches close to steady-state conditions in all cases. The time for the pressure to reach a steady-state condition depends on the extent and pressure of the CO_2 plume. In this case, the initial pressure of formation is 34.2 MPa and the average CO_2 plume pressure is estimated to be initially 35-36 MPa (prior to the CO_2 circulation test). Deviation of injection pressure from the pressure within the CO_2 plume seems to control how fast the pressure (injector and plume) reaches steady-state conditions.

We can define the pressure difference between the injector and producer within the CO_2 plume as an additional performance indicator. Higher CO_2 injection rate results in higher pressure drop between wells within the CO_2 plume. **Figure 30-(c)** compares the relationship of injection mass rate, production mass rate, and the mass rate difference between the injector and producer with pressure drop within the CO_2 plume. Although this is not a simple 1 D single phase flow or immiscible displacement analytical model, when the system stabilizes, it is interesting to note that there is a linear trend between these variables; one might think it follows a form of Darcy's equation. This may be due to the fact that the CO_2 plume within the injector and observation wells in Aquistore has been fairly developed and CO_2 seems to be the dominant mobile phase.

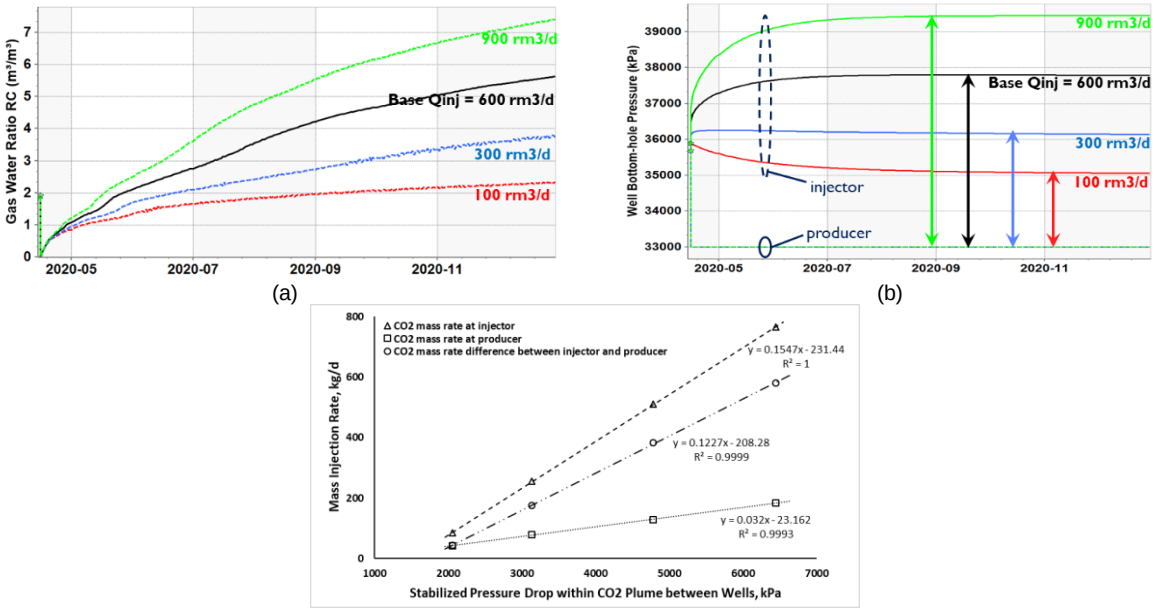

Figure 30: (a) gas water ration at the production well in downhole condition, (b) well bottomhole pressure of the injector, the producer and the difference in downhole pressure between the two wells within the CO_2 plume, (c) the relationship among injection rate and pressures.

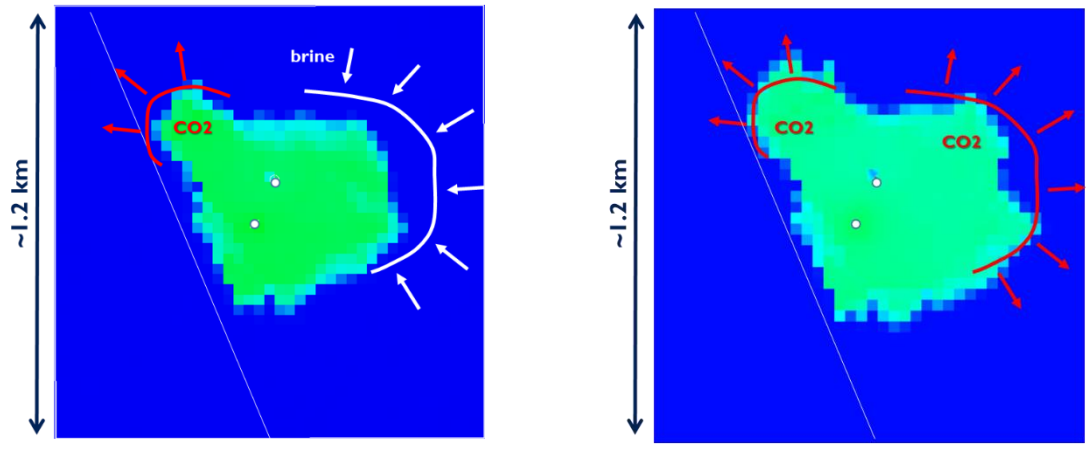

Figure 31: Top view of water saturation at the Deadwood D formation – top layer with calibrated flow simulation to M6 monitor seismic survey with inclusion of flexure (a) injection rate of 300 rm3/day, and (b) injection rate of 900 rm3/day.

Figure 31 provides the top view of water saturation near the injection and production wells during the course of CO_2 circulation. **Figure 31-(a)** shows that with an injection rate of 300 rm3/d, the CO_2 plume extends in NNE direction alongside the flexure structure (i.e. permeability baffle), but brine from the regional aquifer would push the CO_2 plume toward the production well (brine encroachment). **Figure 31-(b)** is also the top view of water saturation near the injection and production wells, but the injector operates at a higher injection rate of 900 rm3/d. It appears that the injection rate, and as a requirement, the injection/plume pressure, are sufficiently large to extend the CO_2 plume in all directions, and additionally, to prevent or minimize the brine encroachment. These basic simulations highlight the importance of examining and optimization of injection/production well constraints to determine the possible existence of any working conditions for both wells (e.g. rates and pressures) to minimize brine entering CO_2 plume/rich zones.

Table 5 provides the summary of uncertainty analysis and changes in the main performance metrics, as determined at the end of the simulated CO_2 circulation test. We can rearrange **Table 5** as in **Table 6** by tracking the changes of simulated results with the base case assumptions in each column. For instance, the relative change in cumulative injected CO_2 for each case can be defined as the difference between cumulative injected CO_2 of that specific case with the base case, divided by the cumulative injected CO_2 of the base case; we express it in percentage. In **Table 6**, red color represents an impairment/downgrade and green color represent an improvement/upgrade with respect to the performance of CO_2 circulation.

Numerous shades of green color suggest that it is possible to optimize the operating conditions to improve the performance of the successful circulation test. The operating parameters include injection rate, production rate, bottomhole pressures, completion designs and workover in injection/production wells, among others. Looking into different realizations of localized and post-workover permeability, it seems heterogeneity has a positive impact on permanent trapping of CO_2 in saline formations. The post-workover changes, including 10-100x increase in injectivity, could significantly change CO_2 circulation outcomes and result in a ~300% increase in CO_2 production and ~85% improvement in cumulative gas-to-water ratio. This potentially minimizes the issues with liquid loading and significant brine production.

Table 5: Simulation results at the end of CO_2 circulation test during the uncertainty analysis

All simulated cases		Cumulative injected CO_2 (kg)	Cumulative produced CO_2 (kg)	Cumulative produced water (Sm3)	Stored CO_2 (kg)	Injector BHP (kPa)	Producer BHP (kPa)	Stabilized pressure drop (kPa)	Cumulative gas-to-water (tonne/Sm3)
Base case assumptions	See **Table 4**	132254000	26125720	11003	106128280	37785	33000	4785	2
Injection rate (rm3/d)	100	21020546	10431332	8874	10589214	35056	33000	2056	1
	300	64882260	16228574	9839	48653686	36135	33000	3135	2
	900	201243504	36977836	11939	164265668	39449	33000	6449	3
Production rate (rm3/d)	100	132510704	16591232	7169	115919472	38143	35382	2761	2
	300	132254000	26125720	11003	106128280	37785	33000	4785	2
Producer BHP (MPa)	23	130431720	70009912	47421	60421808	36483	23000	13483	1
	27	131158184	55613692	30897	75544492	36962	27000	9962	2
	30	131704320	42155728	20199	89548592	37351	30000	7351	2
	36	132808376	7539942	2549	125268435	38286	36000	2286	3
	39	132995360	374	0	132994986	38528	39000	-472	1
Producer well skin (fracturing/plugging/salt precipitation)	-2	131992648	34129592	15225	97863056	37571	33000	4571	2
	+2	132407384	21222042	8678	111185342	37916	33000	4916	2
	+10	132671280	12267743	4740	120403537	38163	33000	5163	3
Completion design of injector	2nd perforated interval	126206552	66265540	6584	59941012	42500	33000	9500	10
Completion design of producer	All perforated intervals	130721248	83881656	24209	46839592	36294	33000	3294	3
	1st perforated interval	131991728	32370412	6437	99621316	37668	33000	4668	5
	3rd perforated interval	132767280	7689367	5732	125077914	38282	33000	5282	1
	4th perforated interval	132035448	44221804	7891	87813644	37319	33000	4319	6
	Layer 1 of 2nd perforated interval	132971976	1057112	98	131914864	38503	33000	5503	11
	Layer 2 of 2nd perforated interval	132988584	307108	48	132681476	38520	33000	5520	6
	Layer 3 of 2nd perforated interval	132990256	231523	41	132758733	38521	33000	5521	6
	Layer 4 of 2nd perforated interval	132894392	4004253	1370	128890139	38407	33000	5407	3
	Layer 5 of 2nd perforated interval	132315792	24215636	10041	108100156	37834	33000	4834	2
	Layer 6 of 2nd perforated interval	132991248	73899	149	132917349	38524	33000	5524	0
Different realizations of localized and post-workover permeability heterogeneity	Realization 1	133653048	16227430	11835	117425618	39502	33000	6502	1
	Realization 2	133327224	19066884	15266	114260340	38886	33000	5886	1
	Realization 3	133394872	17283240	16702	116111632	38829	33000	5829	1
	Realization 4	132937096	22641756	14267	110295340	38473	33000	5473	2
	Realization 5	133249992	15930492	11370	117319500	38683	33000	5683	1
	Realization 6	132973048	19773008	13874	113200040	38473	33000	5473	1
	Realization 7	133204064	15858060	13419	117346004	38554	33000	5554	1
	Realization 8	133473752	12769813	12453	120703939	38919	33000	5919	1
	Post-workover permeability	129086560	101657248	23439	27429312	35064	34428	635	4

Table 6: Quick overview of uncertainty assessment with respect to the base case assumptions

All simulated cases		Change in cumulative injected CO_2 (%)	Change in cumulative produced CO_2 (%)	Change in cumulative produced water (%)	Change in stored CO_2 (%)	Change in injector BHP (%)	Change in stabilized pressure drop (%)	Change in cumulative water-to-gas ratio (%)
Base case assumptions	See **Table 4**	0	0	0	0	0	0	0
Injection rate (rm3/d)	100	-84	-60	-19	-90	-7	-57	-50
	300	-51	-38	-11	-54	-4	-34	-31
	900	52	42	9	55	4	35	30
Production rate (rm3/d)	100	0	-36	-35	9	1	-42	-3
	300	0	0	0	0	0	0	0
Producer BHP (MPa)	23	-1	168	331	-43	-3	182	-38
	27	-1	113	181	-29	-2	108	-24
	30	0	61	84	-16	-1	54	-12
	36	0	-71	-77	18	1	-52	25
	39	1	-100	-100	25	2	-110	-42
Producer well skin (fracturing/plugging/salt precipitation)	-2	0	31	38	-8	-1	-4	-6
	+2	0	-19	-21	5	0	3	3
	+10	0	-53	-57	13	1	8	9
Completion design of injector	2nd perforated interval	-5	154	-40	-44	12	99	324
Completion design of producer	All perforated intervals	-1	221	120	-56	-4	-31	46
	1st perforated interval	0	24	-42	-6	0	-2	112
	3rd perforated interval	0	-71	-48	18	1	10	-43
	4th perforated interval	0	69	-28	-17	-1	-10	136
	Layer 1 of 2nd perforated interval	1	-96	-99	24	2	15	353
	Layer 2 of 2nd perforated interval	1	-99	-100	25	2	15	172
	Layer 3 of 2nd perforated interval	1	-99	-100	25	2	15	141
	Layer 4 of 2nd perforated interval	0	-85	-88	21	2	13	23
	Layer 5 of 2nd perforated interval	0	-7	-9	2	0	1	2
	Layer 6 of 2nd perforated interval	1	-100	-99	25	2	15	-79
Different realizations of localized and post-workover permeability heterogeneity	Realization 1	1	-38	8	11	5	36	-42
	Realization 2	1	-27	39	8	3	23	-47
	Realization 3	1	-34	52	9	3	22	-56
	Realization 4	1	-13	30	4	2	14	-33
	Realization 5	1	-39	3	11	2	19	-41
	Realization 6	1	-24	26	7	2	14	-40
	Realization 7	1	-39	22	11	2	16	-50
	Realization 8	1	-51	13	14	3	24	-57
	Post-workover permeability	-2	289	113	-74	-7	-87	83

Tornado plots in **Figure 32** provide a quick look at the results of the uncertainty analysis within the operational limits that were defined for the CO_2 circulation test. Apart from the obvious impact of injection rate, the completion design of the injector and post-workover changes significantly affect the cumulative injected CO_2 (**Figure 32-a**). Cumulative produced CO_2 is more a function of completion design of the producer, post-workover changes and bottomhole pressure of the producer (**Figure 32-b**). The reason that injector constraints are ranked lower is because a developed CO_2 plume can act itself as a source of CO_2 in early stages, and significantly contribute to CO_2 production at the producer.

The bottomhole pressure at the producer seems a controlling factor to manage the brine production (**Figure 32-c**). When the producer operates at lower bottomhole pressure than the pressures of the CO_2 plume and the aquifer, the brine from the regional aquifer will eventually enter the production well. To minimize the brine production from the aquifer, the CO_2 plume pressure should be maintained sufficiently higher than the pressure in the regional aquifer. This requires a balance of production rate/pressure at the producer and injection pressure/rate at the injector. The completion designs of injector, and in particular the producer, also control the total fluid production, and consequently, the cumulative brine production. The completion design should be optimized to assure that CO_2 can be produced at sufficiently high rates to prevent liquid loading in the production well.

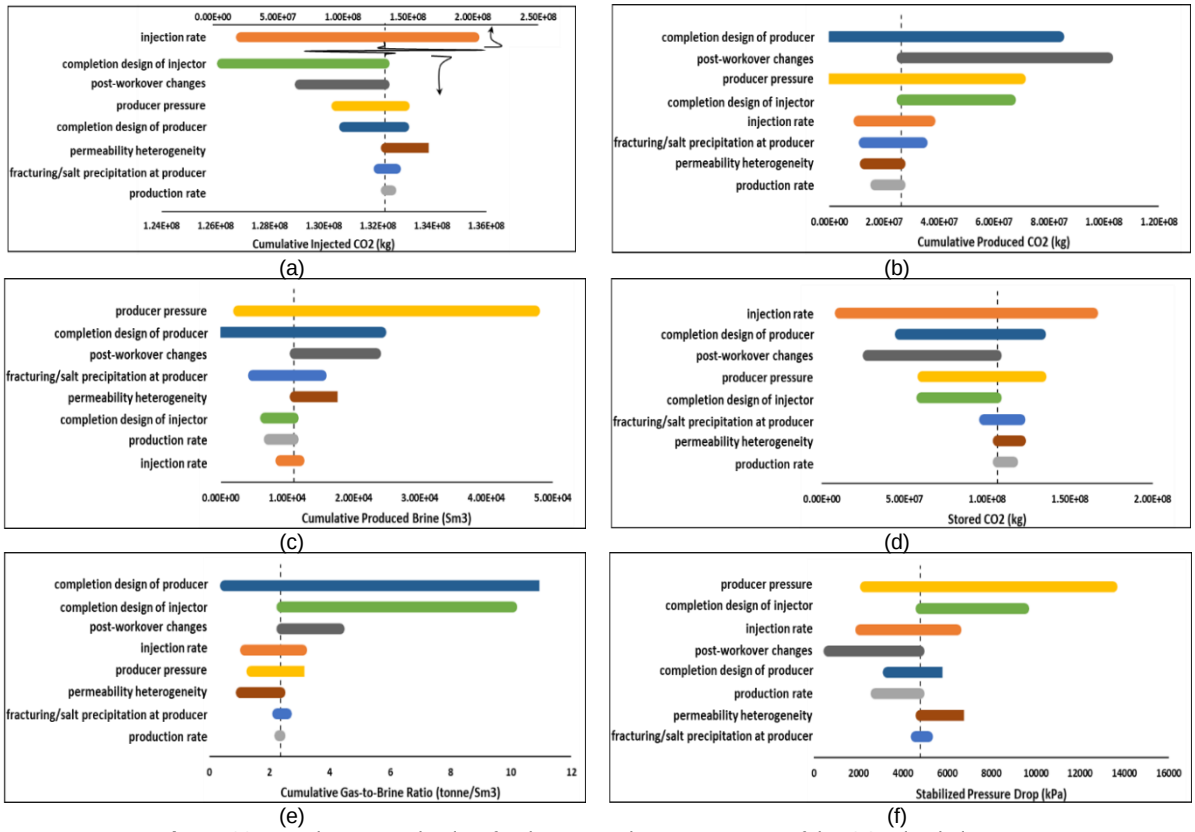

Figure 32: Resultant tornado plots for the uncertainty assessment of the CO_2 circulation test

As explained earlier, significant amounts of CO_2 could be permanently trapped in the saline formation during the CO_2 circulation test. **Figure 32-(d)** shows the injection rate primarily controls the amount of lost/trapped/stored CO_2. Higher injection rate could lead to development of the CO_2 plume in all directions. Multi-well injection/production scenarios could be investigated to minimize the CO_2 loss and the need for make up fluid at the surface. **Figure 32-(e)** confirms that the operational parameters can be managed to maximize CO_2 production and minimize brine production from the producer. Completion designs of both the injector and producer are the key factors in controlling the gas-to-water ratio. Because the injector has a maximum bottomhole pressure constraint of 42.5 MPa (95% of fracking

pressure), the pressure drop between wells within the CO_2 plume is mostly controlled by bottomhole pressure at the producer.

Finally, it is interesting that simulation results do not change as significantly as expected by realization of different permeabilities. This might be due to the fact that the CO_2 plume has already developed and covers both the injector and producer. Moreover, at Aquistore, CO_2 is actively injected into the plume, and the saline formations are believed to be massive continuous sand bodies with acceptable levels of permeability. There is little to no evidence of a permeability barrier between the two wells. However, an increase in permeability between the two wells (due for instance to post-workover conditions, fracturing, movement of salts away from the wells) can positively affect the flow performance of the CO_2 circulation test. The thermal performance of CO_2 circulation should also be investigated (e.g. CO_2 retention time, heat exchange between CO_2 and the porous saline fluid/formations).

4.3 Simplified Wellbore Dynamics and Thermal Multiphase Flow in Production Well

To estimate the potential complex flow regimes and their impacts on the production well and related co-production of CO_2 and brine, we used simplified two-phase vertical flow models for the CO_2 circulation test. One of the key requirements to effectively produce CO_2 back to the surface is a high production rate; however, high fluid rate can result in water coning around the perforated intervals of the production well (Ezekiel et al. 2021). The simulated CO_2 circulation indicates the co-production of both gas and brine in all cases.

The production of liquid (brine) and gas (CO_2) in the vertical production well can be initially assessed by flow regime maps, as in **Figure 33-(a)**. Based on superficial liquid and gas velocities, the well could undergo fine bubble (mostly liquid), bubble, slug, and annular (mostly gas) flow regimes. For fine bubble and bubble flow, the wellbore is mostly filled with continuous liquid phase whereas the gas phase is distributed as fine/small bubbles within the liquid. Higher gas flow rate causes the small gas bubbles to coalesce, forming large bubbles. The gas bubbles could get sufficiently large to fill most of the pipe/wellbore cross section, with some volume of the gas existing as entrained small bubbles in the liquid between the large bubbles. The large bubbles will become unstable and collapse at higher gas flow rates – churn flow – until it reaches a point where the gas is the dominant phase in the wellbore; the continuous gas phase would then carry the liquid droplets by itself, i.e. annular flow (Taitel et al. 1980).

Since the flow in the production well is in upward direction and CO_2 could expand much more than the brine, flowing towards surface, the flow regime at the well perforations (downhole) is of significance in our calculations. With an increase in the CO_2 flow rate, the flow regime could go from bubble to slug/churn to annular flow (**Figure 33**). This transition to annular flow is the favorable flow regime for CO_2 circulation in order to avoid liquid loading (Ezekiel et al. 2021, Hau et al. 2021). If the gas flow rate is not sufficiently high, the liquid could fall to the bottom of the wellbore near the perforated intervals and accumulate, referred to as liquid loading. The liquid loading in the wellbore during CO_2 circulation could eventually kill the well if pumping is not provided; this was one of the speculations for the Cranfield test (Ezekiel et al. 2021, Hau et al. 2021).

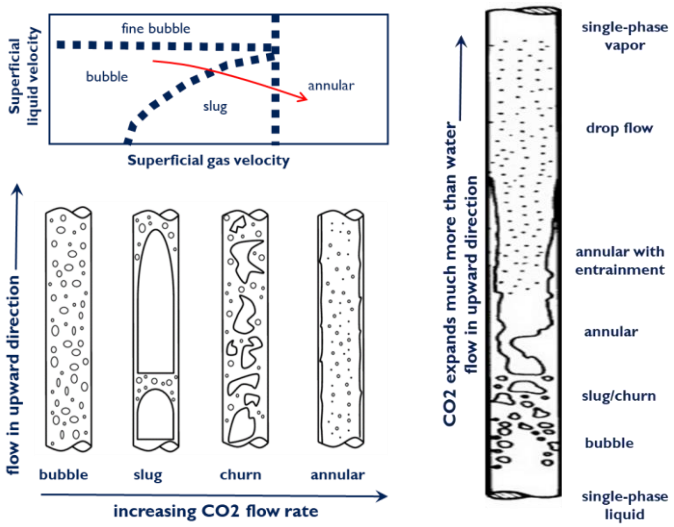

(a) (b)

Figure 33: (a) different two-phase flow regimes in vertical well and (b) how CO_2/brine multiphase flow could evolve in a vertical well (modified after Taitel et al. 1980; Lienhard and Lienhard, 2008)

For the simplified two-phase flow in the vertical wellbore, we used the steady-state equations from Taitel et al. (1980). The equations estimate the transition boundaries between flow regimes based on the superficial liquid and gas velocities as follows:

Bubble flow:

$$U_{S,L} = 4\left\{\frac{D^{0.429}(\sigma/\rho_L)^{0.089}}{(\mu_L/\rho_L)^{0.072}}\left[\frac{\Delta\rho g}{\rho_L}\right]^{0.446}\right\} - U_{S,G}$$

Slug/churn flow:

$$U_{S,L} = -1.15\left[\frac{\sigma\Delta\rho g}{\rho_L^2}\right]^{0.25} + 3U_{S,G}$$

Annular flow:

$$U_{S,G} = 3.1\left[\frac{\sigma\Delta\rho g}{\rho_G^2}\right]^{0.25}$$

where $U_{S,L}$ is superficial liquid velocity, $U_{S,G}$ is superficial gas velocity, D is wellbore diameter, σ is interfacial tension, ρ_L is liquid density, ρ_G is gas density, $\Delta\rho$ is the density difference between liquid and gas phases, μ_L is liquid viscosity, and g is gravitational acceleration. It seems that only the bubble flow regime depends on the wellbore diameter. To calculate the superficial velocities, we divided the simulated flow rates at the producer by the cross-sectional area of the production wellbore. The assumptions were 11 to 33 cm wellbore diameter, average pressure of 36 MPa, average temperature of 115 °C, brine salinity of 300000 ppm, CO_2/brine interfacial tension of 0.033 mN/m, brine density of 1087 kg/m3, CO_2 density of 667 kg/m3, gravitational acceleration of 9.81 N/kg, and brine viscosity of 0.0001 Pa.s (Pruess and Garcia 2002; Bachu and Bennion 2009; Pereira et al. 2017; Rangriz Shokri et al. 2019; Ezekiel et al. 2021).

Figure 34 provides the flow regime maps for different simulated cases of the CO_2 circulation test. Overall, a higher injection rate at the injector helps the transition from bubble flow to annular flow (**Figure 34-a**). It is better not to limit the production rate at the producer (**Figure 34-b**); yet we should maintain

the lowest practical bottomhole pressure at the producer (**Figure 34-c**). The production well would benefit from a workover operation prior to a CO_2 circulation test (**Figure 34-d**) with optimized completion designs for both the injector and producer in order to achieve an annular flow regime (**Figure 34-e**). Production from a limited section of perforated intervals might reduce the gas flow rate and cause a delay for the wellbore to experience annular flow regime (**Figure 34-f**).

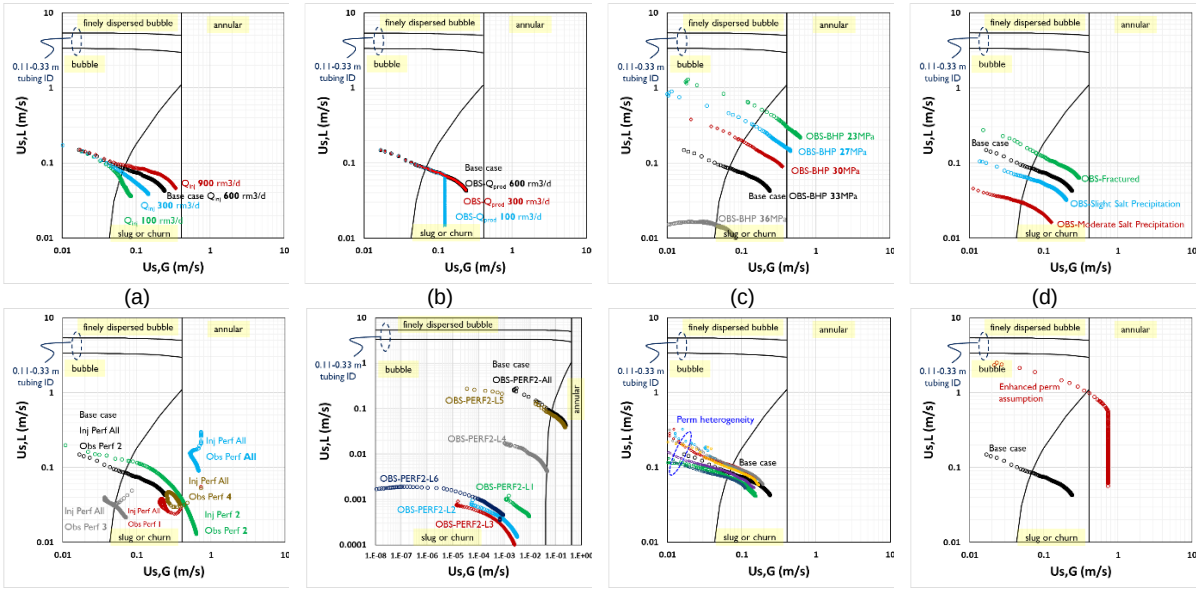

Figure 34: Flow regime maps for different simulated cases of CO_2 circulation test.

If the CO_2 plume has been already developed between two wells, as in the Aquistore site, slight heterogeneity in permeability might not be of huge significance (**Figure 34-g**); this is not the case when shale barriers are expected between injector and producer within the CO_2 plume. Enhancement in permeability/injectivity between two wells due, for instance, to post-workover conditions (e.g. fracturing, salt removal) significantly helps the CO_2 circulation test; it pushes the flow regime in the production wellbore to favorable annular flow regimes (**Figure 34-h**).

5.4 Comments on CO_2 Clathrate Formation

Extensive work on transportation of natural gas suggests that the presence of small gas molecules with water at conditions of high pressure and low temperature might result in the formation of crystalline compounds, called gas hydrates. Hydrates are solid structures of water lattice surrounding trapped gas molecules due to hydrogen bonding, an attractive interaction of a hydrogen atom with an electronegative atom (e.g. oxygen) from another molecule. The thermodynamics of hydrate formation could be very complex, but essentially it requires the presence of water/ice, suitably sized gas/liquid molecules (e.g. CH_4, CO_2), suitable temperature and pressure conditions, and proper gas/liquid/water compositions. Often, hydrates are expected when there is high pressure, low temperature conditions (e.g. sea beds), or there is an abrupt change in pressure/temperature (e.g. chokes, regulators, vents, safety valves) and there is a flow of water in liquid or vapour with suitably sized molecules. To predict hydrate formation, a hydrae phase boundary could be estimated from theory or experiment (Circone et al. 2003; Chapoy et al. 2011, 2014; Pereira et al. 2017; Thoutam et al. 2019) (**Figure 35**).

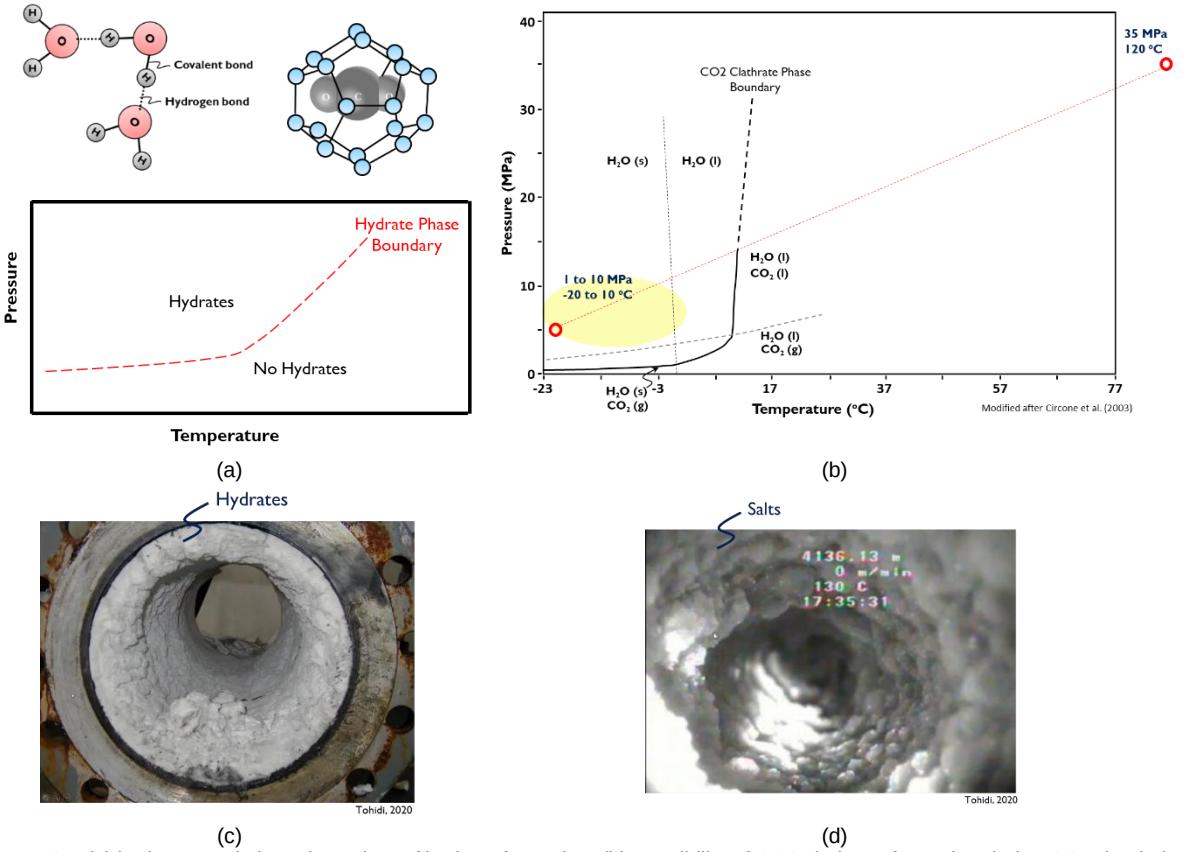

Figure 35: (a) hydrates and phase boundary of hydrate formation, (b) possibility of CO2 clathrate formation during CO_2 circulation test at the Aquistore, (c) hydrates could restrict the flow in the pipe/tubing, (d) hydrates could exclude salts from aqueous phase, resulting in salt precipitation.

CO_2 hydrates, CO_2 molecules trapped in water lattice, are often referred to as CO_2 clathrate. In the CO_2 circulation test, clathrate could form just from a bend in the tubing due to cooling associated with pressure/temperature drops during flow around a corner/bend. Clathrates can restrict the flow in the pipe/tubing. Clathrates can form in the presence of brine (water with high salinity). This will take the water molecules and exclude salts from the aqueous phase, resulting in salt formation.

Hydrate formation is case specific and a strong function of temperature, pressure, and compositions of aqueous and gas phases (Circone et al. 2003; Chapoy et al. 2011, 2014; Pereira et al. 2017; Thoutam et al. 2019). Case specific conditions should be properly investigated. We did not look at the severity of CO_2 clathrate on wellbore/pipe blockage, reduced flow rates, or salt precipitation. But given the downhole and surface conditions of the Aquistore site, our simplified analysis indicates the possibility of CO_2 clathrate formation during CO_2 circulation test at Aquistore (**Figure 35-b**). One of the siphon stages of the Cranfield pilot test was also heavily impacted by the formation of CO_2 clathrate at surface (Pan et al. 2018), but an increase of temperature above the formation point of CO_2 clathrate could solve the problem. It is recommended that CO_2 clathrate formation be examined prior to a CO_2 circulation pilot test; there are different options in order to avoid and/or remediate the adverse effects of CO_2 clathrate formation at downhole and surface conditions.

5 Conclusions

A summary of the main observations and remarks from the CO_2 simulation study is provided below.

- Simulations suggest that CO_2 circulation seems feasible at Aquistore, but it needs significant work on front end engineering design prior to a pilot test.
- Simulations suggest we do not continuously produce huge volumes of brine from the aquifer. An early brine breakthrough is expected and it does not mean the test is unsuccessful. It is recommended that a surface facility be prepared to handle the early brine production and continue the CO_2 circulation test.
- CO_2 makeup fluid is required during the CO_2 circulation test. In all simulated cases, a significant amount of injected CO_2 will be stored in the saline aquifer.
- Operating conditions can be optimized to have a successful CO_2 circulation test (e.g. injection/production rates, pressure drops, completion designs at both injector and producer, among others).
- Heterogeneity, in particular shale barriers, has a negative impact on the flow performance of CO_2 circulation. The evidence of post-workover changes in the saline aquifer should be thoroughly investigated.
- Well stimulation (e.g. localized fracturing or salt removal) at both injection and observation wells improves the CO_2 circulation test.
- Formation of CO_2 clathrate during CO_2 circulation operation is possible and could result in tubing/pipes blockage, reduced flow rates, or salt precipitation. Ways to avoid or remediate the CO_2 clathrate at downhole and surface conditions should be investigated.

6 Outlook and next steps

The major next step is to develop the Front-End Engineering and Design (FEED) study for the CO_2 circulation pilot test at the Aquistore site. The developed model in this study can be enhanced with learning from the Deep Earth Energy Production (DEEP) geothermal project in Saskatchewan, extended or adapted for deployment of CPG technology to ensure that activities involved in a CPG pilot at Aquistore do not impose a risk to the integrity of the existing CO_2 storage complex. Some of the specific issues include:

- As a part of a future uncertainty assessment, we need to explore heat extraction behavior during the CO_2 circulation test. This also includes the impact of potential thermally induced fractures and their propagation (short circuiting the injction/production wells).
- Future work should address CO_2 loss, and the need for make-up fluid, brine disposal, voidage replacement, and pressure management.
- Locating the production well within the CO_2 plume is of interest: the developed model can be used to determine the location of a new producer, or an additional brine well for brine disposal, to manage reservoir pressure in future studies.
- The geochemistry of supercritical CO_2 (brine/CO_2/rock), is not well characterized. Future work is needed to predict possible long-term changes in reservoir porosity and permeability.

7 National and international cooperation

This research was funded by the Swiss Federal Office of Energy (SFOE) under research contract SI/502043-01 and the Petroleum Technology Research Centre (PTRC). We gratefully acknowledge the Petroleum Technology Research Centre, Regina, Saskatchewan, for additional recommendations, and access to data. We wish to thank Norm Sacuta for his review of this report. Thanks are extended to Prof. Martin Saar and his Geothermal Energy & Geofluids Group, especially Mr. Kevin Hau, Institute of Geophysics, ETH Zurich, Zurich, Switzerland, Mr. Gunter Siddiqi of SFOE, Dr. Don White, Geological Survey of Canada, and Dr. Stephen Talman, University of Alberta. We acknowledge Schlumberger for providing the Petrel software package, and Computer Modelling Group LTD. for providing the CMG Software package.

8 Communication

Not applicable.

9 Publications

Published

Hau, K.P., **Rangriz Shokri, A.**, Chalaturnyk, R.J., Saar, M.O. (2021) On the Suitability of the Aquistore CCS-site for a CO_2-Circulation Test, World Geothermal Congress, Reykjavik, Iceland, May 21 – 26.

Hau, K.P., **Rangriz Shokri, A.**, Nickel, E., Chalaturnyk, R.J., Saar, M.O. (2021) Modeling CO2Circulation Test, as a Key Element of CO_2 Plume Geothermal, at An Active CO_2 Storage Site, GeoConvention Conference, Virtual Event, September 13-15.

Chalaturnyk, R.J., **Rangriz Shokri, A.** (2021) Advancing Canadian Experience and Best Practices in Containment, Conformance, and Injectivity of Deep Subsurface CO_2 Storage, CO_2 EOR, and CO_2 Geothermal, GeoConvention Conference, Virtual Event, September 13-15.

In preparation

Rangriz-Shokri, A., Hau, K.P., Saar, M.O., Chalaturnyk, R.J., White, D.J., Nickel, E., Siddiqi, G. On the Feasibility of CO_2 Circulation Test for Sustainable Geothermal Power Generation at the Aquistore Storage Site, Saskatchewan, Canada

10 References

Adams, B.M., Kuehn, T.H., Bielicki, J.M., Randolph, J.B., Saar, M.O., (2015) A comparison of electric power output of CO2 Plume Geothermal (CPG) and brine geothermal systems for varying reservoir conditions. Appl. Energy 140, 365–377. https://doi.org/10.1016/J.APENERGY.2014.11.043

Adams, B.M., Kuehn, T.H., Bielicki, J.M., Randolph, J.B., Saar, M.O., (2014) On the importance of the thermosiphon effect in CPG (CO2 plume geothermal) power systems. Energy 69, 409–418. https://doi.org/10.1016/j.energy.2014.03.032

Atrens, A., Gurgenci, H., Rudolph, V., (2009) Exergy analysis of a CO2 thermosiphon, in: Proceedings of the Thirty-Fourth Workshop on Geothermal Reservoir Engineering. Stanford, California, pp. 1–6.

Bachu, S., Adams, J. (2003) Sequestration of CO2 in Geological Media in Response to Climate Change - Capacity of Deep Saline Aquifers to Sequester CO2 in Solution. Energy Conversion and Management, 44(20): 3151–3175.

Bachu, S., Faltinson, J., Hauck, T., Perkins, E., Peterson, J., Talman, S., Jensen, G. (2011) The Basal Aquifer in the Prairie Region of Canada - Characterization for CO2 Storage. Preliminary Report for Stage I (Phases 1 and 2), Alberta Innovates Technology Futures.

Bachu, S., Brant Bennion, D., (2009) Interfacial Tension between CO2, Freshwater, and Brine in the Range of Pressure from (2 to 27) MPa, Temperature from (20 to 125) °C, and Water Salinity from (0 to 334 000) mg·L−1. J. Chem. & Eng. Data 54, 765–775. https://doi.org/10.1021/je800529x

Batzle, M. and Wang, Z. (1992) Seismic properties of pore fluids, Geophysics, Vol. 57, No. 11, Nov. 1992, pp.1396-1408.

Bennion, D.B. and Bachu, S. (2006a) Supercritical CO2 and H2S Brine Drainage and Imbibition Relative Permeability Relationships for Integral Sandstone and Carbonate Formations, Paper SPE 99326, SPE Europec/Eage Annual Conference and Exhibition, Vienna, Austria, 12 15 June.

Bennion, D.B. and Bachu, S. (2006b) Supercritical CO2 and H2S Brine Drainage and Imbibition Relative Permeability Relationships for Integral Sandstone and Carbonate Formations, Paper SPE 99325, SPE/DOE Symposium on Improved Oil Recovery, Tulsa, Oklahoma, 22 26 April.

Brown, D., (2000) A Hot Dry Rock geothermal energy concept utilizing supercritical CO2 instead of water. In: Proceedings of the Twenty-Fifth Workshop on Geothermal Reservoir Engineering, Stanford University, pp. 233–238.

Chapoy, A., Burgass, R., Tohidi, B., Austell, J. M.; Eickhoff, C. (2011) Effect of common impurities on the phase behavior of carbon-dioxide-rich systems: Minimizing the risk of hydrate formation and two-phase flow. SPE J., 16, 921−930.

Chapoy, A., Burgass, R., Tohidi, B., Alsiyabi, I. (2014) Hydrate and phase behavior modeling in CO2-rich pipelines. J. Chem. Eng. Data, 60, 447−453.

Circone, S., Stern, L.A., Kirby, S.H., Durham, W.B., Chakoumakos, B.C., Rawn, C.J., Rondinone, A.J., Ishii, Y. (2003) CO2 Hydrate: Synthesis, Composition, Structure, Dissociation Behavior, and a Comparison to Structure I CH4 Hydrate, he Journal of Physical Chemistry B 2003 107 (23), 5529-5539; DOI: 10.1021/jp027391j

Coats, K.H., (1977) Geothermal Reservoir Modelling, in: SPE Annual Fall Technical Conference and Exhibition. Society of Petroleum Engineers, Denver, Colorado, p. 33. https://doi.org/10.2118/6892-MS

Delshad, M., Kong, X., Tavakoli, R., Hosseini, S.A., Wheeler, M.F., (2013) Modeling and simulation of carbon sequestration at Cranfield incorporating new physical models. Int. J. Greenh. Gas Control 18, 463–473. https://doi.org/10.1016/j.ijggc.2013.03.019

Ezekiel, J., Adams, B.M., Saar, M.O., Ebigbo, A. (2021) Numerical analysis and optimization of the performance of CO2-Plume Geothermal (CPG) production wells and implications for electric power generation, Geothermics, in review.

Ezekiel, J., Ebigbo, A., Adams, B.M., Saar, M.O., (2020) Combining natural gas recovery and CO2-based geothermal energy extraction for electric power generation. Appl. Energy 269, 1–21. https://doi.org/https://doi.org/10.1016/j.apenergy.2020.115012

Fleming, M.R., B.M. Adams, J.B. Randolph, J.D. Ogland-Hand, T.H. Kuehn, T.A. Buscheck, J.M. Bielicki, M.O. Saar (2018), High Efficiency and Large-scale Subsurface Energy Storage with CO2 PROCEEDINGS, 43rd Workshop on Geothermal Reservoir Engineering Stanford University, Stanford, California, February 12-14.

Fleming, M.R., Adams, B.M., Kuehn, T.H., Bielicki, J.M., Saar, M.O., (2020) Increased Power Generation due to Exothermic Water Exsolution in CO2 Plume Geothermal (CPG) Power Plants. Geothermics 88, 101865. https://doi.org/https://doi.org/10.1016/j.geothermics.2020.101865

Fouillac, C., Sanjuan, B., Gentier, S., Czernichowski-Lauriol, I., (2004) Could sequestration of CO2 be combined with the development of Enhanced Geothermal Systems? Paper presented at Third Annual Conference on Carbon Capture and Sequestration, Alexandria, VA.

Freifeld, B.M., Pan, L., Doughty, C., Zakem, S., Hart, K., Hostler, S., (2016) Demonstration of Geothermal Energy Production Using Carbon Dioxide as a Working Fluid at the SECARB Cranfield Site, Cranfield, Mississippi, in: Proceedings, 41st Workshop on Geothermal Reservoir Engineering. pp. 1–14.

Garapati, N., Randolph, J.B., Saar, M.O., (2015) Brine displacement by CO2, energy extraction rates, and lifespan of a CO2-limited CO2-Plume Geothermal (CPG) system with a horizontal production well. Geothermics 55, 182–194. https://doi.org/10.1016/j.geothermics.2015.02.005

Harvey, A. (1996) Semiempirical Correlation for Henry's Constants over Large Temperature Ranges. American Institute of Chemical Engineers Journal, 42(5):1491-1494.

Hau, K.P., Rangriz Shokri, A., Chalaturnyk, R.J., Saar, M.O. (2021) On the Suitability of the Aquistore CCS-site for a CO2-Circulation Test, World Geothermal Congress, Reykjavik, Iceland, May 21 – 26.

Hau, K. P. (2020) Feasibility of a CO2 Plume Geothermal (CPG) Pilot at the Aquistore (Canada) CCS site, MA thesis. ETH Zürich.

Hovorka, S.D., Meckel, T.A., Trevino, R.H., (2013) Monitoring a large-volume injection at Cranfield, Mississippi – project design and recommendations. Int. J. Greenh. Gas Control 18, 345–360.

Jiang, T., Pekot, L.J., Jin, L., Peck, W.D., Gorecki, C.D. (2016) Geological Modeling and Simulation Report for the Aquistore Project. Plains CO2 Reduction (PCOR) Partnership Phase III, Task 1 - Deliverable D93, Update 2, National Energy Technology Laboratory, February.

Kennedy, M. (2017). Interpreting CO2 Saturation Changes from Pulsed Neutron Logs at the Aquistore Site. Report for the Petroleum Technology Research Centre.

Kestin, J., Khalifa, H.E., Correia, R.J. (1981) Tables of Dynamic and Kinematic Viscosity of Aqueous NaCl Solutions in the Temperature Range 20-150 °C and the Pressure Range 0.1-35 MPa, Journal of Physical and Chemical Reference Data, 10: 71-87.

Kurz, M., Heebink, L., Smith, S., Zacher, E. (2014) Petrophysical Evaluation of Core from the Aquistore CO2 Injection Site. Plains CO2 Reduction (PCOR) Partnership value-added report for U.S. Department of Energy National Energy Technology Laboratory Cooperative Agreement No. DE-FC26-05NT42592, EERC Publication 2014-EERC-07-16, Grand Forks, North Dakota, Energy & Environmental Research Center, March.

Lee, S-Y, Swager, L., Pekot, L., Piercey, M., Will, R., Zaluski, W. (2018) Study of operational dynamic data in Aquistore project, International Journal of Greenhouse Gas Control, 76: 62-77, https://doi.org/10.1016/j.ijggc.2018.06.008.

Lienhard and Lienhard, (2008) A Heat Transfer Textbook, Reupublished, Fifth Edition, Dover Pubns; Reprint edition (Dec 18 2019).

Levy, E.K., Wang, X., Pan, C., Romero, C.E., Maya, C.R., (2018) Use of hot supercritical CO2 produced from a geothermal reservoir to generate electric power in a gas turbine power generation system. J. CO2 Util. 23, 20–28. https://doi.org/10.1016/J.JCOU.2017.11.001

Marfurt, K.J., Scheet, R.M., Sharp, J.A., and Harper, M.G., (1998) Suppression of the acquisition footprint for seismic sequence attribute mapping: Geophysics, Vol. 63, No. 3, p. 1024-1035.

Movahedzadeh, Z., Rangriz Shokri, A., Chalaturnyk, R.J., Nickel, E., Sacuta, N. (2021) Measurement, Monitoring, Verification and Modelling at the Aquistore CO2 Storage Site, EAGE First Break 39(2):69-75 DOI: 10.3997/1365-2397.fb2021013

Nielsen, C.M., Frykmana, P., Dalhoffb, F. (2013) Synergy benefits in combining CCS and geothermal energy production, Energy Procedia 37: 2622 – 2628

Pan, L., Doughty, C., Freifeld, B., (2018) How to sustain a CO2-thermosiphon in a partially saturated geothermal reservoir: Lessons learned from field experiment and numerical modeling. Geothermics 71, 274–293. https://doi.org/10.1016/j.geothermics.2017.10.004

Pan, L., Doughty, C., Freifeld, B., Oldenburg, C., (2015) Modeling a CO2 thermosiphon in a partially saturated reservoir using EOS7CMA, in: Proceedings, TOUGH Symposium 2015, Lawrence Berkeley National Laboratory, Berkeley, CA, September 28–30.

Peck, W.D., Bailey, T.P., Liu, G., Klenner, R.C.L, Gorecki, C.D., Ayash, S.C., Steadman, E.N., Harju, J.A. (2014a) Model Development of the Aquistore CO2 Storage Project, Energy Procedia, 63: 3723-3734.

Peck, W., Klenner, R., Liu, G., Gorecki, C., Steadman, E. (2014b) Geological Modeling and Simulation Report for the Aquistore Project. Plains CO2 Reduction (PCOR) Partnership Phase III, Task 1 - Deliverable D93, National Energy Technology Laboratory, March.

Pereira, L.M.C., Chapoy, A., Burgass, R., Tohidi, B. (2017) Interfacial tension of CO2 + brine systems: Experiments and predictive modelling, Advances in Water Resources 103 (2017) 64–75

Pruess, K., (2008) On production behavior of enhanced geothermal systems with CO2 as working fluid. Energy Convers. Manag. 49, 1446–1454. https://doi.org/https://doi.org/10.1016/j.enconman.2007.12.029

Pruess, K., Azaroual, M., (2006) On the feasibility of using supercritical CO2 as heat transmission fluid in an Engineered Hot Dry Rock Geothermal System. In: Proceedings of the Thirty-First Workshop on Geothermal Reservoir Engineering, Stanford University, Stanford, CA, USA, pp. 386–393.

Pruess, K., Garcia, J.E., (2002) Multiphase flow dynamics during CO2 injection into saline aquifers. Environ. Geol. 42, 282–295.

Ramey Jr., H.J., (1962) Wellbore heat transmission. J. Pet. Technol. (April), 427–435.

Randolph, J.B., Adams, B., Kuehn, T.H., Saar, M.O., (2012) Wellbore heat transfer in CO2-based geothermal systems. Geotherm Resour Counc. Trans.

Randolph, J.B., Saar, M.O., (2011a) Combining geothermal energy capture with geologic carbon dioxide sequestration. Geophys. Res. Lett. 38, 1–7. https://doi.org/10.1029/2011GL047265

Randolph, J.B. and M.O. Saar (2011b) Coupling carbon dioxide sequestration with geothermal energy capture in naturally permeable, porous geologic formations: Implications for CO 2 sequestration, Energy Procedia, doi.org/10.1016/j.egypro.2011.02.108 , 4:2206-2213.

Rangriz Shokri, A., Talman, S., Chalaturnyk, R.J., Nickel, E. (2021) On the Temporal Evolution of Non-Isothermal Injectivity Behaviour at an Active CO2 Injection Site, 55th US Rock Mechanics Geomechanics Symposium, ARMA, Houston, TX, June 20-23.

Rangriz Shokri, A., R. J. Chalaturnyk, and E. Nickel (2019). “Non-Isothermal Injec- tivity Considerations for Effective Geological Storage of CO2 at the Aquistore Site, Saskatchewan, Canada”. In: SPE Annual Technical Conference and Exhibition. Society of Petroleum Engineers. doi: 10.2118/196118-ms.

Roach, L.A.N. & White, D.J. (2018). Evolution of a deep CO 2 plume from time-lapse seismic imaging at the Aquistore storage site, Saskatchewan, Canada. Int J Greenhouse Gas Control 74: 79-86.

Rostron, B., White, D., Hawkes, C., Chalaturnyk, R.J. (2014). Characterization of the Aquistore CO2 project storage site, Saskatchewan, Canada". In: Energy Procedia 63, pp. 2977–2984. doi: 10.1016/j.egypro.2014.11.320.

Rowe, A.M., Chou, J.C.S. (1970) Pressure–Volume–Temperature-Concentration Relation of Aqueous NaCl Solutions, Journal of Chemical Engineering Data, 15(1): 61-66.

Saar, M.O. (2019) CO2 Circulation Test at Aquistore: The World's First Field Test of the CO 2 –Plume Geothermal (CPG) Technology, a proposal submitted to PTRC.

Schlumberger, (2018) Aquistore 3D – Seismic AVO Inversion and Lithology Prediction Report, PTRC internal report from Schlumberger, 34 p.

Schlumberger Carbon Services (2015) PTRC INJ 05-06-02-08 Production Log, Technical Memorandum.

Schlumberger Reservoir Laboratories (2013) Relative Permeability by Unsteady-State Method. Prepared for Petroleum Technology Research Centre, Well: 5-6-2-8, Regina, Saskatchewan.

Sepulveda, N. A., Jenkins, J. D., de Sisternes, F. J., & Lester, R. K. (2018). The role of firm low-carbon electricity resources in deep decarbonization of power generation. Joule, 2(11), 2403-2420.

Swager, L. (2017) Reservoir Saturation Tool, Monitoring Log Report PTRC OBS 5-6-2-8, PTRC INJ 5-6-2-8, May.

Taitel, Y., Bornea, D., Dukler, A.E., (1980) Modelling flow pattern transitions for steady upward gasliquid flow in vertical tubes. AIChE J. 26, 345–354. https://doi.org/10.1002/aic.690260304

Talman, S., Rangriz Shokri, A., Chalaturnyk, R.J., Nickel, E. (2020) Salt Precipitation at an Active CO 2 Injection Site. doi: 10.1002/9781119593324.ch11.

Thoutam, P., Rezaei Gomari, S., Chapoy, A., Ahmad, F., Islam, M. (2019) Study on CO2 Hydrate Formation Kinetics in Saline Water in the Presence of Low Concentrations of CH4, ACS Omega, 4 (19): 18210-18218, https://doi.org/10.1021/acsomega.9b02157

Ueda, A., Kato, K., Ohsumi, T., Yajima, T., Ito, H., Kaieda, H., Meycalf, R., Takase, H., (2005) Experimental studies of CO2-rock interaction at elevated temperatures under hydrothermal conditions. Geochem. J. 39, 417–425.

White, D., Roach, L., Harris, K., Cheraghi, S., Roberts, B. (2018) Tracking a Deep CO2 Plume: 4D Seismic Imaging at the Aquistore CO2 Storage Site, Saskatchewan, Canada, 14th International Conference on Greenhouse Gas Control Technologies

White, D.J., (2018) Prestack AVO Inversion Footprint Removal, Aquistore internal report, 8p.

White, D., Harris, K., Roach, L., Robertson, M. (2019) 7 years of 4D seismic monitoring at the Aquistore CO2 storage site, Saskatchewan, Canada. Paper presented at the SEG International Exposition and Annual Meeting, San Antonio, Texas, USA, September. doi: https://doi.org/10.1190/segam2019-3216776.1

White, D. J., C. D. Hawkes, and B. J. Rostron (2016). Geological characterization of the Aquistore CO2 storage site from 3D seismic data. In: International Journal of Greenhouse Gas Control 54, pp. 330–344. doi: 10.1016/j.ijggc.2016.10.001.

White, D.J., Rangriz Shokri, A., Chalaturnyk, R.J., (2021) Saline Reservoir Monitoring at an Active CO2 Storage Site, CCUS AAPG Conference, March 23-25.

Willhite, G.P. (1967) Over-all heat transfer coefficients in steam and hot water injection wells: Journal of Petroleum Technology, May, p. 607–615.

Xu, T., Pruess, K., (2004) Numerical simulation of injectivity effects of mineral scaling and clay swelling in a fractured geothermal reservoir. Geotherm. Resour. Council Trans. 28, 269–276.

Xu, T., Apps, J.A., Pruess, K., (2005) Mineral sequestration of carbon dioxide in a sandstone-shale system. Chem. Geol. 217, 295–318.

Zambrano-Narvaez, G, Chalaturnyk, R., Worth, K. (2015) Design and deployment of an integrated instrumentation system in a monitoring well at the Aquistore Geological CO2 storage project, Saskatchewan, Canada, in PM Dight (ed.), Proceedings of the 9th Symposium on Field Measurements in Geomechanics, Australian Centre for Geomechanics, Perth, pp. 717-726

Zhang, L., Cui, G., Zhang, Y., Ren, B., Ren, S., Wang, X., (2016) Influence of pore water on the heat mining performance of supercritical CO2 injected for geothermal development. J. CO2 Util. 16, 287–300. https://doi.org/10.1016/j.jcou.2016.08.008

11 Appendix

Plots related to injection rate

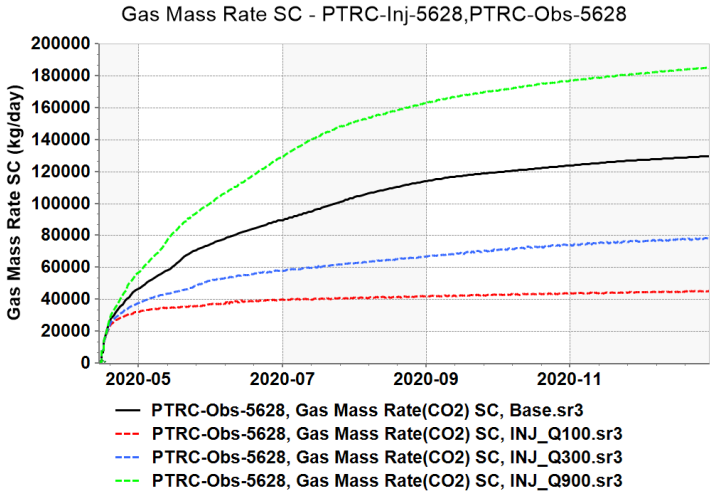

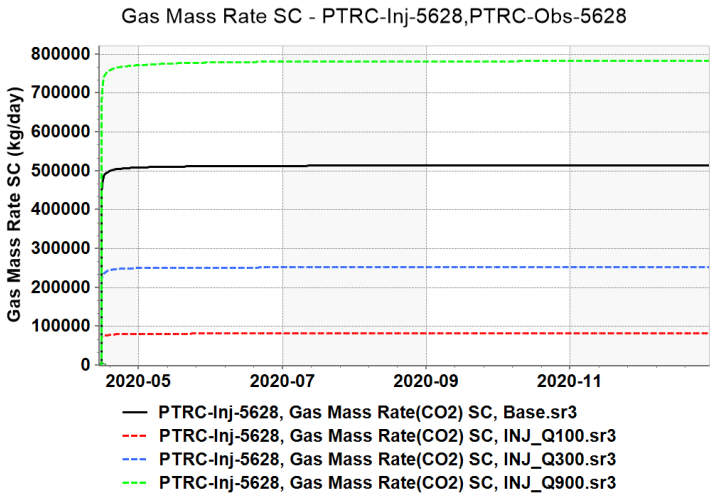

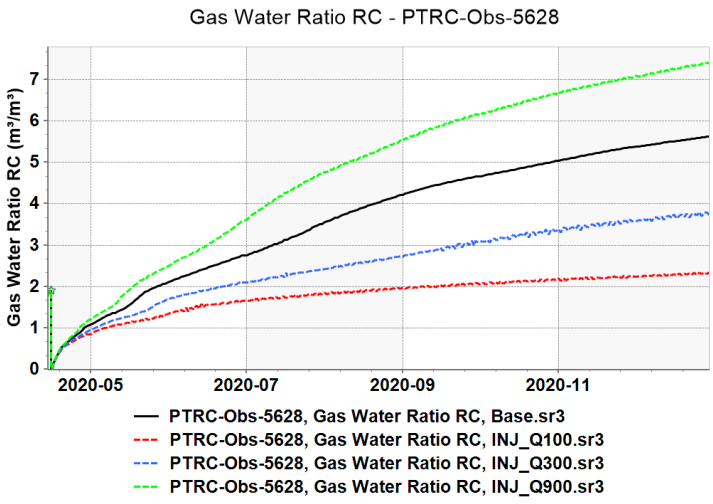

Gas Water Ratio SC - PTRC-Obs-5628

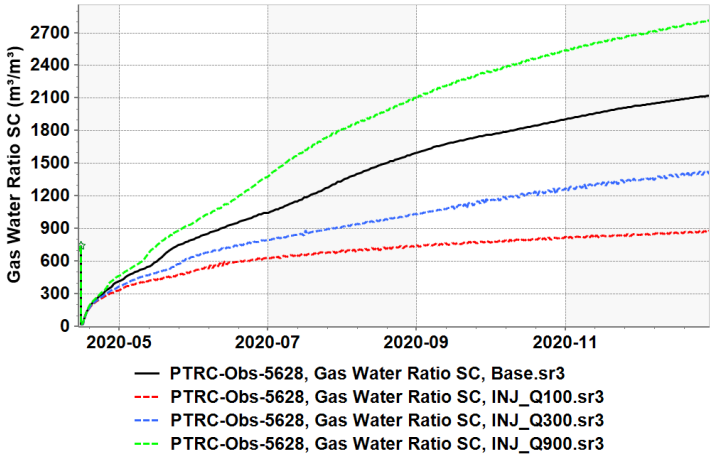

Well Bottom-hole Pressure - PTRC-Inj-5628,PTRC-Obs-5628

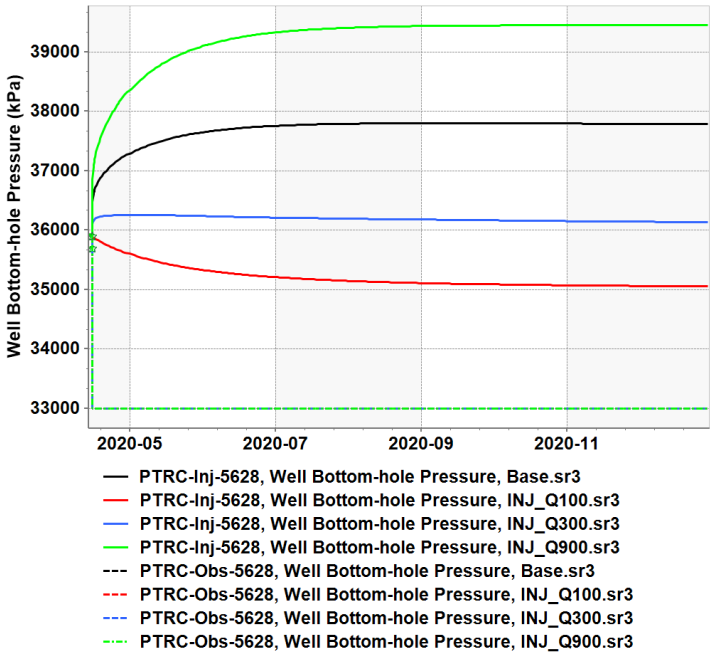

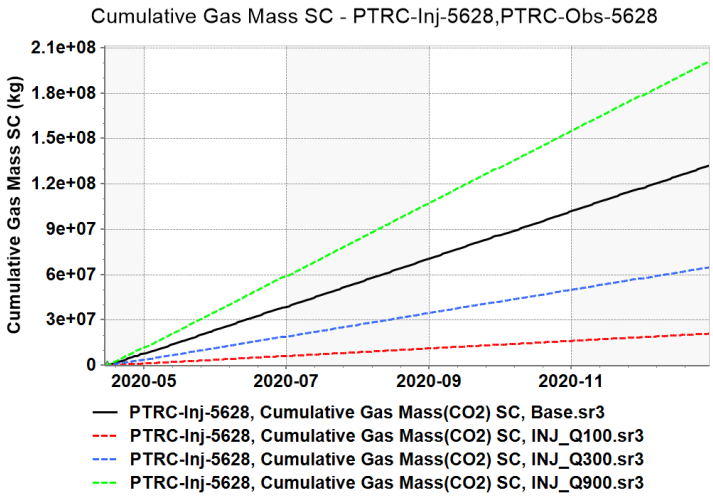
Cumulative Gas Mass SC - PTRC-Inj-5628,PTRC-Obs-5628
Cumulative Gas Mass SC (kg)
2.1e+08
1.8e+08
1.5e+08
1.2e+08
9e+07
6e+07
3e+07
0
2020-05
2020-07
2020-09
2020-11
PTRC-Inj-5628, Cumulative Gas Mass(CO2) SC, Base.sr3
PTRC-Inj-5628, Cumulative Gas Mass(CO2) SC, INJ_Q100.sr3
PTRC-Inj-5628, Cumulative Gas Mass(CO2) SC, INJ_Q300.sr3
PTRC-Inj-5628, Cumulative Gas Mass(CO2) SC, INJ_Q900.sr3

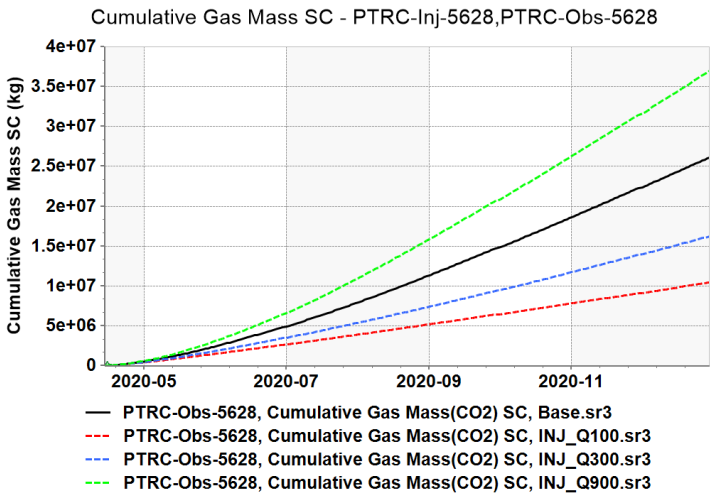
Cumulative Gas Mass SC - PTRC-Inj-5628,PTRC-Obs-5628
Cumulative Gas Mass SC (kg)
4e+07
3.5e+07
3e+07
2.5e+07
2e+07
1.5e+07
1e+07
5e+06
0
2020-05
2020-07
2020-09
2020-11
PTRC-Obs-5628, Cumulative Gas Mass(CO2) SC, Base.sr3
PTRC-Obs-5628, Cumulative Gas Mass(CO2) SC, INJ_Q100.sr3
PTRC-Obs-5628, Cumulative Gas Mass(CO2) SC, INJ_Q300.sr3
PTRC-Obs-5628, Cumulative Gas Mass(CO2) SC, INJ_Q900.sr3

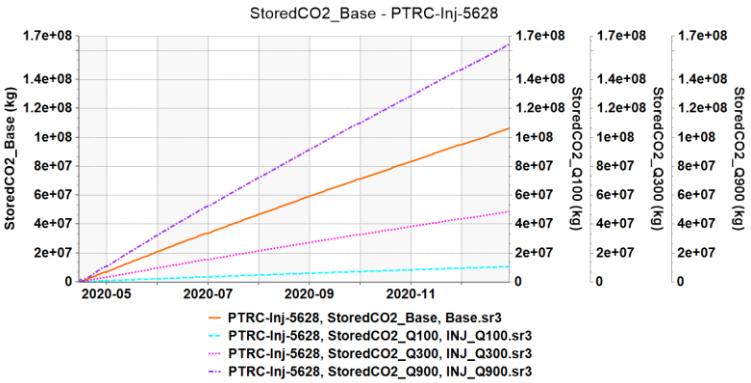
StoredCO2_Base - PTRC-Inj-5628
StoredCO2_Base (kg)
StoredCO2_Q100 (kg)
StoredCO2_Q300 (kg)
StoredCO2_Q900 (kg)
1.7e+08
1.4e+08
1.2e+08
1e+08
8e+07
6e+07
4e+07
2e+07
0
2020-05
2020-07
2020-09
2020-11
PTRC-Inj-5628, StoredCO2_Base, Base.sr3
PTRC-Inj-5628, StoredCO2_Q100, INJ_Q100.sr3
PTRC-Inj-5628, StoredCO2_Q300, INJ_Q300.sr3
PTRC-Inj-5628, StoredCO2_Q900, INJ_Q900.sr3

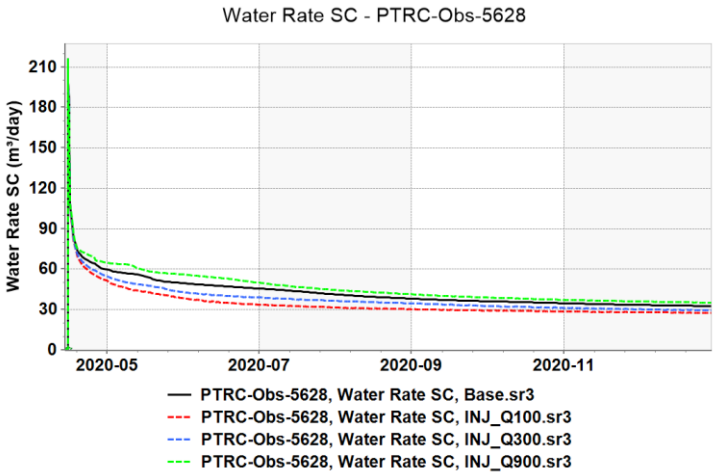
Water Rate SC - PTRC-Obs-5628
Water Rate SC (m³/day)
210
180
150
120
90
60
30
0
2020-05
2020-07
2020-09
2020-11
PTRC-Obs-5628, Water Rate SC, Base.sr3
PTRC-Obs-5628, Water Rate SC, INJ_Q100.sr3
PTRC-Obs-5628, Water Rate SC, INJ_Q300.sr3
PTRC-Obs-5628, Water Rate SC, INJ_Q900.sr3

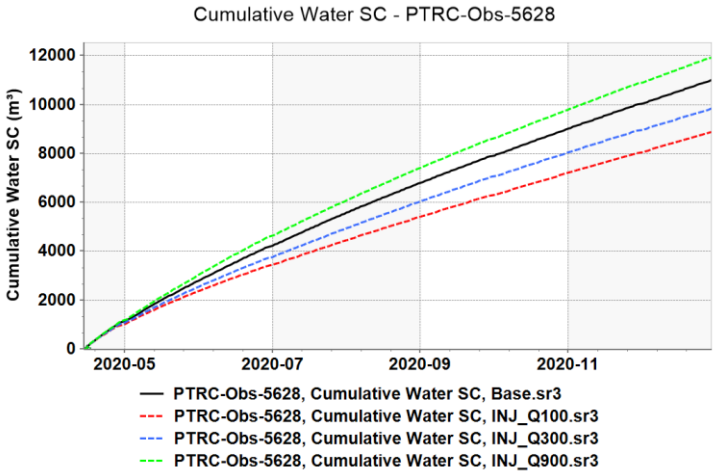
Cumulative Water SC - PTRC-Obs-5628
Cumulative Water SC (m³)
12000
10000
8000
6000
4000
2000
0
2020-05
2020-07
2020-09
2020-11
PTRC-Obs-5628, Cumulative Water SC, Base.sr3
PTRC-Obs-5628, Cumulative Water SC, INJ_Q100.sr3
PTRC-Obs-5628, Cumulative Water SC, INJ_Q300.sr3
PTRC-Obs-5628, Cumulative Water SC, INJ_Q900.sr3

Plots related to bottomhole pressure of producer

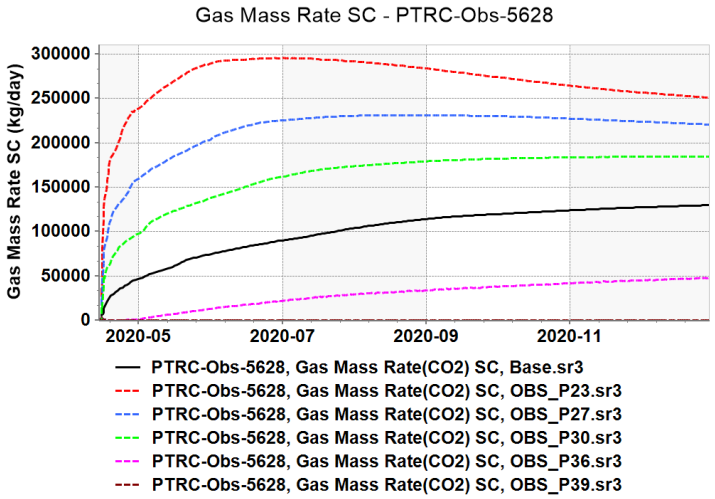

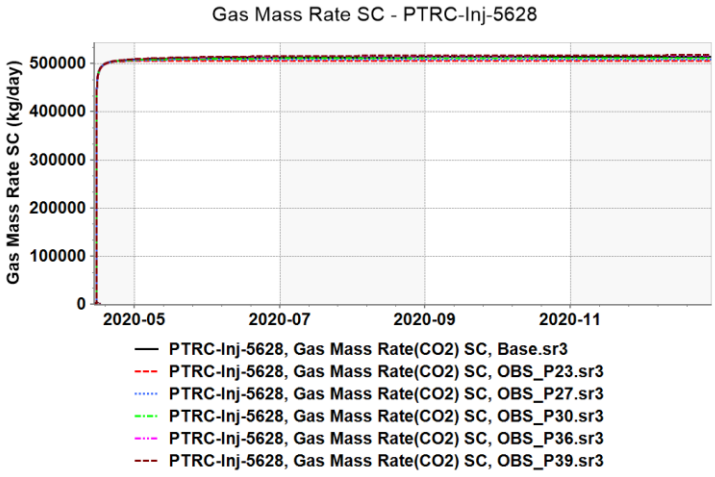

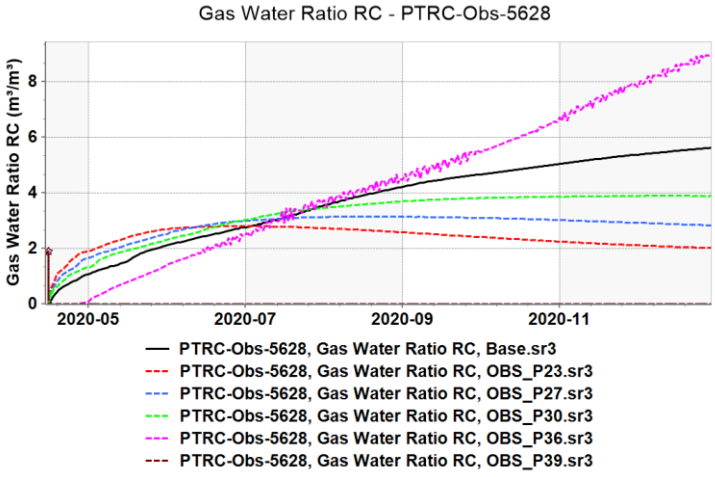

Gas Water Ratio SC - PTRC-Obs-5628

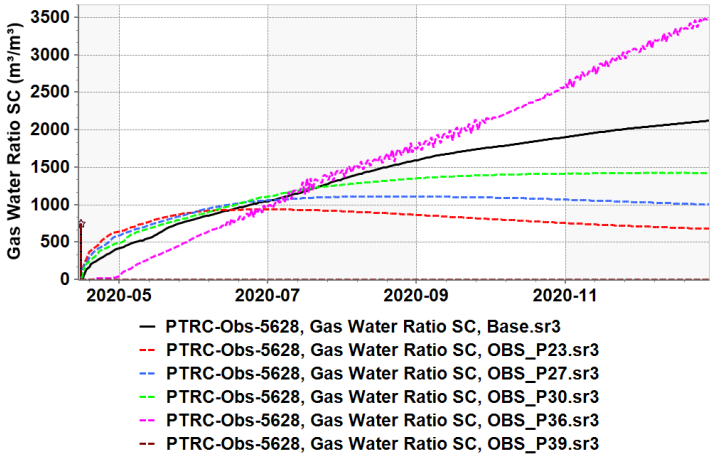

Well Bottom-hole Pressure - PTRC-Inj-5628,PTRC-Obs-5628

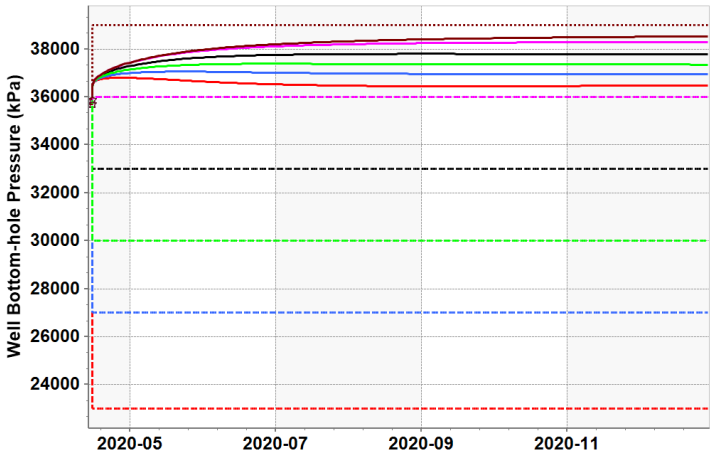

Well Bottom-hole Pressure - PTRC-Inj-5628,PTRC-Obs-5628

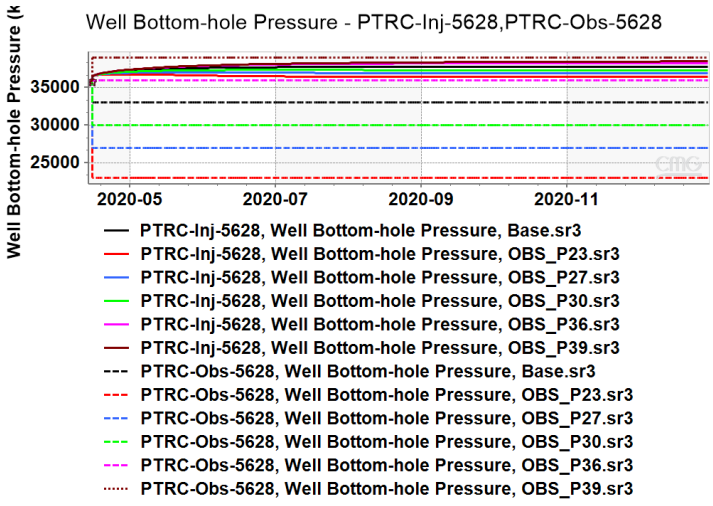

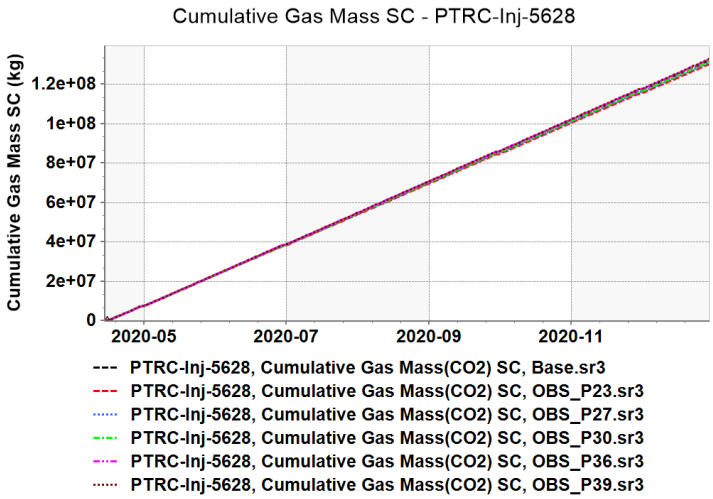
Cumulative Gas Mass SC - PTRC-Inj-5628
Cumulative Gas Mass SC (kg)
1.2e+08
1e+08
8e+07
6e+07
4e+07
2e+07
0
2020-05
2020-07
2020-09
2020-11
PTRC-Inj-5628, Cumulative Gas Mass(CO2) SC, Base.sr3
PTRC-Inj-5628, Cumulative Gas Mass(CO2) SC, OBS_P23.sr3
PTRC-Inj-5628, Cumulative Gas Mass(CO2) SC, OBS_P27.sr3
PTRC-Inj-5628, Cumulative Gas Mass(CO2) SC, OBS_P30.sr3
PTRC-Inj-5628, Cumulative Gas Mass(CO2) SC, OBS_P36.sr3
PTRC-Inj-5628, Cumulative Gas Mass(CO2) SC, OBS_P39.sr3

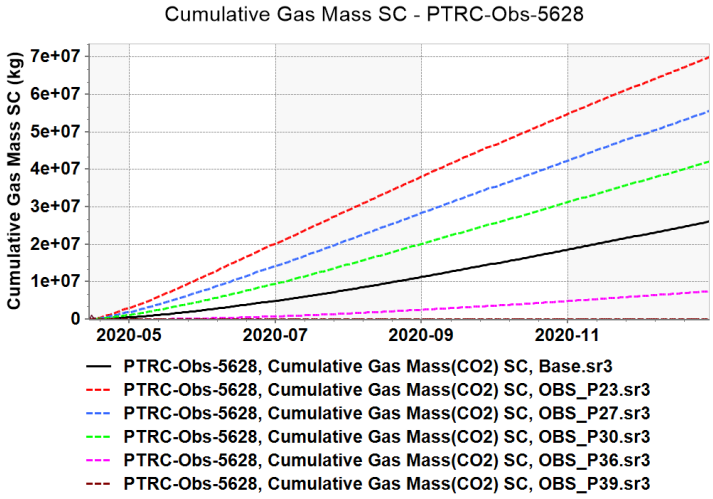
Cumulative Gas Mass SC - PTRC-Obs-5628
Cumulative Gas Mass SC (kg)
7e+07
6e+07
5e+07
4e+07
3e+07
2e+07
1e+07
0
2020-05
2020-07
2020-09
2020-11
PTRC-Obs-5628, Cumulative Gas Mass(CO2) SC, Base.sr3
PTRC-Obs-5628, Cumulative Gas Mass(CO2) SC, OBS_P23.sr3
PTRC-Obs-5628, Cumulative Gas Mass(CO2) SC, OBS_P27.sr3
PTRC-Obs-5628, Cumulative Gas Mass(CO2) SC, OBS_P30.sr3
PTRC-Obs-5628, Cumulative Gas Mass(CO2) SC, OBS_P36.sr3
PTRC-Obs-5628, Cumulative Gas Mass(CO2) SC, OBS_P39.sr3

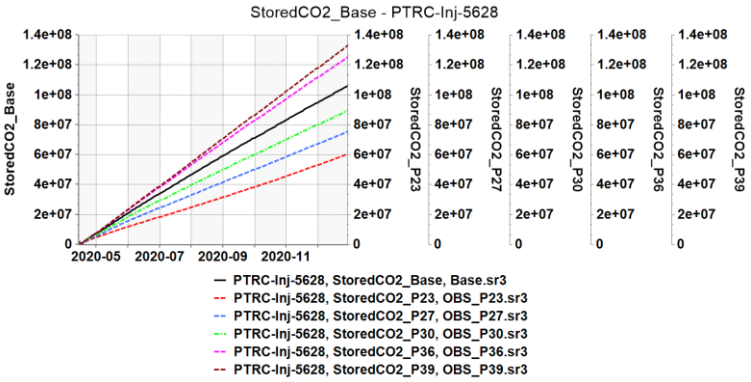
StoredCO2_Base - PTRC-Inj-5628
StoredCO2_Base
StoredCO2_P23
StoredCO2_P27
StoredCO2_P30
StoredCO2_P36
StoredCO2_P39
1.4e+08
1.2e+08
1e+08
8e+07
6e+07
4e+07
2e+07
0
2020-05
2020-07
2020-09
2020-11
PTRC-Inj-5628, StoredCO2_Base, Base.sr3
PTRC-Inj-5628, StoredCO2_P23, OBS_P23.sr3
PTRC-Inj-5628, StoredCO2_P27, OBS_P27.sr3
PTRC-Inj-5628, StoredCO2_P30, OBS_P30.sr3
PTRC-Inj-5628, StoredCO2_P36, OBS_P36.sr3
PTRC-Inj-5628, StoredCO2_P39, OBS_P39.sr3

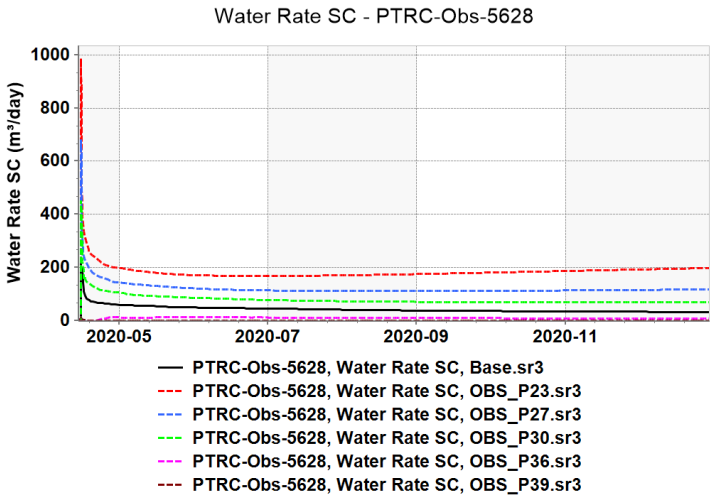
Water Rate SC - PTRC-Obs-5628
Water Rate SC (m³/day)
1000
800
600
400
200
0
2020-05
2020-07
2020-09
2020-11
PTRC-Obs-5628, Water Rate SC, Base.sr3
PTRC-Obs-5628, Water Rate SC, OBS_P23.sr3
PTRC-Obs-5628, Water Rate SC, OBS_P27.sr3
PTRC-Obs-5628, Water Rate SC, OBS_P30.sr3
PTRC-Obs-5628, Water Rate SC, OBS_P36.sr3
PTRC-Obs-5628, Water Rate SC, OBS_P39.sr3

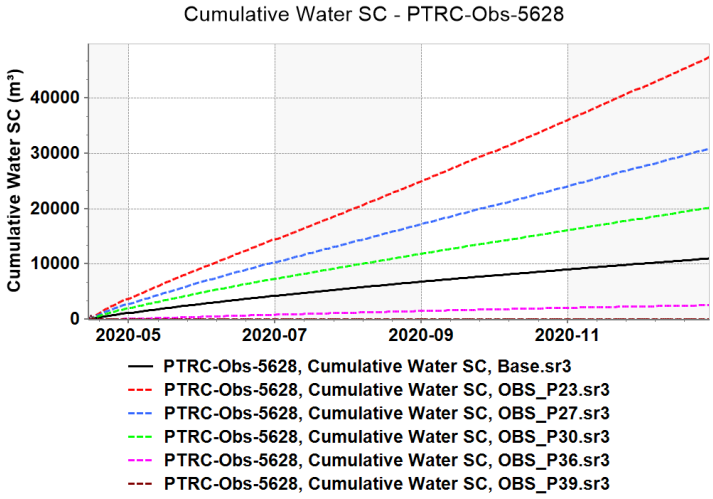
Cumulative Water SC - PTRC-Obs-5628
Cumulative Water SC (m³)
40000
30000
20000
10000
0
2020-05
2020-07
2020-09
2020-11
PTRC-Obs-5628, Cumulative Water SC, Base.sr3
PTRC-Obs-5628, Cumulative Water SC, OBS_P23.sr3
PTRC-Obs-5628, Cumulative Water SC, OBS_P27.sr3
PTRC-Obs-5628, Cumulative Water SC, OBS_P30.sr3
PTRC-Obs-5628, Cumulative Water SC, OBS_P36.sr3
PTRC-Obs-5628, Cumulative Water SC, OBS_P39.sr3

Plots related to perforation of the injector

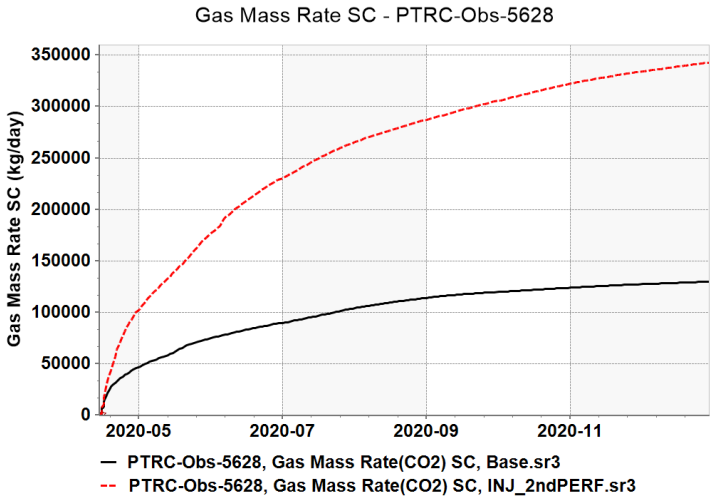

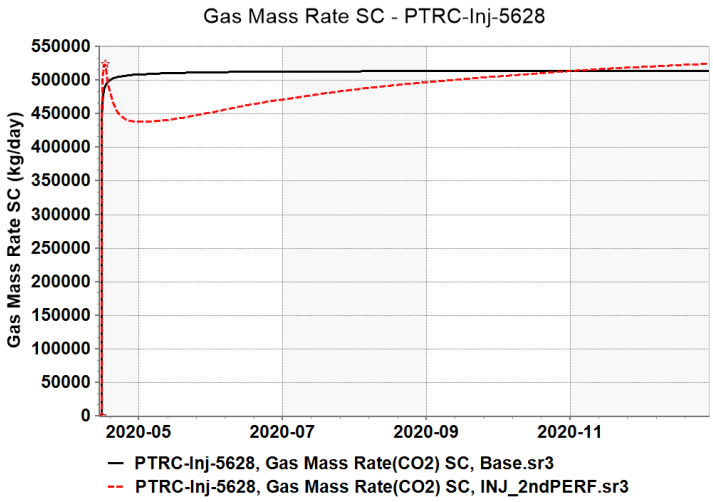

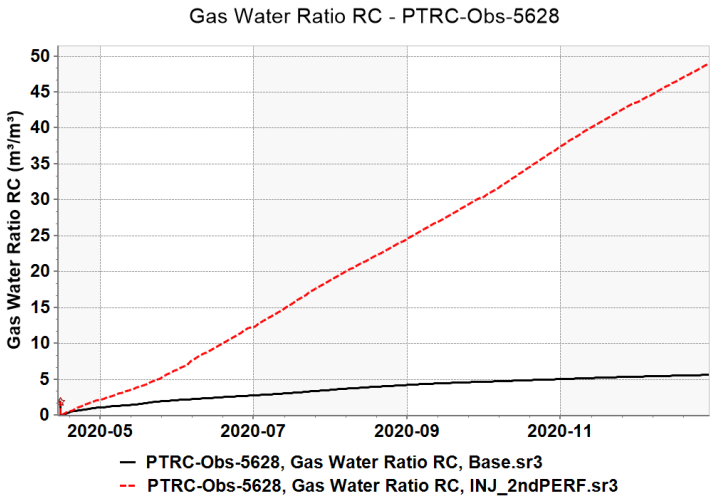

Gas Water Ratio SC - PTRC-Obs-5628

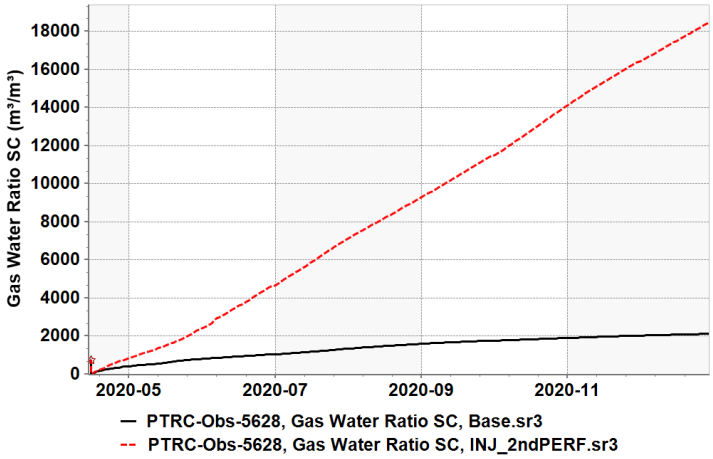

Well Bottom-hole Pressure - PTRC-Inj-5628,PTRC-Obs-5628

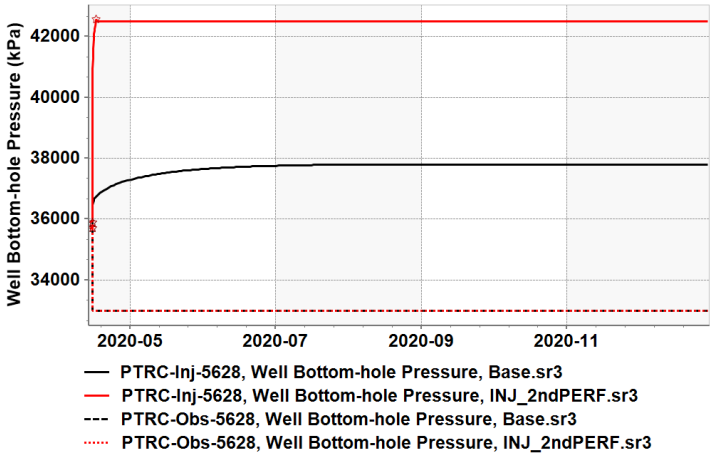

Cumulative Gas Mass SC - PTRC-Inj-5628

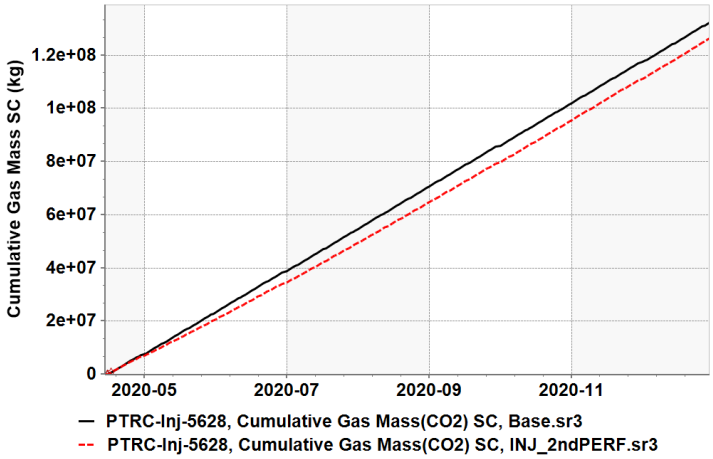

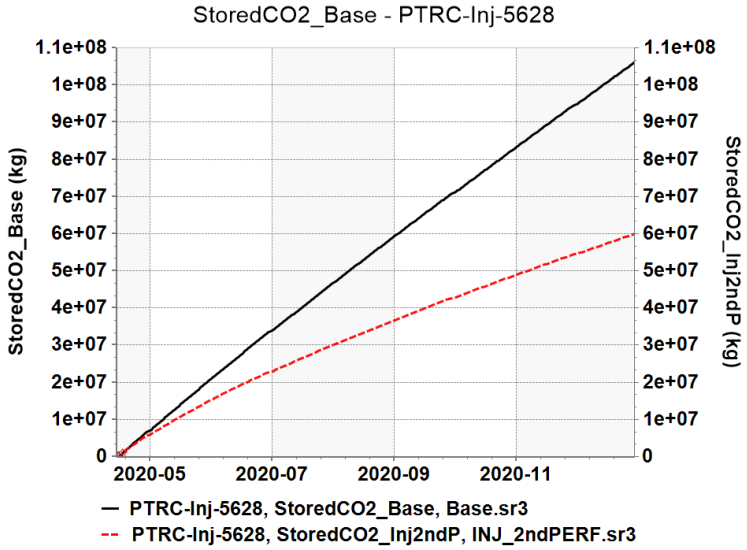
StoredCO2_Base - PTRC-Inj-5628
StoredCO2_Base (kg)
StoredCO2_Inj2ndP (kg)
1.1e+08
1e+08
9e+07
8e+07
7e+07
6e+07
5e+07
4e+07
3e+07
2e+07
1e+07
0
2020-05
2020-07
2020-09
2020-11
PTRC-Inj-5628, StoredCO2_Base, Base.sr3
PTRC-Inj-5628, StoredCO2_Inj2ndP, INJ_2ndPERF.sr3

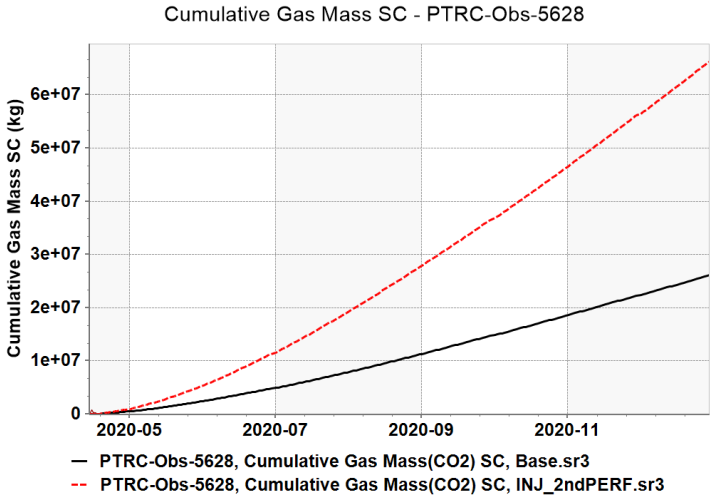
Cumulative Gas Mass SC - PTRC-Obs-5628
Cumulative Gas Mass SC (kg)
6e+07
5e+07
4e+07
3e+07
2e+07
1e+07
0
2020-05
2020-07
2020-09
2020-11
PTRC-Obs-5628, Cumulative Gas Mass(CO2) SC, Base.sr3
PTRC-Obs-5628, Cumulative Gas Mass(CO2) SC, INJ_2ndPERF.sr3

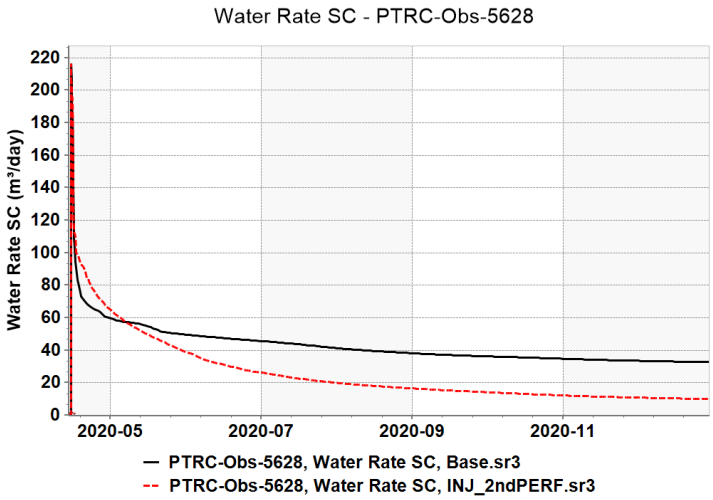
Water Rate SC - PTRC-Obs-5628
Water Rate SC (m³/day)
220
200
180
160
140
120
100
80
60
40
20
0
2020-05
2020-07
2020-09
2020-11
PTRC-Obs-5628, Water Rate SC, Base.sr3
PTRC-Obs-5628, Water Rate SC, INJ_2ndPERF.sr3

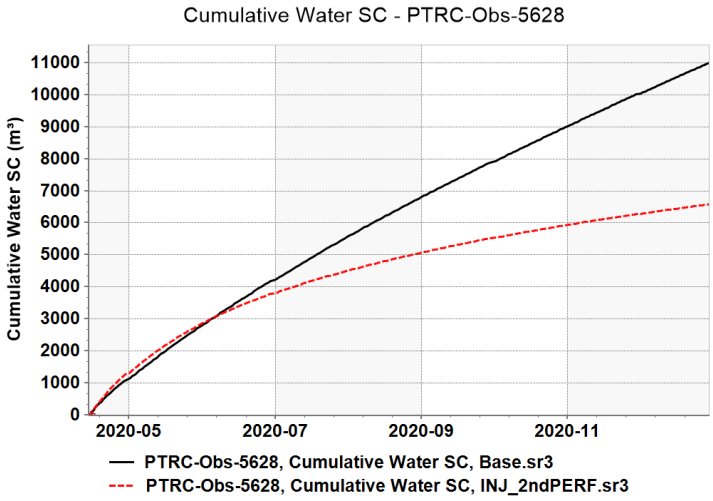
Cumulative Water SC - PTRC-Obs-5628
Cumulative Water SC (m³)
11000
10000
9000
8000
7000
6000
5000
4000
3000
2000
1000
0
2020-05
2020-07
2020-09
2020-11
PTRC-Obs-5628, Cumulative Water SC, Base.sr3
PTRC-Obs-5628, Cumulative Water SC, INJ_2ndPERF.sr3

Plots related to perforation of the producer

Gas Mass Rate SC - PTRC-Obs-5628

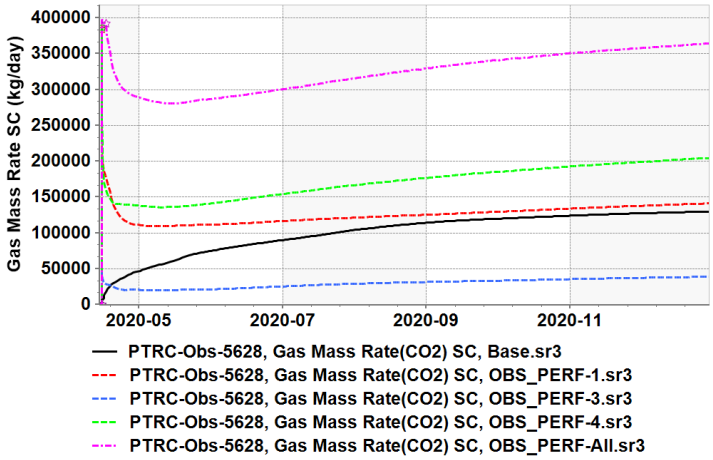

Gas Mass Rate SC - PTRC-Inj-5628,PTRC-Obs-5628

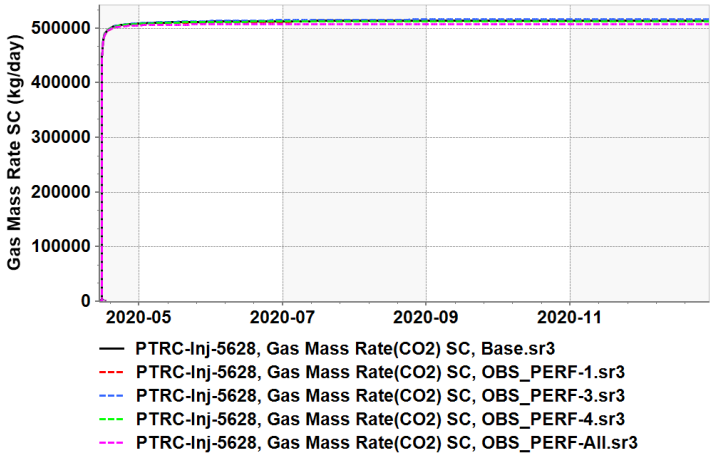

Gas Water Ratio RC - PTRC-Obs-5628

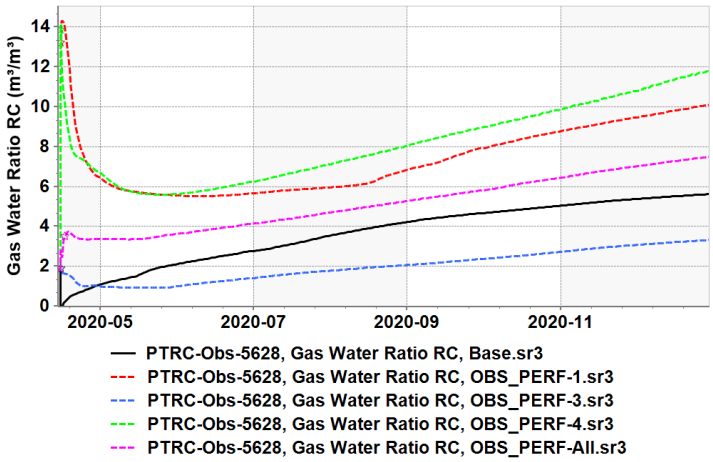

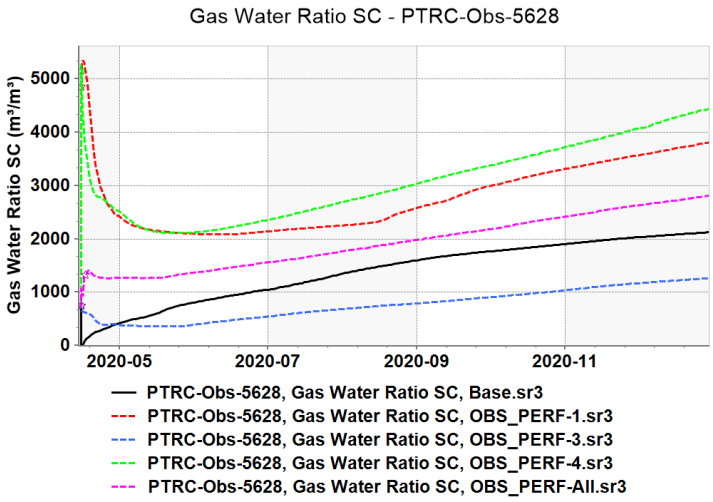
Gas Water Ratio SC - PTRC-Obs-5628
Gas Water Ratio SC (m³/m³)
5000
4000
3000
2000
1000
0
2020-05
2020-07
2020-09
2020-11
PTRC-Obs-5628, Gas Water Ratio SC, Base.sr3
PTRC-Obs-5628, Gas Water Ratio SC, OBS_PERF-1.sr3
PTRC-Obs-5628, Gas Water Ratio SC, OBS_PERF-3.sr3
PTRC-Obs-5628, Gas Water Ratio SC, OBS_PERF-4.sr3
PTRC-Obs-5628, Gas Water Ratio SC, OBS_PERF-All.sr3

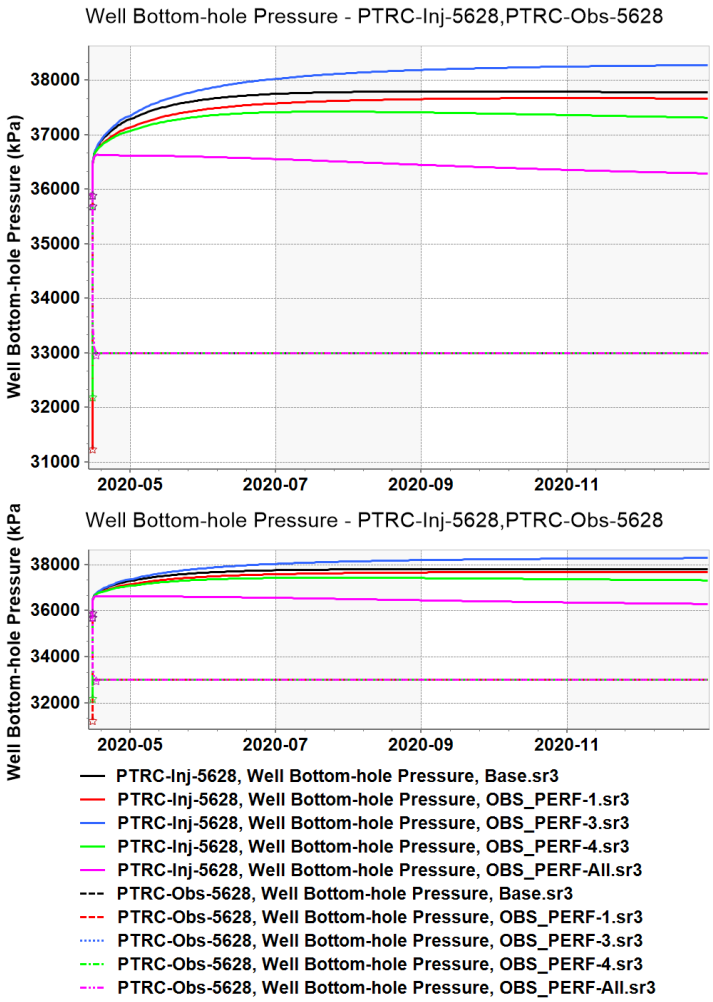
Well Bottom-hole Pressure - PTRC-Inj-5628,PTRC-Obs-5628
Well Bottom-hole Pressure (kPa)
38000
37000
36000
35000
34000
33000
32000
31000
2020-05
2020-07
2020-09
2020-11
Well Bottom-hole Pressure - PTRC-Inj-5628,PTRC-Obs-5628
Well Bottom-hole Pressure (kPa
38000
36000
34000
32000
2020-05
2020-07
2020-09
2020-11
PTRC-Inj-5628, Well Bottom-hole Pressure, Base.sr3
PTRC-Inj-5628, Well Bottom-hole Pressure, OBS_PERF-1.sr3
PTRC-Inj-5628, Well Bottom-hole Pressure, OBS_PERF-3.sr3
PTRC-Inj-5628, Well Bottom-hole Pressure, OBS_PERF-4.sr3
PTRC-Inj-5628, Well Bottom-hole Pressure, OBS_PERF-All.sr3
PTRC-Obs-5628, Well Bottom-hole Pressure, Base.sr3
PTRC-Obs-5628, Well Bottom-hole Pressure, OBS_PERF-1.sr3
PTRC-Obs-5628, Well Bottom-hole Pressure, OBS_PERF-3.sr3
PTRC-Obs-5628, Well Bottom-hole Pressure, OBS_PERF-4.sr3
PTRC-Obs-5628, Well Bottom-hole Pressure, OBS_PERF-All.sr3

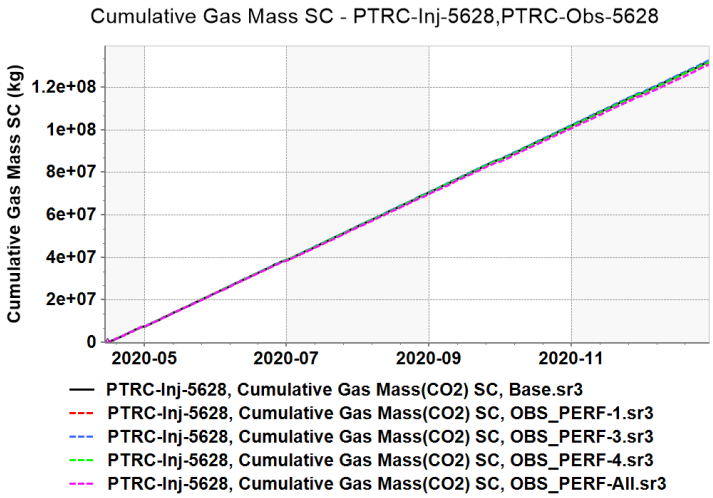
Cumulative Gas Mass SC - PTRC-Inj-5628,PTRC-Obs-5628
Cumulative Gas Mass SC (kg)
1.2e+08
1e+08
8e+07
6e+07
4e+07
2e+07
0
2020-05
2020-07
2020-09
2020-11
PTRC-Inj-5628, Cumulative Gas Mass(CO2) SC, Base.sr3
PTRC-Inj-5628, Cumulative Gas Mass(CO2) SC, OBS_PERF-1.sr3
PTRC-Inj-5628, Cumulative Gas Mass(CO2) SC, OBS_PERF-3.sr3
PTRC-Inj-5628, Cumulative Gas Mass(CO2) SC, OBS_PERF-4.sr3
PTRC-Inj-5628, Cumulative Gas Mass(CO2) SC, OBS_PERF-All.sr3

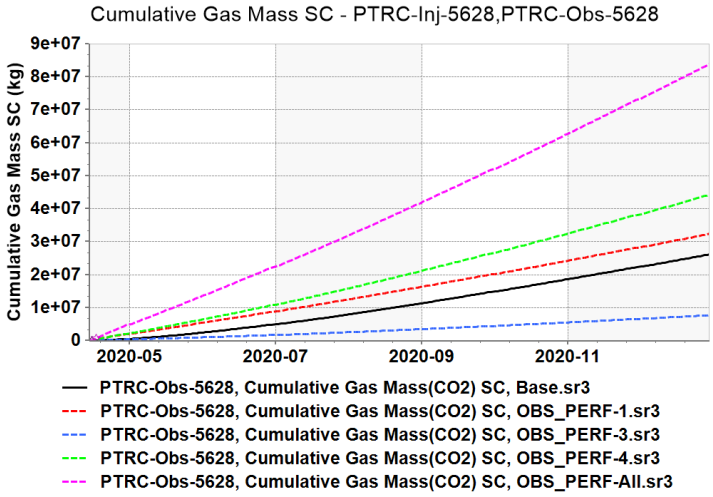
Cumulative Gas Mass SC - PTRC-Inj-5628,PTRC-Obs-5628
Cumulative Gas Mass SC (kg)
9e+07
8e+07
7e+07
6e+07
5e+07
4e+07
3e+07
2e+07
1e+07
0
2020-05
2020-07
2020-09
2020-11
PTRC-Obs-5628, Cumulative Gas Mass(CO2) SC, Base.sr3
PTRC-Obs-5628, Cumulative Gas Mass(CO2) SC, OBS_PERF-1.sr3
PTRC-Obs-5628, Cumulative Gas Mass(CO2) SC, OBS_PERF-3.sr3
PTRC-Obs-5628, Cumulative Gas Mass(CO2) SC, OBS_PERF-4.sr3
PTRC-Obs-5628, Cumulative Gas Mass(CO2) SC, OBS_PERF-All.sr3

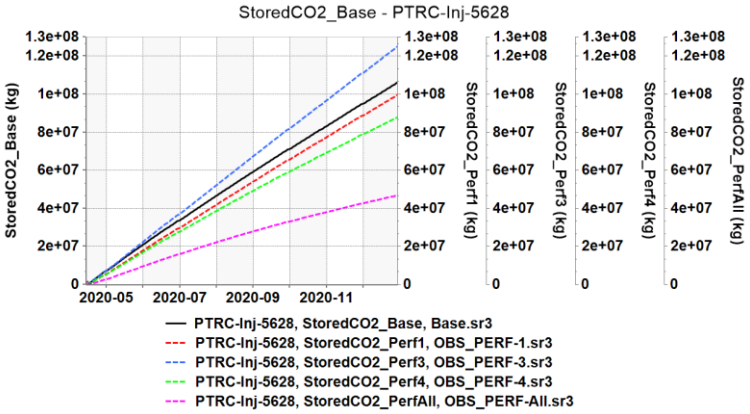
StoredCO2_Base - PTRC-Inj-5628
StoredCO2_Base (kg)
StoredCO2_Perf1 (kg)
StoredCO2_Perf3 (kg)
StoredCO2_Perf4 (kg)
StoredCO2_PerfAll (kg)
1.3e+08
1.2e+08
1e+08
8e+07
6e+07
4e+07
2e+07
0
2020-05
2020-07
2020-09
2020-11
PTRC-Inj-5628, StoredCO2_Base, Base.sr3
PTRC-Inj-5628, StoredCO2_Perf1, OBS_PERF-1.sr3
PTRC-Inj-5628, StoredCO2_Perf3, OBS_PERF-3.sr3
PTRC-Inj-5628, StoredCO2_Perf4, OBS_PERF-4.sr3
PTRC-Inj-5628, StoredCO2_PerfAll, OBS_PERF-All.sr3

Water Rate SC - PTRC-Obs-5628

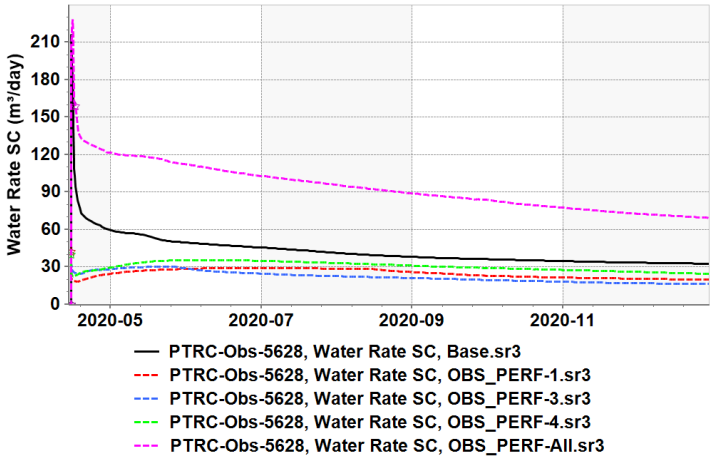

Cumulative Water SC - PTRC-Obs-5628

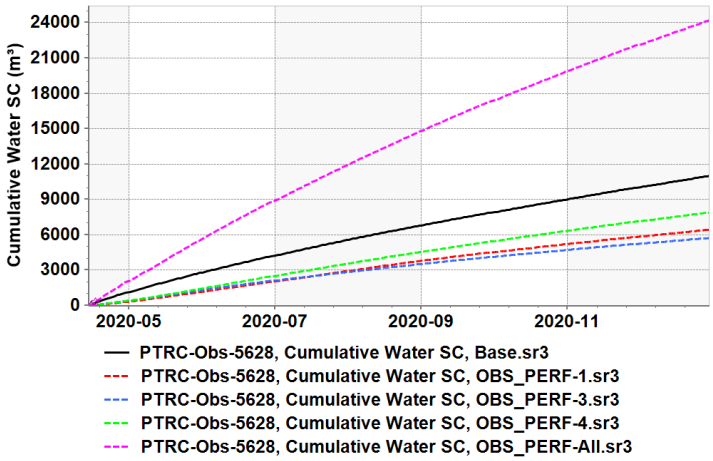

Gas Mass Rate SC - PTRC-Inj-5628,PTRC-Obs-5628

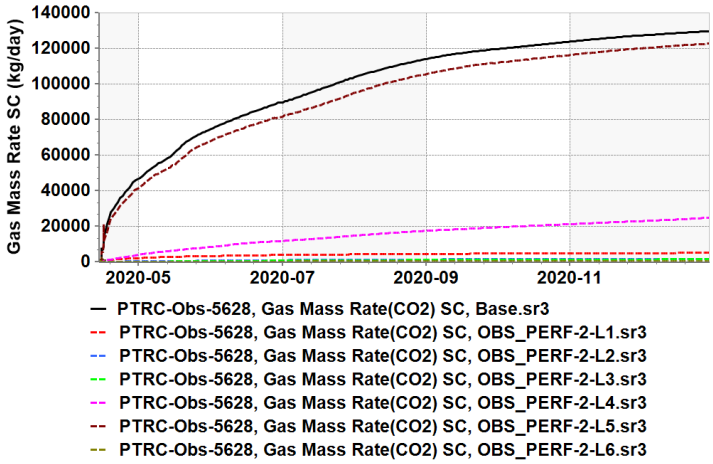

Gas Mass Rate SC - PTRC-Inj-5628,PTRC-Obs-5628

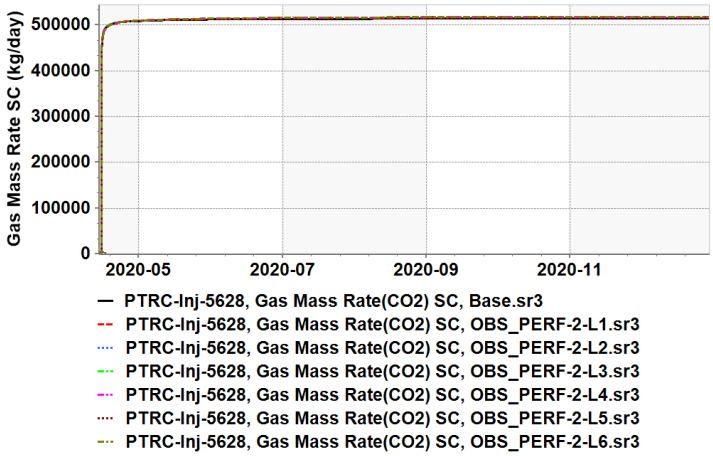

PTRC-Inj-5628, Gas Mass Rate(CO2) SC, Base.sr3
PTRC-Inj-5628, Gas Mass Rate(CO2) SC, OBS_PERF-2-L1.sr3
PTRC-Inj-5628, Gas Mass Rate(CO2) SC, OBS_PERF-2-L2.sr3
PTRC-Inj-5628, Gas Mass Rate(CO2) SC, OBS_PERF-2-L3.sr3
PTRC-Inj-5628, Gas Mass Rate(CO2) SC, OBS_PERF-2-L4.sr3
PTRC-Inj-5628, Gas Mass Rate(CO2) SC, OBS_PERF-2-L5.sr3
PTRC-Inj-5628, Gas Mass Rate(CO2) SC, OBS_PERF-2-L6.sr3

Gas Water Ratio RC - PTRC-Obs-5628

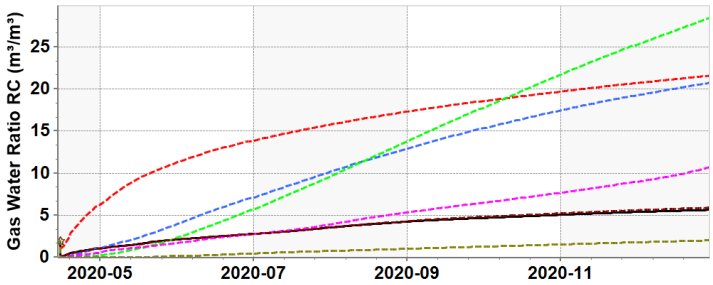

PTRC-Obs-5628, Gas Water Ratio RC, Base.sr3
PTRC-Obs-5628, Gas Water Ratio RC, OBS_PERF-2-L1.sr3
PTRC-Obs-5628, Gas Water Ratio RC, OBS_PERF-2-L2.sr3
PTRC-Obs-5628, Gas Water Ratio RC, OBS_PERF-2-L3.sr3
PTRC-Obs-5628, Gas Water Ratio RC, OBS_PERF-2-L4.sr3
PTRC-Obs-5628, Gas Water Ratio RC, OBS_PERF-2-L5.sr3
PTRC-Obs-5628, Gas Water Ratio RC, OBS_PERF-2-L6.sr3

Gas Water Ratio SC - PTRC-Obs-5628

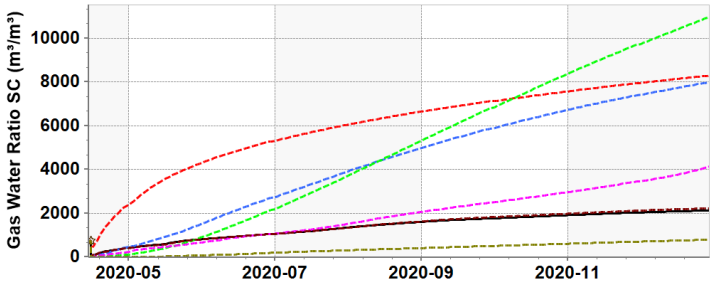

PTRC-Obs-5628, Gas Water Ratio SC, Base.sr3
PTRC-Obs-5628, Gas Water Ratio SC, OBS_PERF-2-L1.sr3
PTRC-Obs-5628, Gas Water Ratio SC, OBS_PERF-2-L2.sr3
PTRC-Obs-5628, Gas Water Ratio SC, OBS_PERF-2-L3.sr3
PTRC-Obs-5628, Gas Water Ratio SC, OBS_PERF-2-L4.sr3
PTRC-Obs-5628, Gas Water Ratio SC, OBS_PERF-2-L5.sr3
PTRC-Obs-5628, Gas Water Ratio SC, OBS_PERF-2-L6.sr3

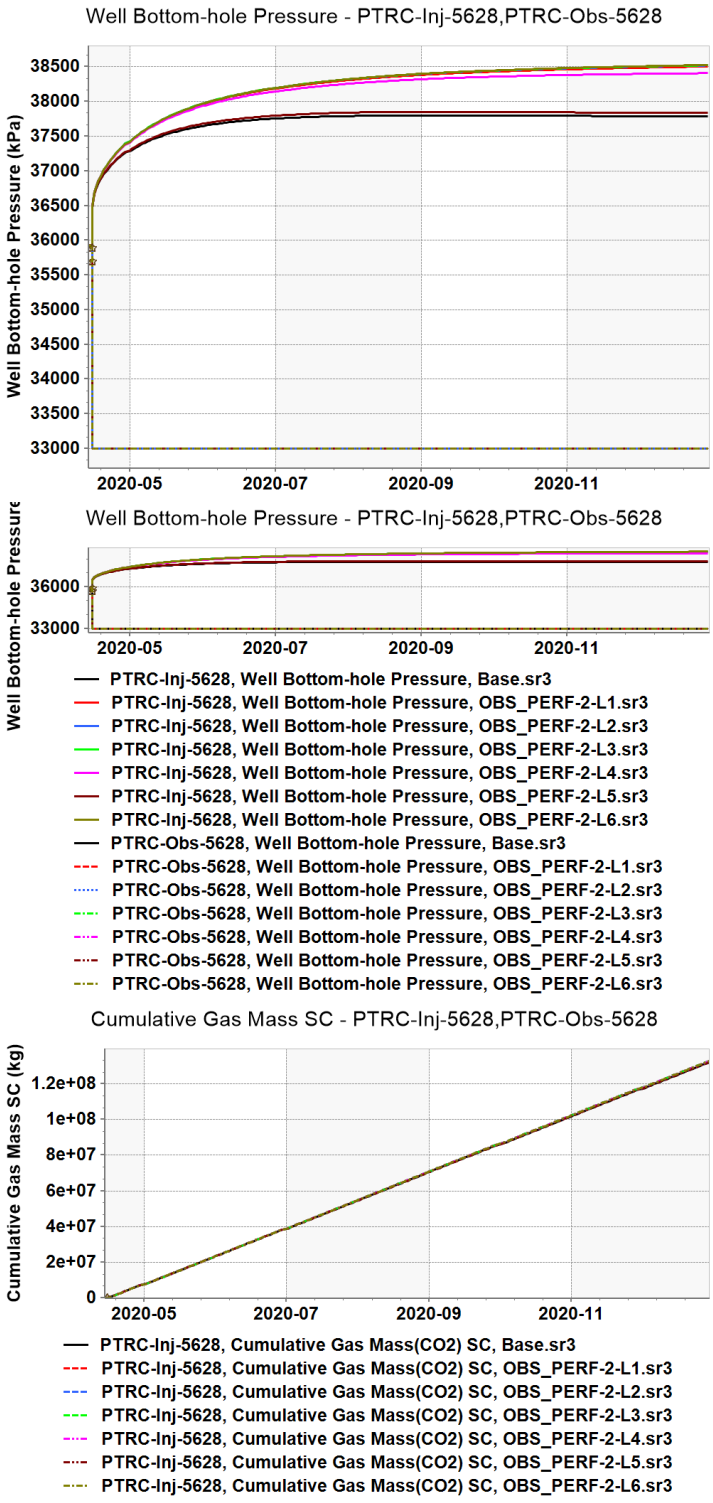
Well Bottom-hole Pressure - PTRC-Inj-5628,PTRC-Obs-5628
Well Bottom-hole Pressure (kPa)
38500
38000
37500
37000
36500
36000
35500
35000
34500
34000
33500
33000
2020-05
2020-07
2020-09
2020-11
Well Bottom-hole Pressure - PTRC-Inj-5628,PTRC-Obs-5628
Well Bottom-hole Pressure
36000
33000
2020-05
2020-07
2020-09
2020-11
PTRC-Inj-5628, Well Bottom-hole Pressure, Base.sr3
PTRC-Inj-5628, Well Bottom-hole Pressure, OBS_PERF-2-L1.sr3
PTRC-Inj-5628, Well Bottom-hole Pressure, OBS_PERF-2-L2.sr3
PTRC-Inj-5628, Well Bottom-hole Pressure, OBS_PERF-2-L3.sr3
PTRC-Inj-5628, Well Bottom-hole Pressure, OBS_PERF-2-L4.sr3
PTRC-Inj-5628, Well Bottom-hole Pressure, OBS_PERF-2-L5.sr3
PTRC-Inj-5628, Well Bottom-hole Pressure, OBS_PERF-2-L6.sr3
PTRC-Obs-5628, Well Bottom-hole Pressure, Base.sr3
PTRC-Obs-5628, Well Bottom-hole Pressure, OBS_PERF-2-L1.sr3
PTRC-Obs-5628, Well Bottom-hole Pressure, OBS_PERF-2-L2.sr3
PTRC-Obs-5628, Well Bottom-hole Pressure, OBS_PERF-2-L3.sr3
PTRC-Obs-5628, Well Bottom-hole Pressure, OBS_PERF-2-L4.sr3
PTRC-Obs-5628, Well Bottom-hole Pressure, OBS_PERF-2-L5.sr3
PTRC-Obs-5628, Well Bottom-hole Pressure, OBS_PERF-2-L6.sr3
Cumulative Gas Mass SC - PTRC-Inj-5628,PTRC-Obs-5628
Cumulative Gas Mass SC (kg)
1.2e+08
1e+08
8e+07
6e+07
4e+07
2e+07
0
2020-05
2020-07
2020-09
2020-11
PTRC-Inj-5628, Cumulative Gas Mass(CO2) SC, Base.sr3
PTRC-Inj-5628, Cumulative Gas Mass(CO2) SC, OBS_PERF-2-L1.sr3
PTRC-Inj-5628, Cumulative Gas Mass(CO2) SC, OBS_PERF-2-L2.sr3
PTRC-Inj-5628, Cumulative Gas Mass(CO2) SC, OBS_PERF-2-L3.sr3
PTRC-Inj-5628, Cumulative Gas Mass(CO2) SC, OBS_PERF-2-L4.sr3
PTRC-Inj-5628, Cumulative Gas Mass(CO2) SC, OBS_PERF-2-L5.sr3
PTRC-Inj-5628, Cumulative Gas Mass(CO2) SC, OBS_PERF-2-L6.sr3

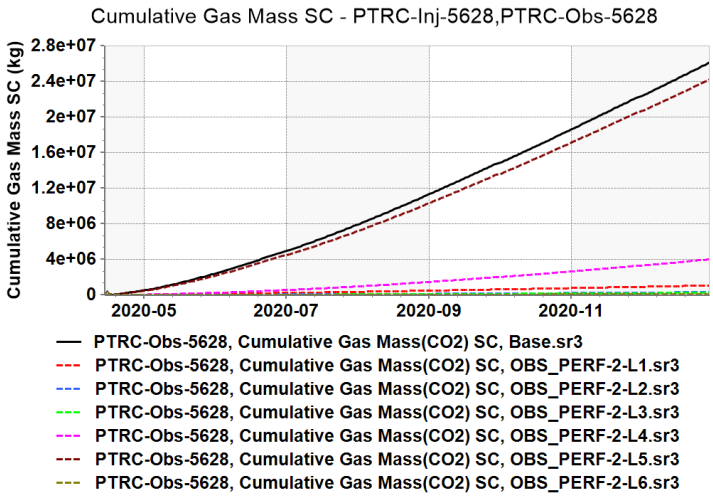
Cumulative Gas Mass SC - PTRC-Inj-5628,PTRC-Obs-5628
Cumulative Gas Mass SC (kg)
2.8e+07
2.4e+07
2e+07
1.6e+07
1.2e+07
8e+06
4e+06
0
2020-05
2020-07
2020-09
2020-11
PTRC-Obs-5628, Cumulative Gas Mass(CO2) SC, Base.sr3
PTRC-Obs-5628, Cumulative Gas Mass(CO2) SC, OBS_PERF-2-L1.sr3
PTRC-Obs-5628, Cumulative Gas Mass(CO2) SC, OBS_PERF-2-L2.sr3
PTRC-Obs-5628, Cumulative Gas Mass(CO2) SC, OBS_PERF-2-L3.sr3
PTRC-Obs-5628, Cumulative Gas Mass(CO2) SC, OBS_PERF-2-L4.sr3
PTRC-Obs-5628, Cumulative Gas Mass(CO2) SC, OBS_PERF-2-L5.sr3
PTRC-Obs-5628, Cumulative Gas Mass(CO2) SC, OBS_PERF-2-L6.sr3

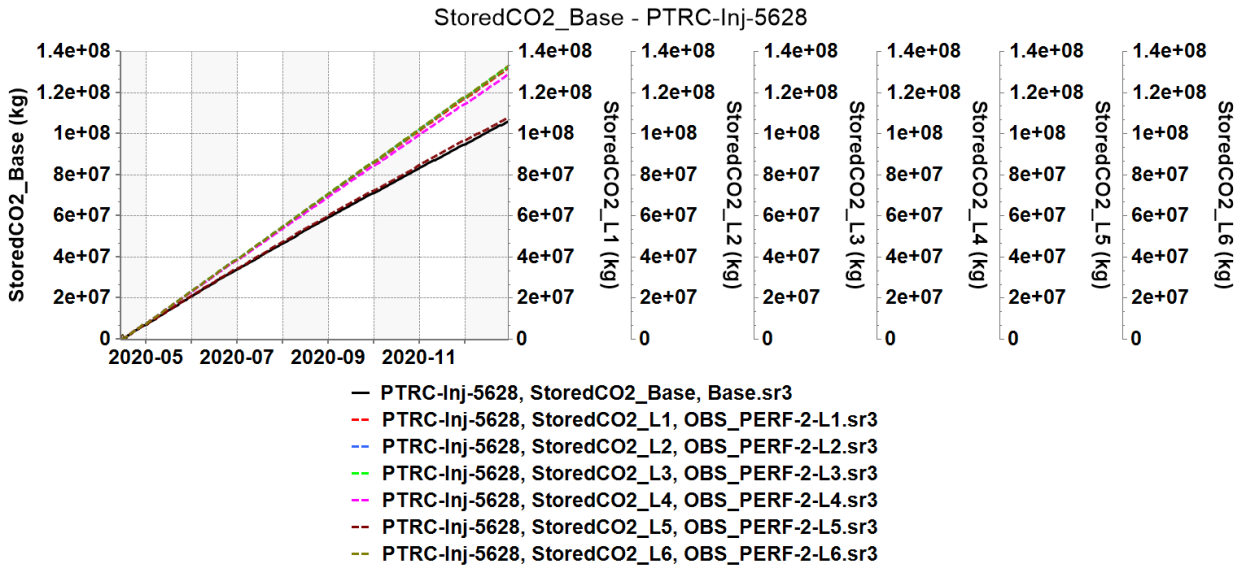
StoredCO2_Base - PTRC-Inj-5628
StoredCO2_Base (kg)
1.4e+08
1.2e+08
1e+08
8e+07
6e+07
4e+07
2e+07
0
2020-05
2020-07
2020-09
2020-11
StoredCO2_L1 (kg)
StoredCO2_L2 (kg)
StoredCO2_L3 (kg)
StoredCO2_L4 (kg)
StoredCO2_L5 (kg)
StoredCO2_L6 (kg)
PTRC-Inj-5628, StoredCO2_Base, Base.sr3
PTRC-Inj-5628, StoredCO2_L1, OBS_PERF-2-L1.sr3
PTRC-Inj-5628, StoredCO2_L2, OBS_PERF-2-L2.sr3
PTRC-Inj-5628, StoredCO2_L3, OBS_PERF-2-L3.sr3
PTRC-Inj-5628, StoredCO2_L4, OBS_PERF-2-L4.sr3
PTRC-Inj-5628, StoredCO2_L5, OBS_PERF-2-L5.sr3
PTRC-Inj-5628, StoredCO2_L6, OBS_PERF-2-L6.sr3

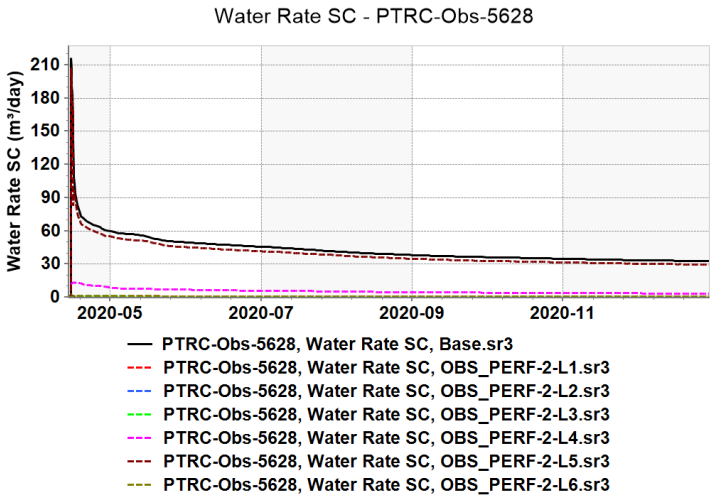
Water Rate SC - PTRC-Obs-5628
Water Rate SC (m³/day)
210
180
150
120
90
60
30
0
2020-05
2020-07
2020-09
2020-11
PTRC-Obs-5628, Water Rate SC, Base.sr3
PTRC-Obs-5628, Water Rate SC, OBS_PERF-2-L1.sr3
PTRC-Obs-5628, Water Rate SC, OBS_PERF-2-L2.sr3
PTRC-Obs-5628, Water Rate SC, OBS_PERF-2-L3.sr3
PTRC-Obs-5628, Water Rate SC, OBS_PERF-2-L4.sr3
PTRC-Obs-5628, Water Rate SC, OBS_PERF-2-L5.sr3
PTRC-Obs-5628, Water Rate SC, OBS_PERF-2-L6.sr3

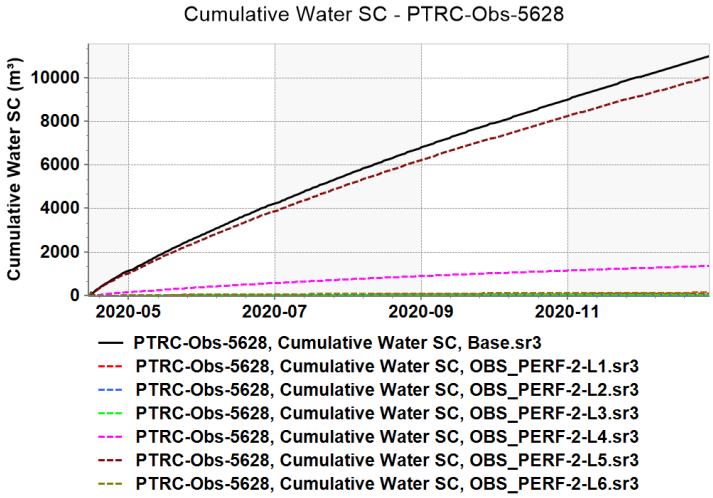
Cumulative Water SC - PTRC-Obs-5628
Cumulative Water SC (m³)
10000
8000
6000
4000
2000
0
2020-05
2020-07
2020-09
2020-11
PTRC-Obs-5628, Cumulative Water SC, Base.sr3
PTRC-Obs-5628, Cumulative Water SC, OBS_PERF-2-L1.sr3
PTRC-Obs-5628, Cumulative Water SC, OBS_PERF-2-L2.sr3
PTRC-Obs-5628, Cumulative Water SC, OBS_PERF-2-L3.sr3
PTRC-Obs-5628, Cumulative Water SC, OBS_PERF-2-L4.sr3
PTRC-Obs-5628, Cumulative Water SC, OBS_PERF-2-L5.sr3
PTRC-Obs-5628, Cumulative Water SC, OBS_PERF-2-L6.sr3

Plots related to skin factor of the producer

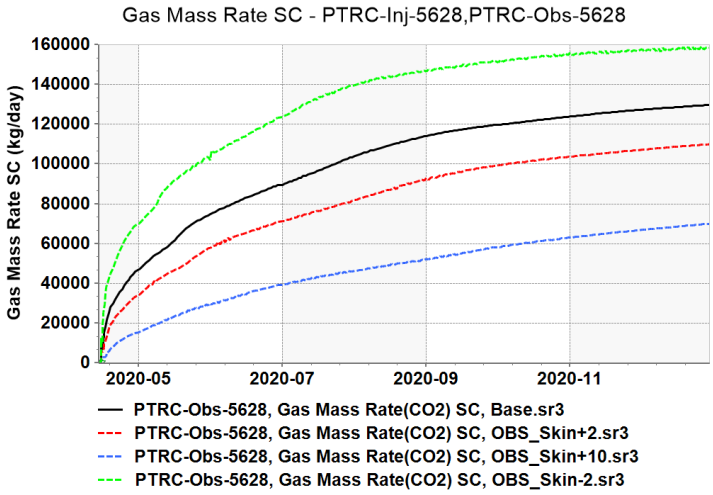

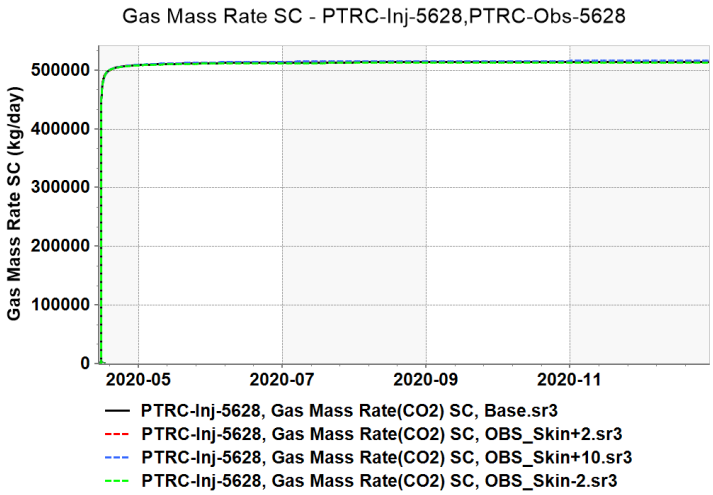

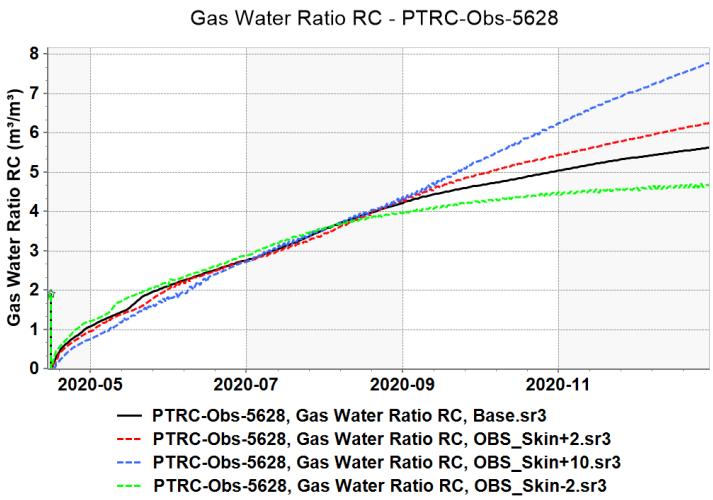

Gas Water Ratio SC - PTRC-Obs-5628

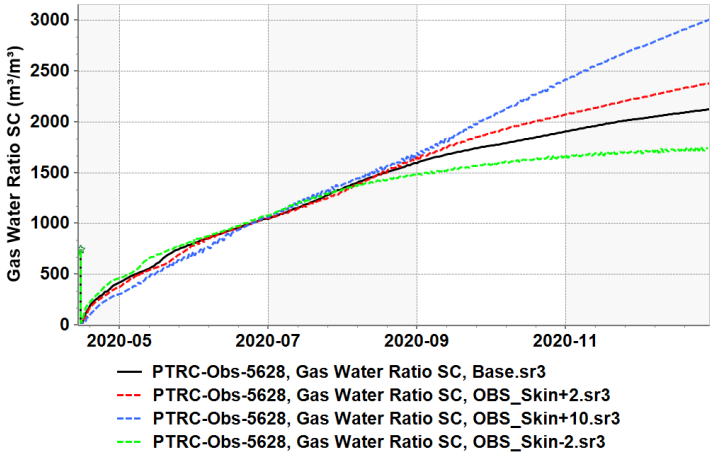

Well Bottom-hole Pressure - PTRC-Inj-5628,PTRC-Obs-5628

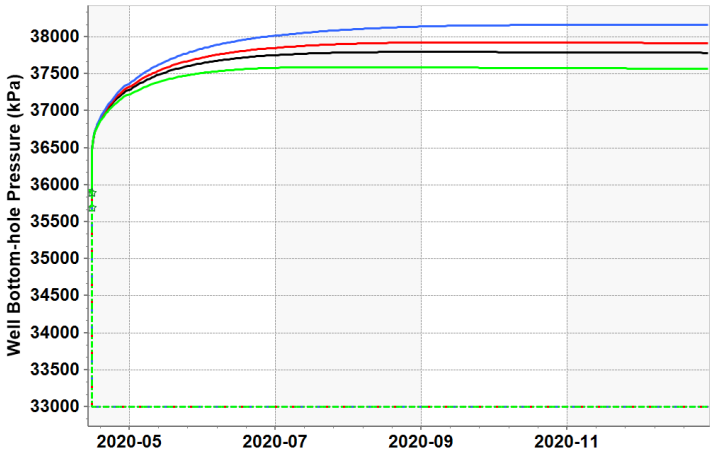

Well Bottom-hole Pressure - PTRC-Inj-5628,PTRC-Obs-5628

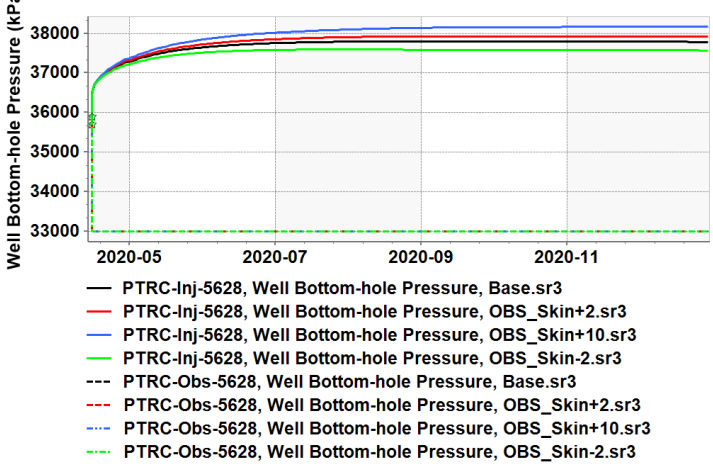

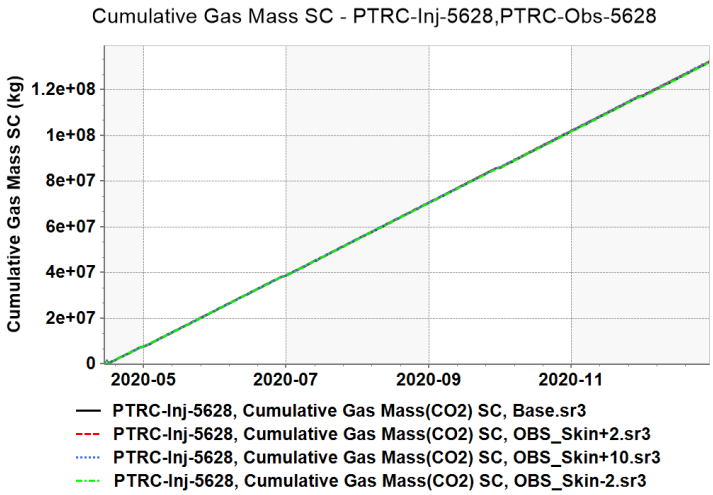
Cumulative Gas Mass SC - PTRC-Inj-5628,PTRC-Obs-5628
Cumulative Gas Mass SC (kg)
1.2e+08
1e+08
8e+07
6e+07
4e+07
2e+07
0
2020-05
2020-07
2020-09
2020-11
PTRC-Inj-5628, Cumulative Gas Mass(CO2) SC, Base.sr3
PTRC-Inj-5628, Cumulative Gas Mass(CO2) SC, OBS_Skin+2.sr3
PTRC-Inj-5628, Cumulative Gas Mass(CO2) SC, OBS_Skin+10.sr3
PTRC-Inj-5628, Cumulative Gas Mass(CO2) SC, OBS_Skin-2.sr3

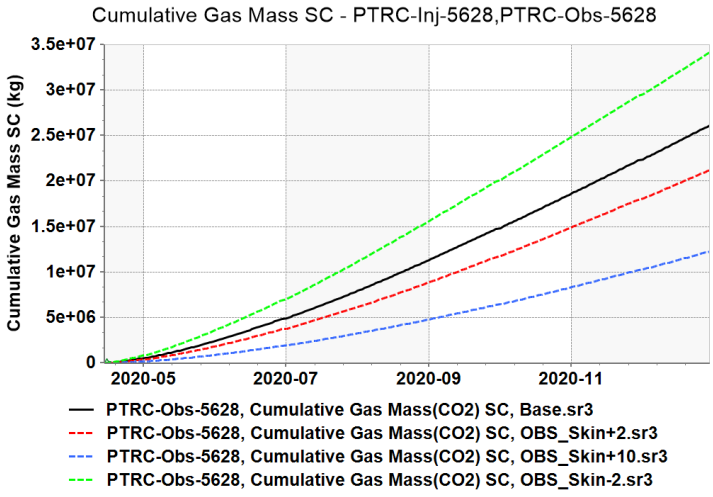
Cumulative Gas Mass SC - PTRC-Inj-5628,PTRC-Obs-5628
Cumulative Gas Mass SC (kg)
3.5e+07
3e+07
2.5e+07
2e+07
1.5e+07
1e+07
5e+06
0
2020-05
2020-07
2020-09
2020-11
PTRC-Obs-5628, Cumulative Gas Mass(CO2) SC, Base.sr3
PTRC-Obs-5628, Cumulative Gas Mass(CO2) SC, OBS_Skin+2.sr3
PTRC-Obs-5628, Cumulative Gas Mass(CO2) SC, OBS_Skin+10.sr3
PTRC-Obs-5628, Cumulative Gas Mass(CO2) SC, OBS_Skin-2.sr3

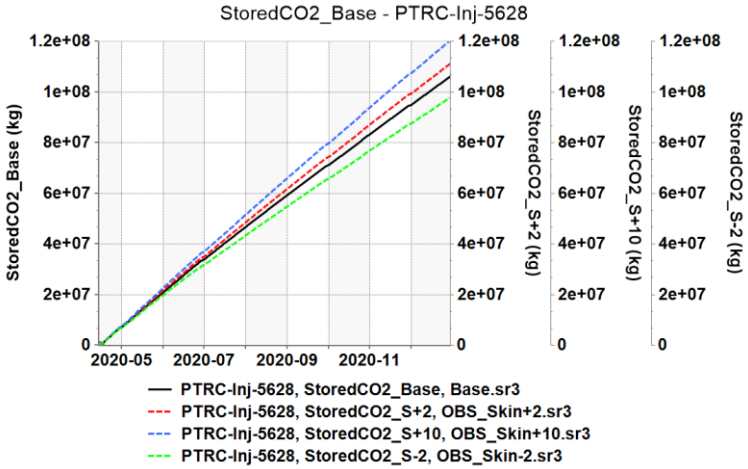
StoredCO2_Base - PTRC-Inj-5628
StoredCO2_Base (kg)
StoredCO2_S+2 (kg)
StoredCO2_S+10 (kg)
StoredCO2_S-2 (kg)
1.2e+08
1e+08
8e+07
6e+07
4e+07
2e+07
0
2020-05
2020-07
2020-09
2020-11
PTRC-Inj-5628, StoredCO2_Base, Base.sr3
PTRC-Inj-5628, StoredCO2_S+2, OBS_Skin+2.sr3
PTRC-Inj-5628, StoredCO2_S+10, OBS_Skin+10.sr3
PTRC-Inj-5628, StoredCO2_S-2, OBS_Skin-2.sr3

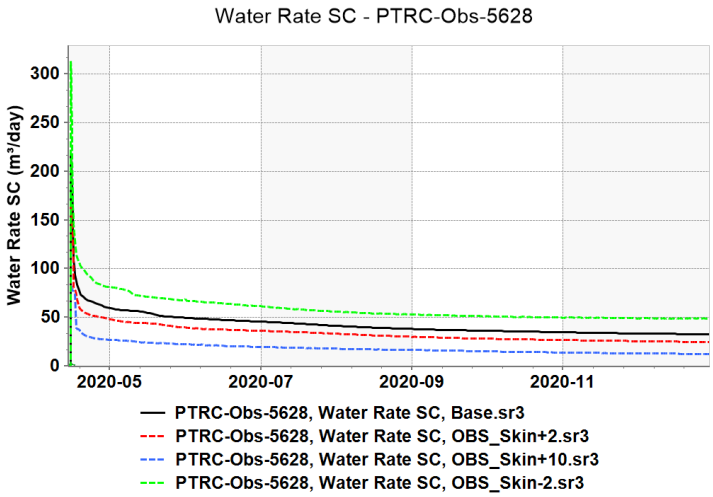
Water Rate SC - PTRC-Obs-5628
Water Rate SC (m³/day)
300
250
200
150
100
50
0
2020-05
2020-07
2020-09
2020-11
PTRC-Obs-5628, Water Rate SC, Base.sr3
PTRC-Obs-5628, Water Rate SC, OBS_Skin+2.sr3
PTRC-Obs-5628, Water Rate SC, OBS_Skin+10.sr3
PTRC-Obs-5628, Water Rate SC, OBS_Skin-2.sr3

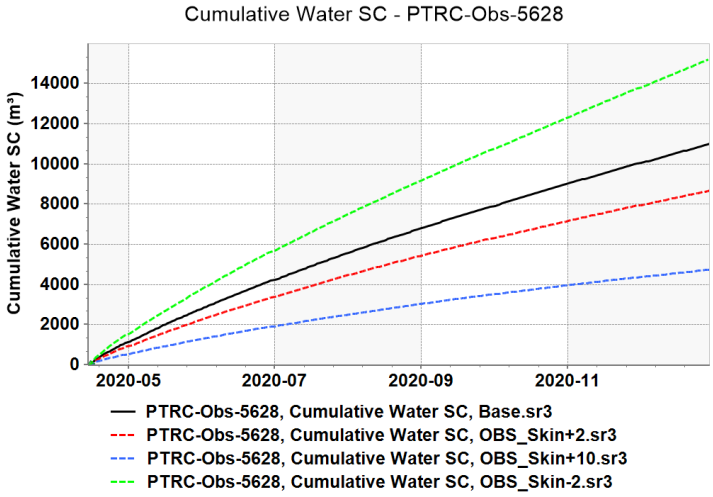
Cumulative Water SC - PTRC-Obs-5628
Cumulative Water SC (m³)
14000
12000
10000
8000
6000
4000
2000
0
2020-05
2020-07
2020-09
2020-11
PTRC-Obs-5628, Cumulative Water SC, Base.sr3
PTRC-Obs-5628, Cumulative Water SC, OBS_Skin+2.sr3
PTRC-Obs-5628, Cumulative Water SC, OBS_Skin+10.sr3
PTRC-Obs-5628, Cumulative Water SC, OBS_Skin-2.sr3

Plots related to production rate

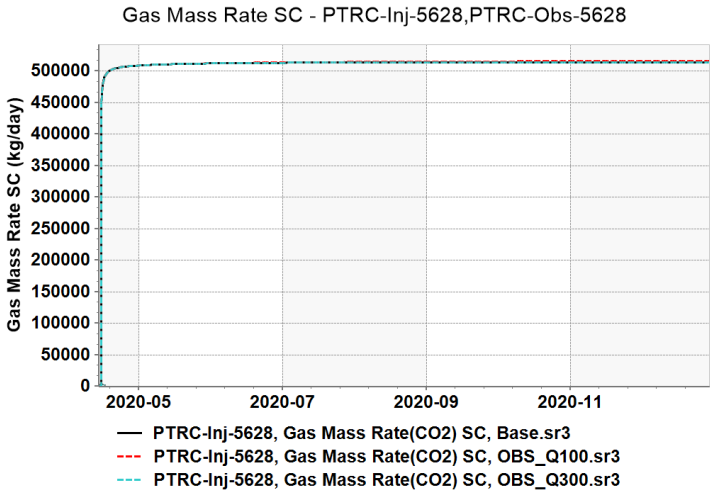

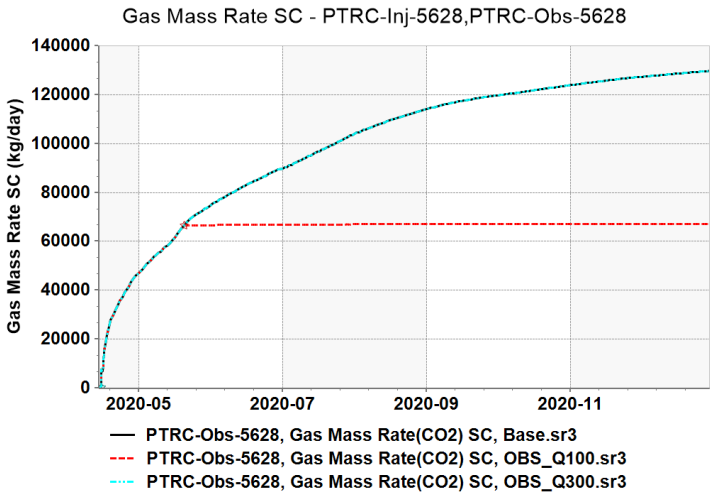

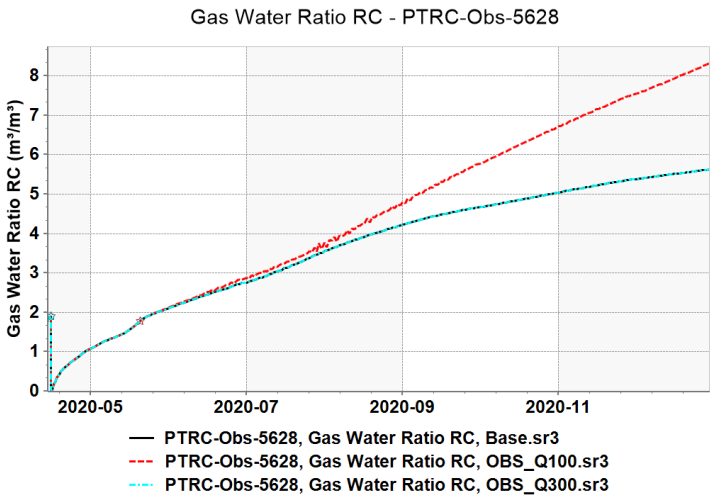

Gas Water Ratio SC - PTRC-Obs-5628

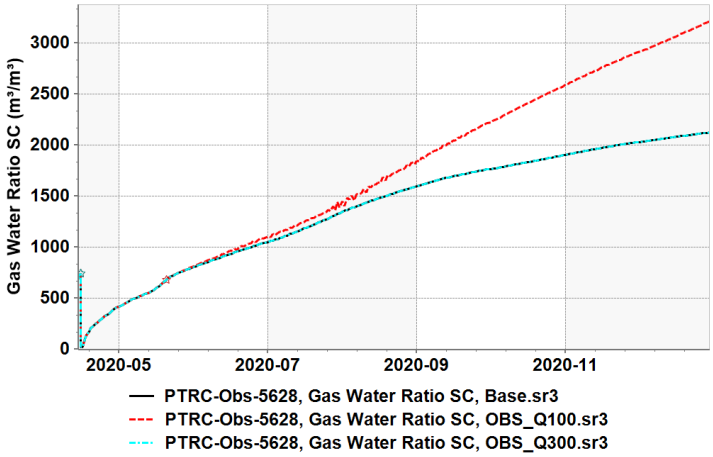

Well Bottom-hole Pressure - PTRC-Inj-5628,PTRC-Obs-5628

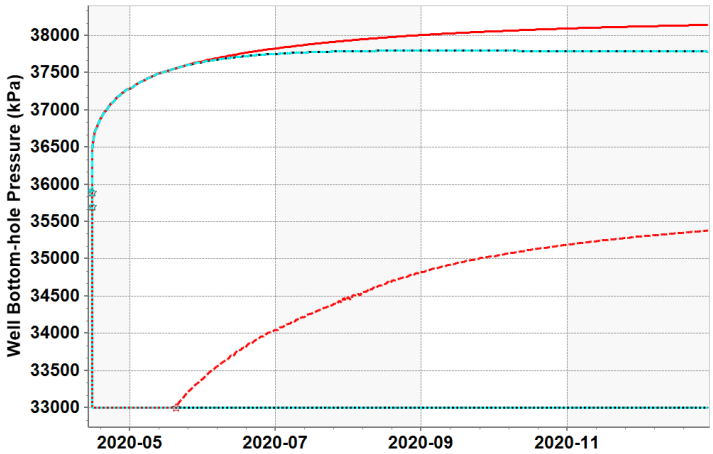

Well Bottom-hole Pressure - PTRC-Inj-5628,PTRC-Obs-5628

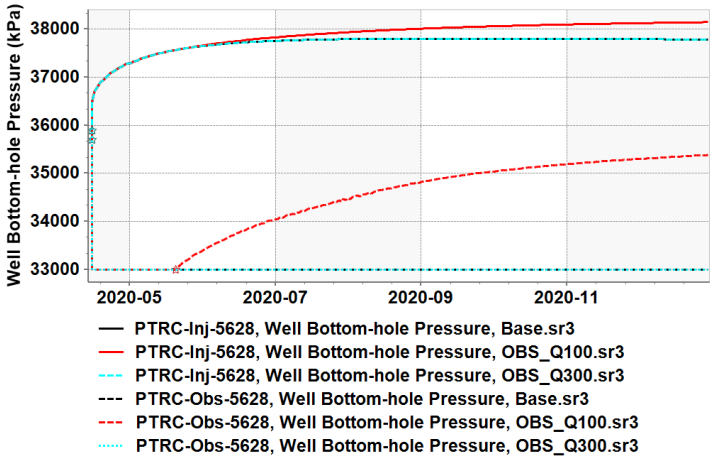

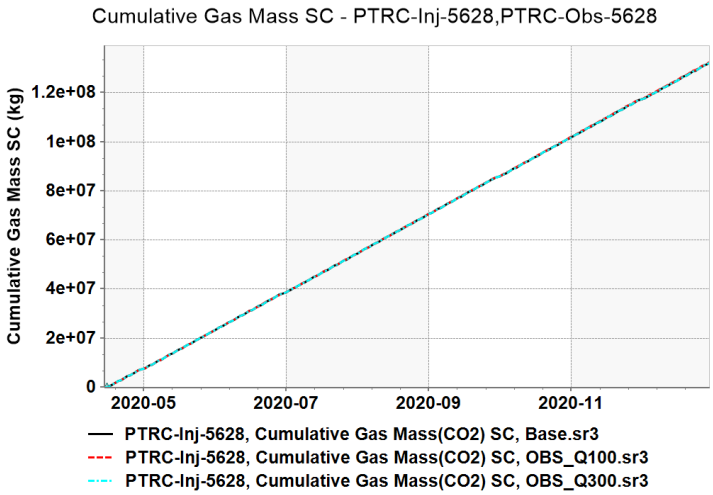
Cumulative Gas Mass SC - PTRC-Inj-5628,PTRC-Obs-5628
Cumulative Gas Mass SC (kg)
1.2e+08
1e+08
8e+07
6e+07
4e+07
2e+07
0
2020-05
2020-07
2020-09
2020-11
PTRC-Inj-5628, Cumulative Gas Mass(CO2) SC, Base.sr3
PTRC-Inj-5628, Cumulative Gas Mass(CO2) SC, OBS_Q100.sr3
PTRC-Inj-5628, Cumulative Gas Mass(CO2) SC, OBS_Q300.sr3

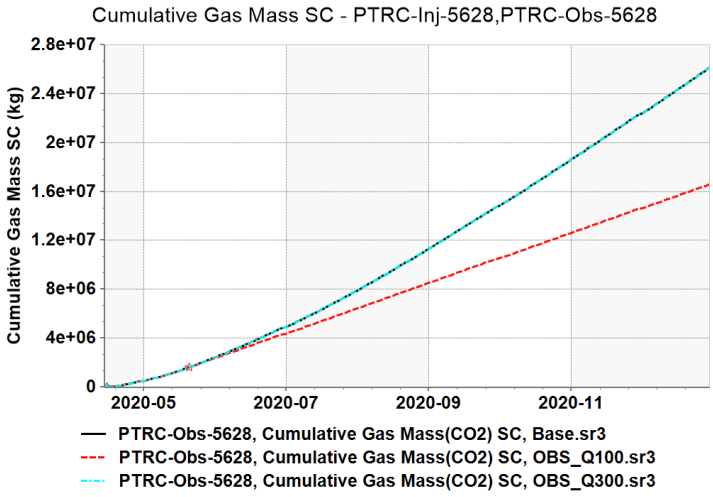
Cumulative Gas Mass SC - PTRC-Inj-5628,PTRC-Obs-5628
Cumulative Gas Mass SC (kg)
2.8e+07
2.4e+07
2e+07
1.6e+07
1.2e+07
8e+06
4e+06
0
2020-05
2020-07
2020-09
2020-11
PTRC-Obs-5628, Cumulative Gas Mass(CO2) SC, Base.sr3
PTRC-Obs-5628, Cumulative Gas Mass(CO2) SC, OBS_Q100.sr3
PTRC-Obs-5628, Cumulative Gas Mass(CO2) SC, OBS_Q300.sr3

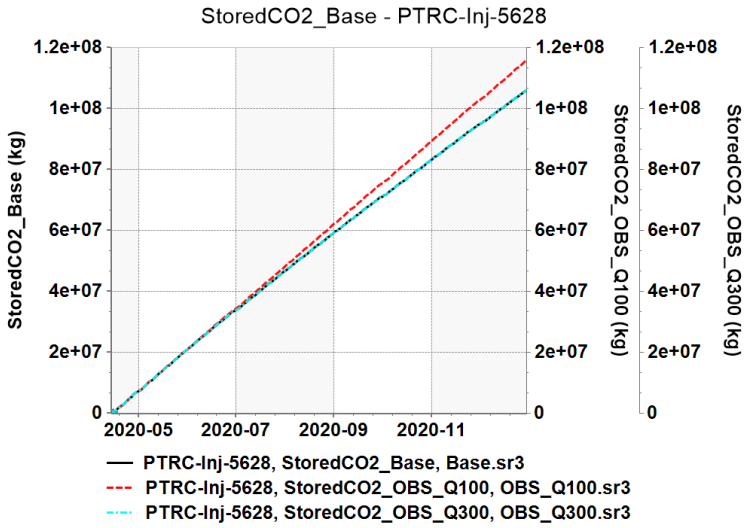
StoredCO2_Base - PTRC-Inj-5628
StoredCO2_Base (kg)
StoredCO2_OBS_Q100 (kg)
StoredCO2_OBS_Q300 (kg)
1.2e+08
1e+08
8e+07
6e+07
4e+07
2e+07
0
2020-05
2020-07
2020-09
2020-11
PTRC-Inj-5628, StoredCO2_Base, Base.sr3
PTRC-Inj-5628, StoredCO2_OBS_Q100, OBS_Q100.sr3
PTRC-Inj-5628, StoredCO2_OBS_Q300, OBS_Q300.sr3

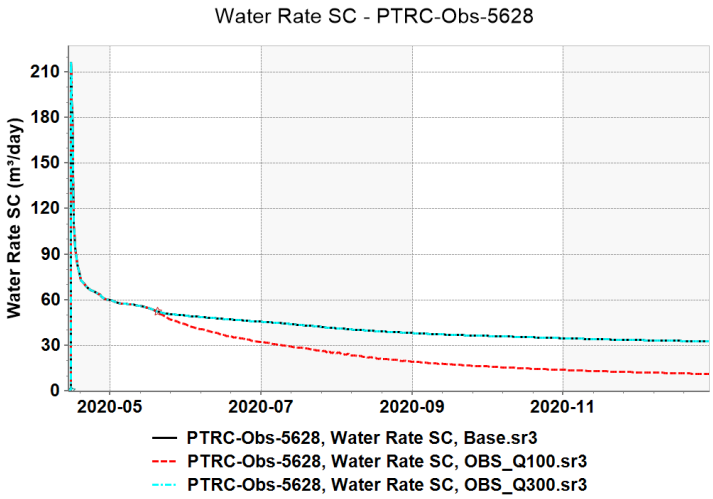
Water Rate SC - PTRC-Obs-5628
Water Rate SC (m³/day)
210
180
150
120
90
60
30
0
2020-05
2020-07
2020-09
2020-11
PTRC-Obs-5628, Water Rate SC, Base.sr3
PTRC-Obs-5628, Water Rate SC, OBS_Q100.sr3
PTRC-Obs-5628, Water Rate SC, OBS_Q300.sr3

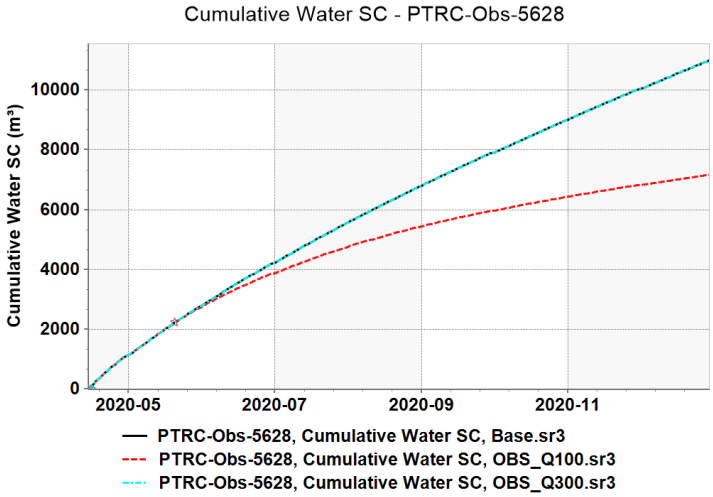
Cumulative Water SC - PTRC-Obs-5628
Cumulative Water SC (m³)
10000
8000
6000
4000
2000
0
2020-05
2020-07
2020-09
2020-11
PTRC-Obs-5628, Cumulative Water SC, Base.sr3
PTRC-Obs-5628, Cumulative Water SC, OBS_Q100.sr3
PTRC-Obs-5628, Cumulative Water SC, OBS_Q300.sr3

Plots related to permeability of the sector model

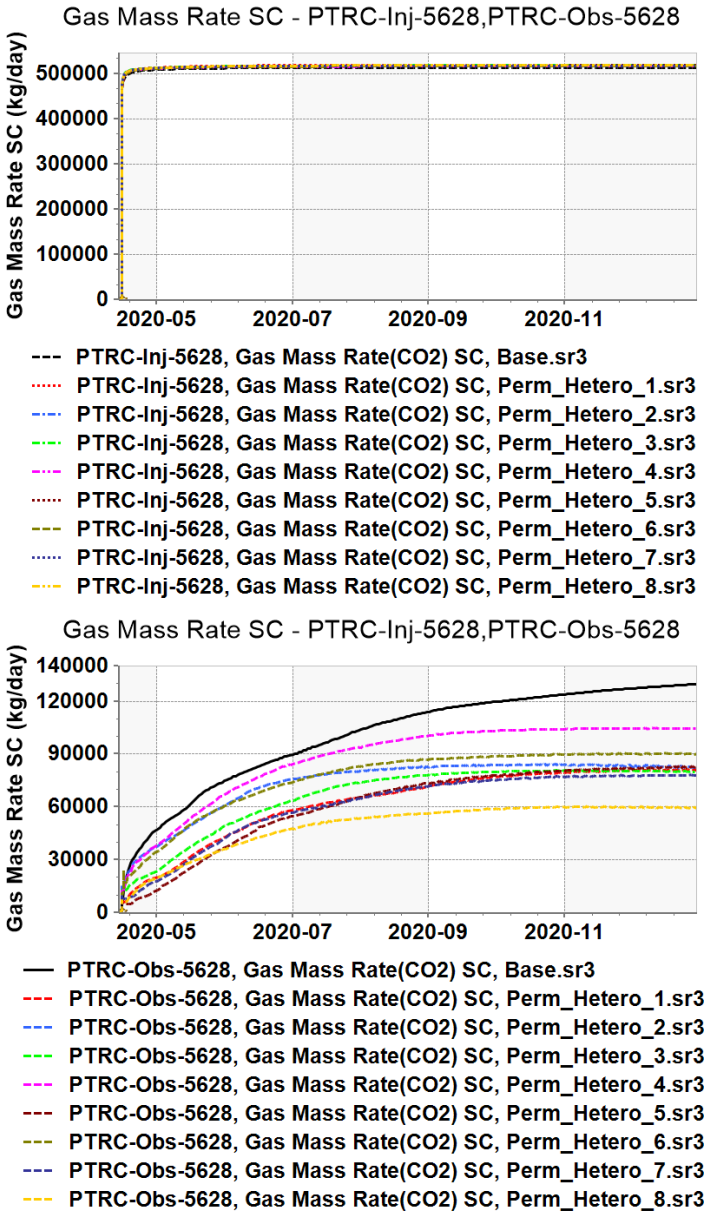

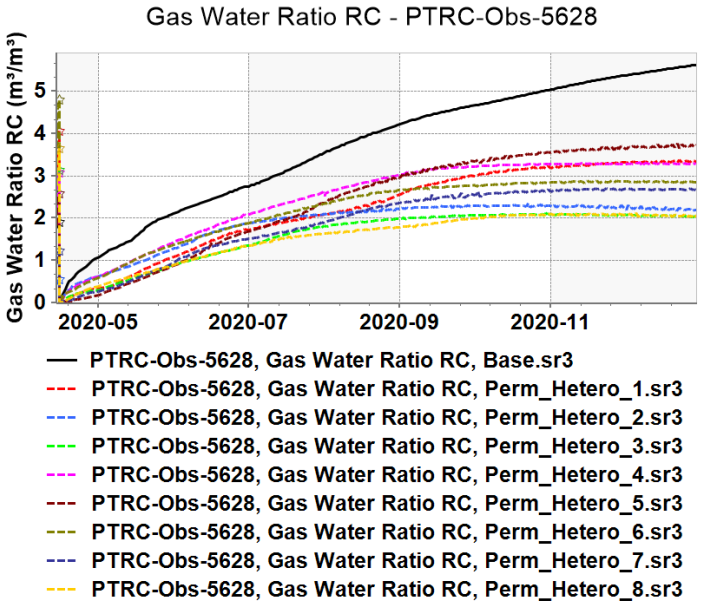
Gas Water Ratio RC - PTRC-Obs-5628
Gas Water Ratio RC (m³/m³)
0
1
2
3
4
5
2020-05
2020-07
2020-09
2020-11
PTRC-Obs-5628, Gas Water Ratio RC, Base.sr3
PTRC-Obs-5628, Gas Water Ratio RC, Perm_Hetero_1.sr3
PTRC-Obs-5628, Gas Water Ratio RC, Perm_Hetero_2.sr3
PTRC-Obs-5628, Gas Water Ratio RC, Perm_Hetero_3.sr3
PTRC-Obs-5628, Gas Water Ratio RC, Perm_Hetero_4.sr3
PTRC-Obs-5628, Gas Water Ratio RC, Perm_Hetero_5.sr3
PTRC-Obs-5628, Gas Water Ratio RC, Perm_Hetero_6.sr3
PTRC-Obs-5628, Gas Water Ratio RC, Perm_Hetero_7.sr3
PTRC-Obs-5628, Gas Water Ratio RC, Perm_Hetero_8.sr3

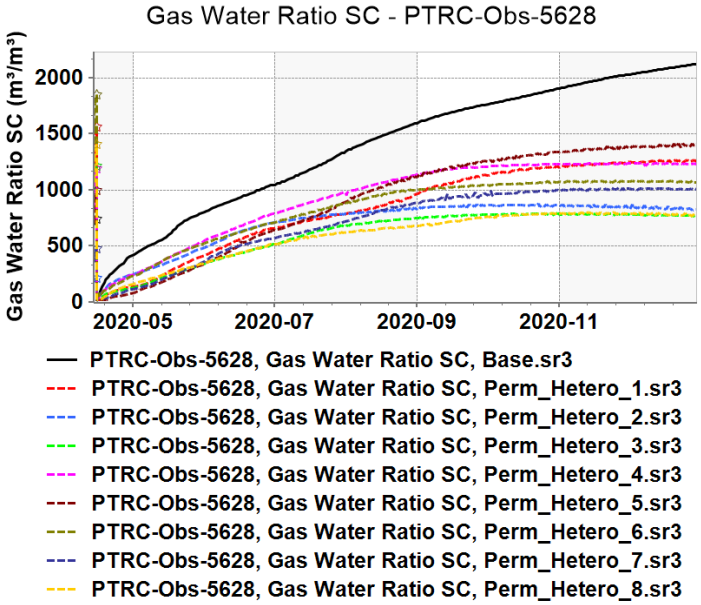
Gas Water Ratio SC - PTRC-Obs-5628
Gas Water Ratio SC (m³/m³)
0
500
1000
1500
2000
2020-05
2020-07
2020-09
2020-11
PTRC-Obs-5628, Gas Water Ratio SC, Base.sr3
PTRC-Obs-5628, Gas Water Ratio SC, Perm_Hetero_1.sr3
PTRC-Obs-5628, Gas Water Ratio SC, Perm_Hetero_2.sr3
PTRC-Obs-5628, Gas Water Ratio SC, Perm_Hetero_3.sr3
PTRC-Obs-5628, Gas Water Ratio SC, Perm_Hetero_4.sr3
PTRC-Obs-5628, Gas Water Ratio SC, Perm_Hetero_5.sr3
PTRC-Obs-5628, Gas Water Ratio SC, Perm_Hetero_6.sr3
PTRC-Obs-5628, Gas Water Ratio SC, Perm_Hetero_7.sr3
PTRC-Obs-5628, Gas Water Ratio SC, Perm_Hetero_8.sr3

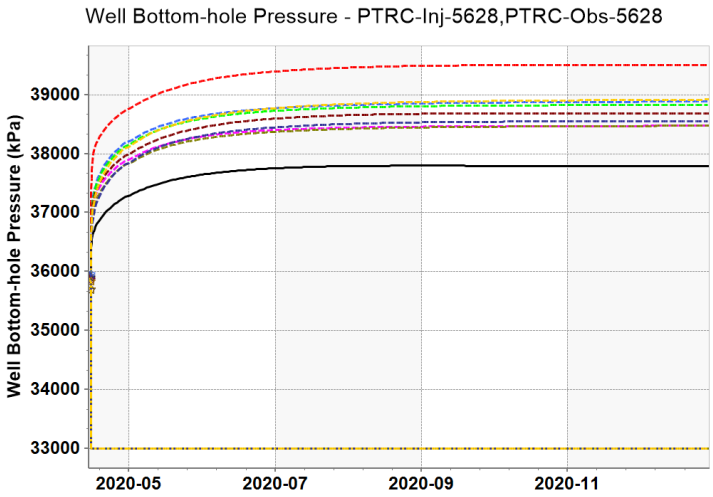
Well Bottom-hole Pressure - PTRC-Inj-5628,PTRC-Obs-5628
Well Bottom-hole Pressure (kPa)
39000
38000
37000
36000
35000
34000
33000
2020-05
2020-07
2020-09
2020-11

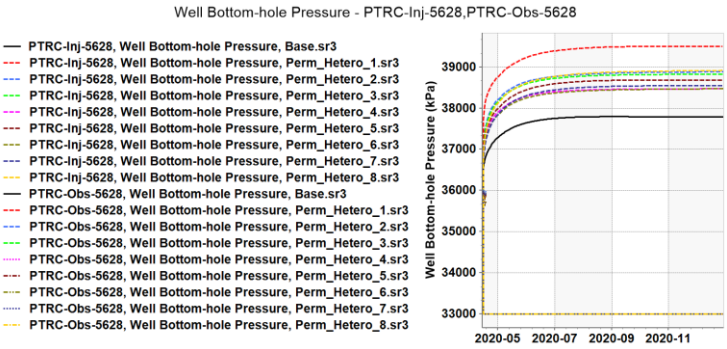
Well Bottom-hole Pressure - PTRC-Inj-5628,PTRC-Obs-5628
PTRC-Inj-5628, Well Bottom-hole Pressure, Base.sr3
PTRC-Inj-5628, Well Bottom-hole Pressure, Perm_Hetero_1.sr3
PTRC-Inj-5628, Well Bottom-hole Pressure, Perm_Hetero_2.sr3
PTRC-Inj-5628, Well Bottom-hole Pressure, Perm_Hetero_3.sr3
PTRC-Inj-5628, Well Bottom-hole Pressure, Perm_Hetero_4.sr3
PTRC-Inj-5628, Well Bottom-hole Pressure, Perm_Hetero_5.sr3
PTRC-Inj-5628, Well Bottom-hole Pressure, Perm_Hetero_6.sr3
PTRC-Inj-5628, Well Bottom-hole Pressure, Perm_Hetero_7.sr3
PTRC-Inj-5628, Well Bottom-hole Pressure, Perm_Hetero_8.sr3
PTRC-Obs-5628, Well Bottom-hole Pressure, Base.sr3
PTRC-Obs-5628, Well Bottom-hole Pressure, Perm_Hetero_1.sr3
PTRC-Obs-5628, Well Bottom-hole Pressure, Perm_Hetero_2.sr3
PTRC-Obs-5628, Well Bottom-hole Pressure, Perm_Hetero_3.sr3
PTRC-Obs-5628, Well Bottom-hole Pressure, Perm_Hetero_4.sr3
PTRC-Obs-5628, Well Bottom-hole Pressure, Perm_Hetero_5.sr3
PTRC-Obs-5628, Well Bottom-hole Pressure, Perm_Hetero_6.sr3
PTRC-Obs-5628, Well Bottom-hole Pressure, Perm_Hetero_7.sr3
PTRC-Obs-5628, Well Bottom-hole Pressure, Perm_Hetero_8.sr3
Well Bottom-hole Pressure (kPa)
39000
38000
37000
36000
35000
34000
33000
2020-05
2020-07
2020-09
2020-11

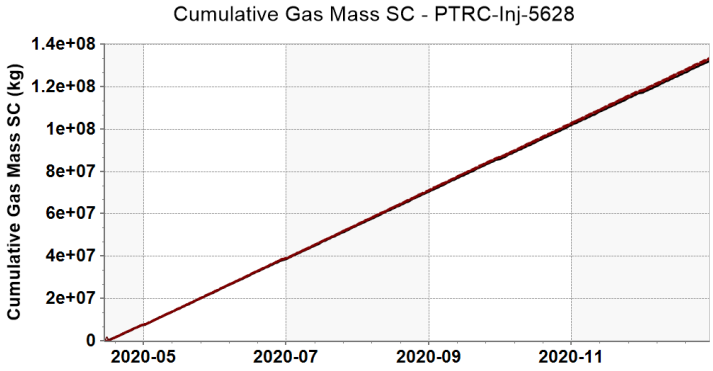
Cumulative Gas Mass SC - PTRC-Inj-5628
Cumulative Gas Mass SC (kg)
1.4e+08
1.2e+08
1e+08
8e+07
6e+07
4e+07
2e+07
0
2020-05
2020-07
2020-09
2020-11

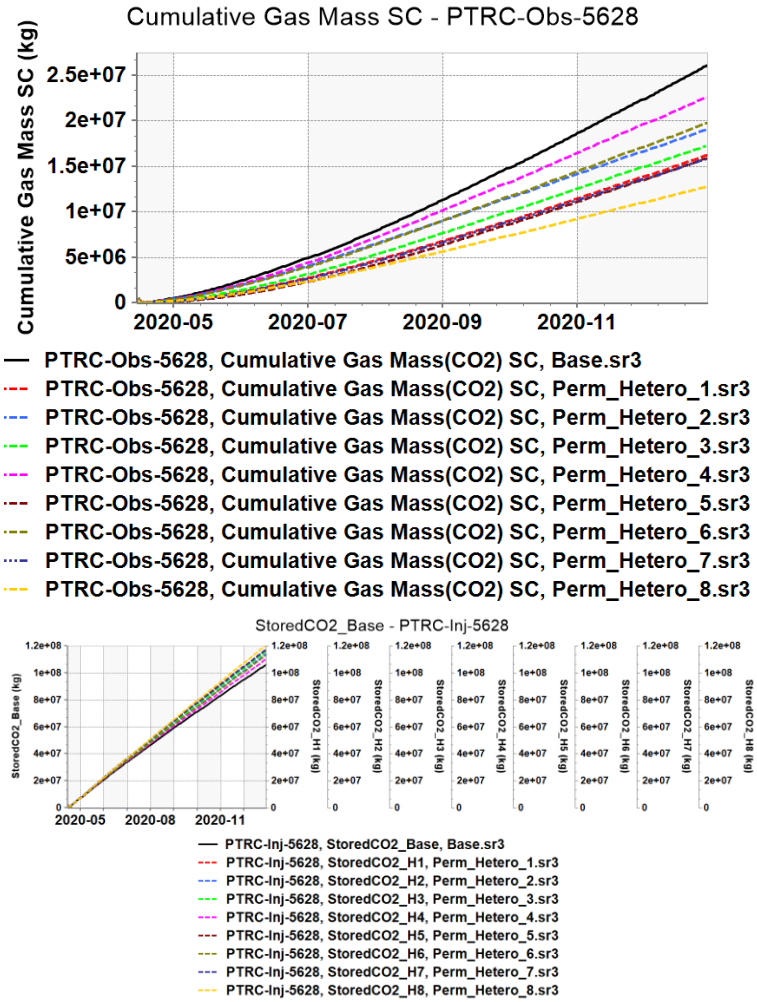
Cumulative Gas Mass SC - PTRC-Obs-5628
Cumulative Gas Mass SC (kg)
2.5e+07
2e+07
1.5e+07
1e+07
5e+06
0
2020-05
2020-07
2020-09
2020-11
PTRC-Obs-5628, Cumulative Gas Mass(CO2) SC, Base.sr3
PTRC-Obs-5628, Cumulative Gas Mass(CO2) SC, Perm_Hetero_1.sr3
PTRC-Obs-5628, Cumulative Gas Mass(CO2) SC, Perm_Hetero_2.sr3
PTRC-Obs-5628, Cumulative Gas Mass(CO2) SC, Perm_Hetero_3.sr3
PTRC-Obs-5628, Cumulative Gas Mass(CO2) SC, Perm_Hetero_4.sr3
PTRC-Obs-5628, Cumulative Gas Mass(CO2) SC, Perm_Hetero_5.sr3
PTRC-Obs-5628, Cumulative Gas Mass(CO2) SC, Perm_Hetero_6.sr3
PTRC-Obs-5628, Cumulative Gas Mass(CO2) SC, Perm_Hetero_7.sr3
PTRC-Obs-5628, Cumulative Gas Mass(CO2) SC, Perm_Hetero_8.sr3

StoredCO2_Base - PTRC-Inj-5628
StoredCO2_Base (kg)
StoredCO2_H1 (kg)
StoredCO2_H2 (kg)
StoredCO2_H3 (kg)
StoredCO2_H4 (kg)
StoredCO2_H5 (kg)
StoredCO2_H6 (kg)
StoredCO2_H7 (kg)
StoredCO2_H8 (kg)
1.2e+08
1e+08
8e+07
6e+07
4e+07
2e+07
0
2020-05
2020-08
2020-11
PTRC-Inj-5628, StoredCO2_Base, Base.sr3
PTRC-Inj-5628, StoredCO2_H1, Perm_Hetero_1.sr3
PTRC-Inj-5628, StoredCO2_H2, Perm_Hetero_2.sr3
PTRC-Inj-5628, StoredCO2_H3, Perm_Hetero_3.sr3
PTRC-Inj-5628, StoredCO2_H4, Perm_Hetero_4.sr3
PTRC-Inj-5628, StoredCO2_H5, Perm_Hetero_5.sr3
PTRC-Inj-5628, StoredCO2_H6, Perm_Hetero_6.sr3
PTRC-Inj-5628, StoredCO2_H7, Perm_Hetero_7.sr3
PTRC-Inj-5628, StoredCO2_H8, Perm_Hetero_8.sr3

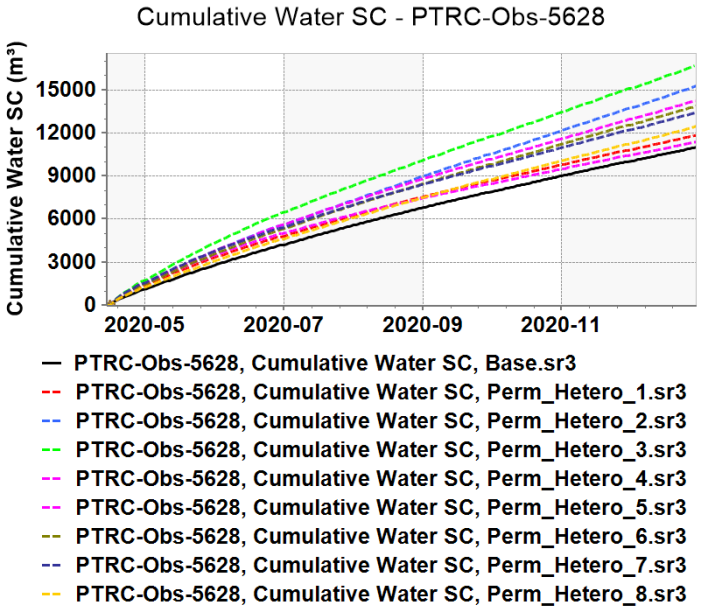
Cumulative Water SC - PTRC-Obs-5628
Cumulative Water SC (m³)
15000
12000
9000
6000
3000
0
2020-05
2020-07
2020-09
2020-11
PTRC-Obs-5628, Cumulative Water SC, Base.sr3
PTRC-Obs-5628, Cumulative Water SC, Perm_Hetero_1.sr3
PTRC-Obs-5628, Cumulative Water SC, Perm_Hetero_2.sr3
PTRC-Obs-5628, Cumulative Water SC, Perm_Hetero_3.sr3
PTRC-Obs-5628, Cumulative Water SC, Perm_Hetero_4.sr3
PTRC-Obs-5628, Cumulative Water SC, Perm_Hetero_5.sr3
PTRC-Obs-5628, Cumulative Water SC, Perm_Hetero_6.sr3
PTRC-Obs-5628, Cumulative Water SC, Perm_Hetero_7.sr3
PTRC-Obs-5628, Cumulative Water SC, Perm_Hetero_8.sr3

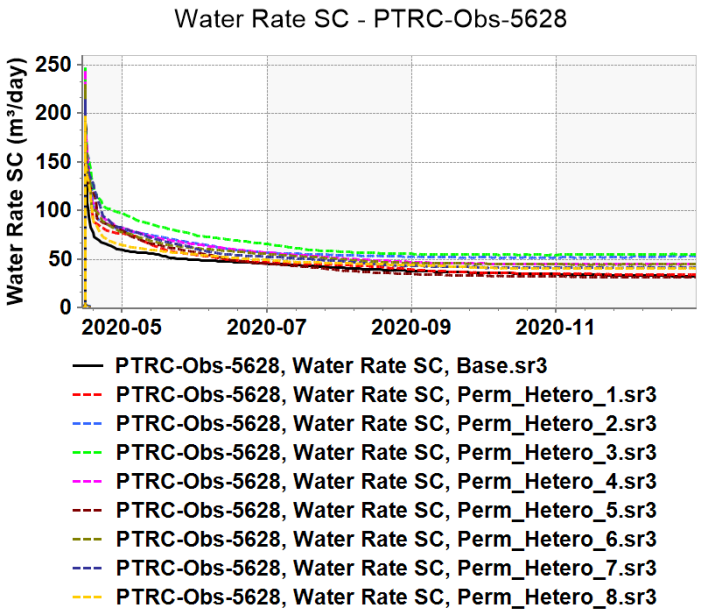
Water Rate SC - PTRC-Obs-5628
Water Rate SC (m³/day)
250
200
150
100
50
0
2020-05
2020-07
2020-09
2020-11
PTRC-Obs-5628, Water Rate SC, Base.sr3
PTRC-Obs-5628, Water Rate SC, Perm_Hetero_1.sr3
PTRC-Obs-5628, Water Rate SC, Perm_Hetero_2.sr3
PTRC-Obs-5628, Water Rate SC, Perm_Hetero_3.sr3
PTRC-Obs-5628, Water Rate SC, Perm_Hetero_4.sr3
PTRC-Obs-5628, Water Rate SC, Perm_Hetero_5.sr3
PTRC-Obs-5628, Water Rate SC, Perm_Hetero_6.sr3
PTRC-Obs-5628, Water Rate SC, Perm_Hetero_7.sr3
PTRC-Obs-5628, Water Rate SC, Perm_Hetero_8.sr3

Plots related to post-workover permeability enhancement

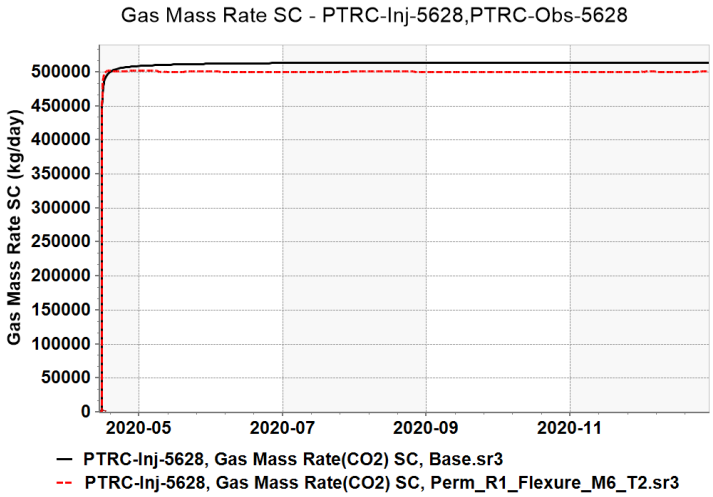

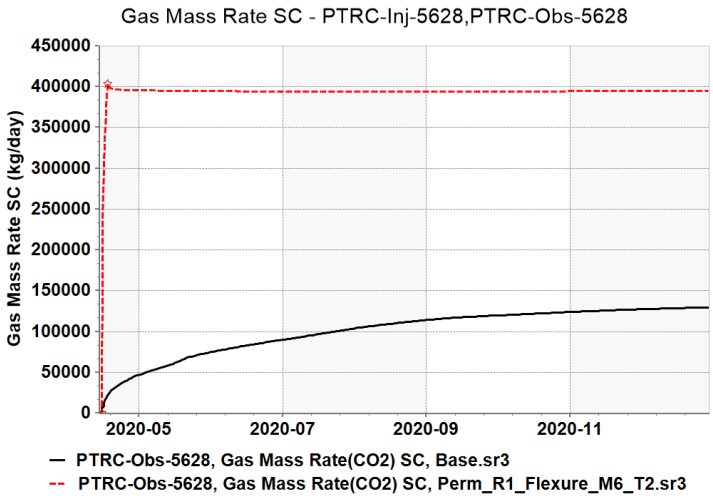

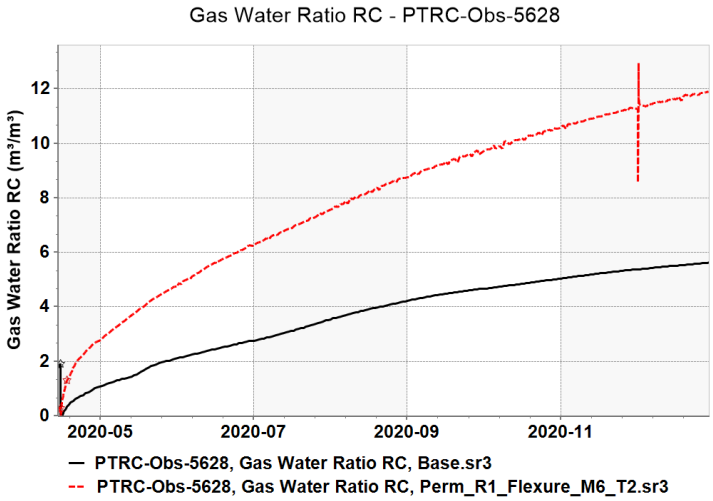

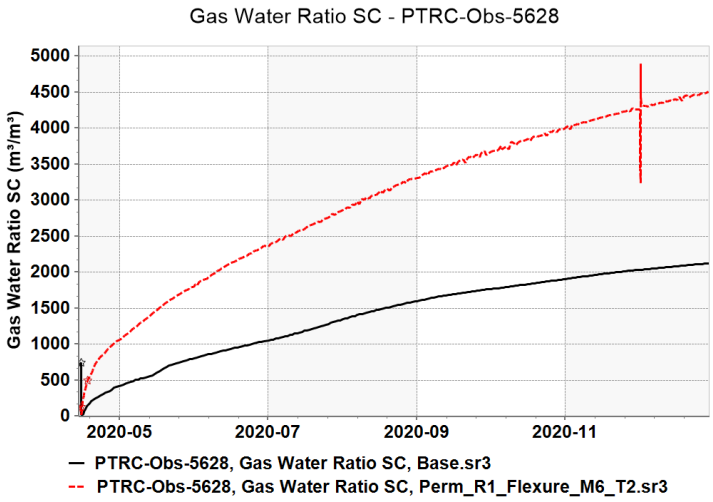
Gas Water Ratio SC - PTRC-Obs-5628
Gas Water Ratio SC (m³/m³)
5000
4500
4000
3500
3000
2500
2000
1500
1000
500
0
2020-05
2020-07
2020-09
2020-11
PTRC-Obs-5628, Gas Water Ratio SC, Base.sr3
PTRC-Obs-5628, Gas Water Ratio SC, Perm_R1_Flexure_M6_T2.sr3

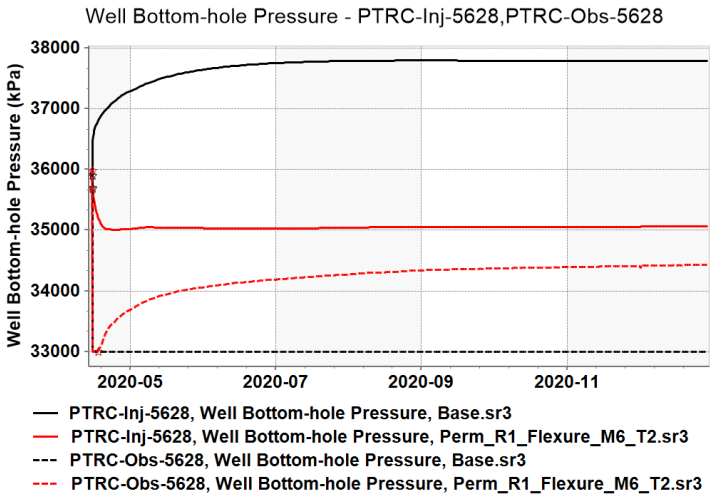
Well Bottom-hole Pressure - PTRC-Inj-5628,PTRC-Obs-5628
Well Bottom-hole Pressure (kPa)
38000
37000
36000
35000
34000
33000
2020-05
2020-07
2020-09
2020-11
PTRC-Inj-5628, Well Bottom-hole Pressure, Base.sr3
PTRC-Inj-5628, Well Bottom-hole Pressure, Perm_R1_Flexure_M6_T2.sr3
PTRC-Obs-5628, Well Bottom-hole Pressure, Base.sr3
PTRC-Obs-5628, Well Bottom-hole Pressure, Perm_R1_Flexure_M6_T2.sr3

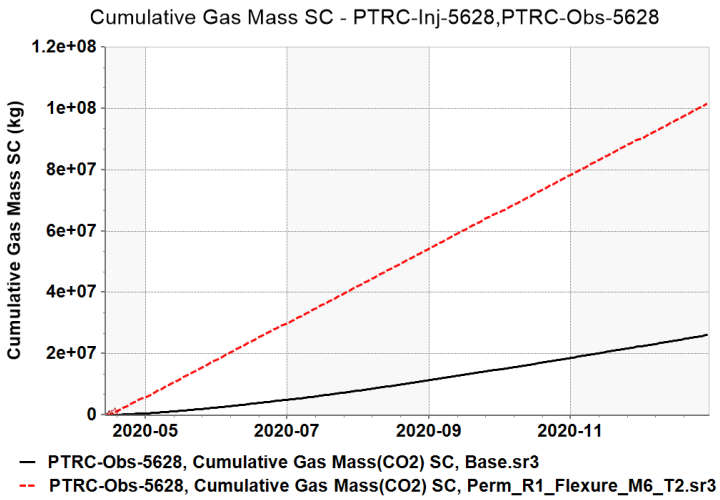
Cumulative Gas Mass SC - PTRC-Inj-5628,PTRC-Obs-5628
Cumulative Gas Mass SC (kg)
1.2e+08
1e+08
8e+07
6e+07
4e+07
2e+07
0
2020-05
2020-07
2020-09
2020-11
PTRC-Obs-5628, Cumulative Gas Mass(CO2) SC, Base.sr3
PTRC-Obs-5628, Cumulative Gas Mass(CO2) SC, Perm_R1_Flexure_M6_T2.sr3

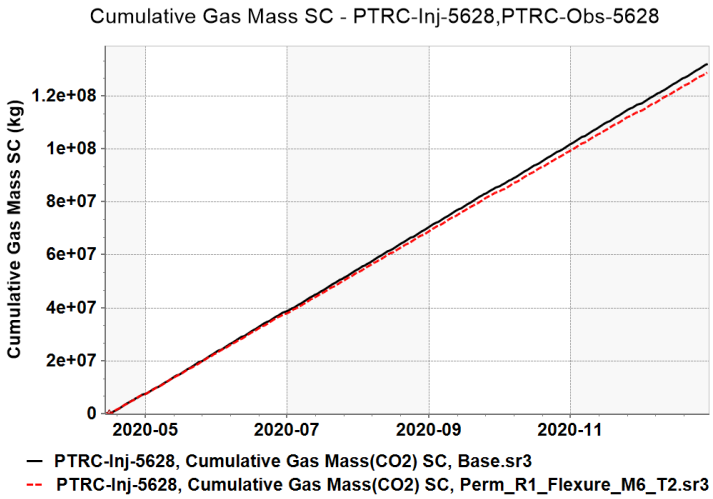
Cumulative Gas Mass SC - PTRC-Inj-5628,PTRC-Obs-5628
Cumulative Gas Mass SC (kg)
1.2e+08
1e+08
8e+07
6e+07
4e+07
2e+07
0
2020-05
2020-07
2020-09
2020-11
PTRC-Inj-5628, Cumulative Gas Mass(CO2) SC, Base.sr3
PTRC-Inj-5628, Cumulative Gas Mass(CO2) SC, Perm_R1_Flexure_M6_T2.sr3

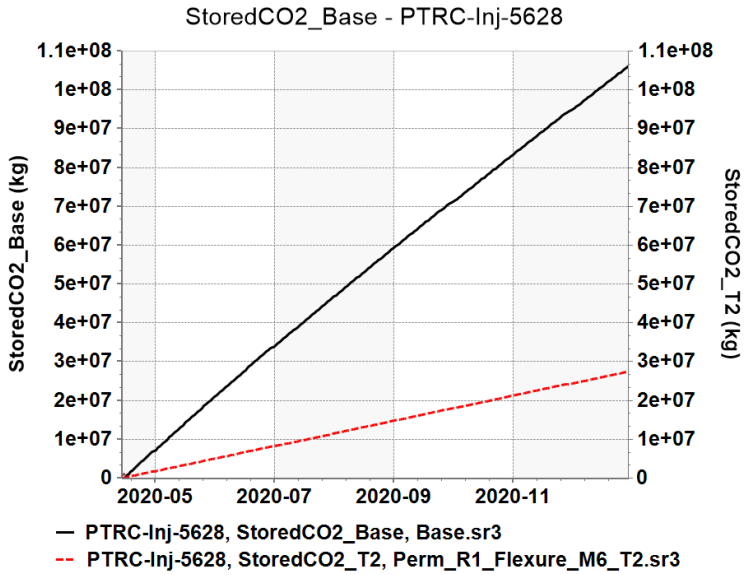
StoredCO2_Base - PTRC-Inj-5628
StoredCO2_Base (kg)
StoredCO2_T2 (kg)
1.1e+08
1e+08
9e+07
8e+07
7e+07
6e+07
5e+07
4e+07
3e+07
2e+07
1e+07
0
2020-05
2020-07
2020-09
2020-11
PTRC-Inj-5628, StoredCO2_Base, Base.sr3
PTRC-Inj-5628, StoredCO2_T2, Perm_R1_Flexure_M6_T2.sr3

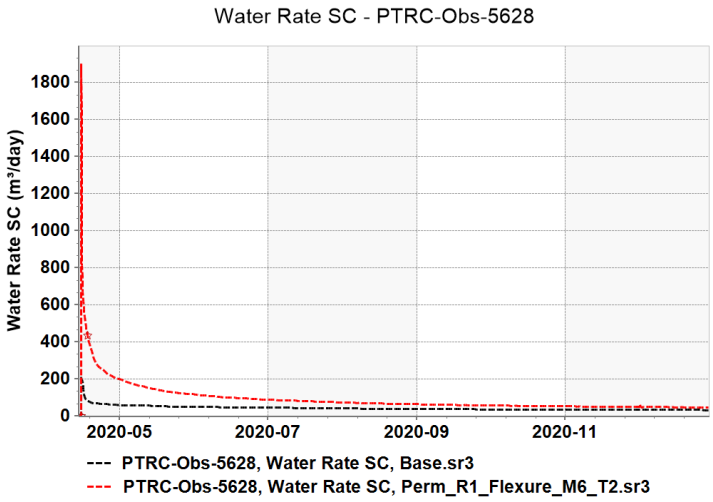
Water Rate SC - PTRC-Obs-5628
Water Rate SC (m³/day)
1800
1600
1400
1200
1000
800
600
400
200
0
2020-05
2020-07
2020-09
2020-11
PTRC-Obs-5628, Water Rate SC, Base.sr3
PTRC-Obs-5628, Water Rate SC, Perm_R1_Flexure_M6_T2.sr3

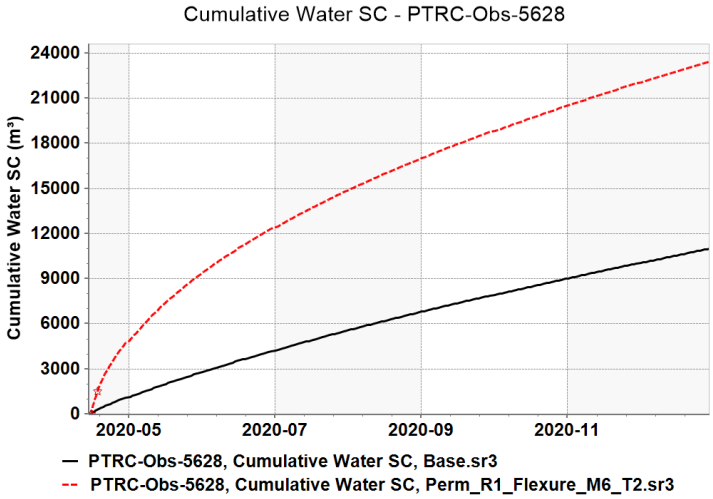
Cumulative Water SC - PTRC-Obs-5628
Cumulative Water SC (m³)
24000
21000
18000
15000
12000
9000
6000
3000
0
2020-05
2020-07
2020-09
2020-11
PTRC-Obs-5628, Cumulative Water SC, Base.sr3
PTRC-Obs-5628, Cumulative Water SC, Perm_R1_Flexure_M6_T2.sr3